PROBING COMPLEX IONIC DYNAMICS ON THE NANOSCALE VIA ENERGY DISCOVERY PLATFORMS

A Dissertation
Presented to
The Academic Faculty

by

Jilai Ding

In Partial Fulfillment
of the Requirements for the Degree
DOCTOR OF PHILOSOPHY in the
SCHOOL OF MATERIALS SCIENCE AND ENGINEERING

Georgia Institute of Technology
AUG 2017

COPYRIGHT © 2017 BY JILAI DING

PROBING COMPLEX IONIC DYNAMICS ON THE NANOSCALE

VIA ENERGY DISCOVERY PLATFORMS

Approved by:

Dr. Nazanin Bassiri-Gharb, Advisor
G.W. Woodruff School of Mechanical Engineering
Georgia Institute of Technology

Dr. Rosario Gerhardt
School of Materials Science and Engineering
Georgia Institute of Technology

Dr. Raymond R. Unocic
Center of Nanophase Materials Sciences
Oak Ridge National Laboratory

Dr. Faisal Alamgir
School of Materials Science and Engineering
Georgia Institute of Technology

Dr. Meilin Liu
School of Materials Science and Engineering
Georgia Institute of Technology

Date Approved: Jul. 28, 2017

To my wife.

ACKNOWLEDGEMENTS

First of all, I would like to express my appreciation to my Ph.D. advisor, Prof. Nazanin Bassiri-Gharb, who has always been passionate and patient, giving me inspiration and a lot of great ideas and advice in my Ph.D. life. I would not accomplish my thesis without her guidance and support. I also appreciate the great research opportunity she provided at Oak Ridge National Laboratory (ORNL), where I gained solid expertise on my research.

I would also thank Dr. Raymond Unocic, who trained me, supervised me and gave me great support during my two years of research at ORNL. He is not only an excellent co-advisor, but also a good friend, and I believe our friendship will continue in the future.

Also, I would thank my committee members, Dr. Meilin Liu, Dr. Rosario Gerhardt and Dr. Faisal Alamgir, who devoted their precious time, giving me a lot of great suggestions on my thesis.

It was a great honor working with a lot of nice and smart people at ORNL. Special thanks to Dr. Ray Unocic, who trained me on STEM and EELS; Dr. Wei Guo, who performed APT measurements and analysis in this thesis; Dr. Evgheni Strelcov, who trained me on tr-KPFM; Dr. Craig Bridges, who helped me with EIS measurements; Dr. Janakiraman Balachandran, who provided insightful ideas and theoretical calculations; Dr. Xiahan Sang, who provided assistance in distortion analysis from atomically resolved STEM images; Dr. Chris Rouleau, who trained me on PLD. I'd also express my thanks to Dr. Sergei Kalinin, Dr. Panchapakesan Ganesh, Dr. Lianshan Lin, Dr. Jonathan Poplawsky,

Dr. Gabriel Veith and Dr. Yongqiang Cheng, who answered my questions patiently and gave me great advice on my research. I enjoyed the time working with all of you!

I would also bring my thanks to my group members at Georgia Tech: Dr. Yaser Bastani, Steven Brewer, Talia Field, Aida Yoguely Cortes-Pena and Sina Hashemi. And my friends Yang Zhang, Tao Zhu, Zhou Lan, Dr. Jun Chen, Hao Luo, Dr. Bo Zhao, Xiaotang Du, Dr. BeiBei Jiang, Yanjie He, etc. Thank you all for sharing your passion and intelligence.

Last but not least, I owe many thanks to my wife, Weikang, who always gave me endless support and encouragement.

TABLE OF CONTENTS

LIST OF TABLES

LIST OF FIGURES

LIST OF SYMBOLS AND ABBREVIATIONS

A	Cross sectional area of a material
a	Interplanar distance of a crystal
AC	Alternating current
AFC	Alkaline fuel cell
AFM	Atomic force microscopy
AH	Absolute humidity
APT	Atom probe tomography
BZO	Barium zirconate, $BaZrO_3$
C	Capacitance
γ	Damping coefficient
$C_{M,N}$	Correlation coefficient between matrix M and N
CPD	Contact potential difference
CSD	Chemical solution deposition
D	Diffusivity
d	Distance
DC	Direct current
DFT	Density functional theory
E	Electric field
e	Elementary charge
ε_0	Dielectric permittivity of free space
ε_r	Relative permittivity
E_a	Activation energy

EELS	Electron energy loss spectroscopy
EIS	Electrochemical impedance spectroscopy
ESM	Electrochemical strain microscopy
F	Faraday's constant
F	Force
f	Charge dissipation rate
f	Lotgering factor
f	Transference function of cantilever
FC	Fuel cell
FEM	Finite element method
FIB	Focused-ion beam
FWHW	Full-with at half maximum
GDC	Gadolinium doped ceria
H	Humidity
HAADF	High-angle annular dark field
I	Current
IPA	Isopropyl alcohol
J	Current density
J_D	Diffusion flux
JSPDS	Joint Committee on Powder Diffraction Standards
K	Calibration coefficient
k	Reaction constant
k	Boltzmann's constant
K_w	Dissociation constant of water
l	Length of a material

λ	Wavelength of an electromagnetic wave
LPCVD	Low-pressure chemical vapor deposition
LSAT	Lanthanum aluminate - strontium aluminum tantalite, $(LaAlO_3)_{0.3}(Sr_2TaAlO_6)_{0.7}$
LSM	Lanthanum strontium manganite, $La_{1-x}Sr_xMnO_{3-\delta}$
m	Mass
μ	Electric mobility
MCFC	Molten carbonate fuel cell
MD	Molecular dynamics
MEMS	Micro-electro-mechanical systems
MIEC	Mixed ionic-electronic conductor
n	Concentration
n	Real part of refractive index
NC	Nanostructured ceria
NEB	Nudged elastic band
NGO	$NdGaO_3$
p	Pressure
PAFC	Phosphoric acid fuel cell
PEMFC	Proton exchange membrane fuel cell
PFM	Piezoresponse force microscopy
PLD	Pulsed laser deposition
PVD	Physical vapor deposition
R	Electrical resistance
ρ	Electrical resistivity
RH	Relative humidity

RHEED	Reflection high-energy electron diffraction
S	Charge generation rate
σ	Electrical conductivity
SD	Sputter deposition
SEM	Scanning electron microscopy
SIM	Scanning impedance microscopy
SOFC	Solid oxide fuel cell
SPM	Scanning probe microscopy
STEM	Scanning transmission electron microscopy
T	Temperature
t	Film thickness
t	Time
τ	Time constant
TEM	Transmission electron microscopy
TPB	Triple phase boundary
tr-KPFM	Time-resolved Kelvin probe force microscopy
V	Potential
v_d	Velocity
Φ	Potential
χ	Work function
ω	Oscillation frequency
XRD	X-ray diffraction
XPS	X-ray photoelectron spectroscopy
Y-BZO	Yttrium-doped barium zirconate
YSZ	Yttrium-stabilized zirconia

Z	Atomic number
Z	Complex impedance
z	Charge number
z	Tip-surface distance

SUMMARY

Ionic dynamics underpin the functionalities of a broad spectrum of materials and devices ranging from energy storage and conversion, to sensors and catalytic devices. Understanding the ionic dynamics on the nanoscale is, thus, crucial for improving the performance of these applications and designing the next generation of devices. Electrochemical reactivity and ionic transport in these systems are, however, complex processes, controlled by the interplay of charge injection and field- and diffusion-controlled transport. These processes are often very sensitive to the environmental conditions and microstructure of the material. To understand the fundamental mechanisms underpinning the electrochemical functionality, it is vital to separate the spatial localization of reaction and transport processes on the nanoscale at controlled conditions, and correlate them with its microstructure and atomic structure.

This study uncovers complex ionic dynamics in functional oxides via energy discovery platforms, which combine microfabricated lateral devices with *in-situ* microscopy and spectroscopy techniques under controlled conditions. To be specific, the electrochemical reactivity and proton conduction mechanisms were investigated by multiple techniques, such as time-resolved Kelvin probe force microscopy (tr-KPFM) and electrochemical impedance spectroscopy (EIS), on nanostructured ceria (NC) and yttrium-doped barium zirconate (Y-BZO). Tr-KPFM, being a novel scanning probe technique, offers excellent spatial and temporal resolutions of surface potential variation that can directly related to the ionic reaction and conduction of the material, proving a good candidate for ionic dynamics study. In addition, theoretical calculations including finite

element method (FEM) and density functional theory (DFT) were utilized to explore the fundamental physics of the ionic dynamics.

NC thin film with lateral Pt electrodes was first prepared for demonstration of the feasibility of energy discovery platforms. Placing the NC lateral device in a gas cell, the effect of external conditions including temperature, relative humidity, DC bias and atmosphere was investigated. The effect of triple phase boundaries (TPBs) was also studied by controlling the presence and absence of TPBs through microfabrication. The surface electrochemical reactions and conduction pathways between electrodes were proposed. Under externally applied bias, water on the NC surface or from the ambient decomposes, generating protons and hydroxyl groups that are transported through the NC, causing the surface potential variation. FEM was utilized to simulate the physical processes of the phenomena, and the physical parameters such as proton generation rate and ionic diffusivity and mobility were obtained as a function of environmental conditions. Through both experimental and theoretical calculation, two conduction mechanisms were identified, which are surface proton conduction through condensed water layer, and bulk conduction through chemisorbed water layer.

The effect of internal conditions such as microstructure on the electrochemical reactivity and proton conductivity was also studied on NC. NC films with various surface roughness, grain boundaries and crystal orientation were prepared via pulsed laser deposition, sputter deposition and chemical solution deposition. It was found that surface morphology determines the water splitting rate and proton conductivity at 25 °C and wet condition, while grain size and crystallographic orientation became significant factors at higher temperature (e.g. 125 °C) and dry condition. Moreover, the grain size mainly

affected the proton generation rate and the crystallographic orientation determines the proton transport process along the surface. This result further demonstrates the existence of two conduction regimes in NC.

The second material studied, Y-BZO thin film samples with various dopant concentrations were prepared by pulsed laser deposition (PLD) that showed limited grain boundaries. It was observed that the activation energy for proton transport monotonically increases with increasing dopant concentration. To understand this phenomenon, distortion analysis was performed on atomic resolution images obtained via scanning transmission electron microscopy (STEM). As dopant level increases, more Y-Y clusters form statistically, which increases the local lattice distortion. This dopant-dopant association induced increase in lattice distortion leads to an increase in trapping of defects such as oxygen vacancies and proton interstitials, forming defect-clusters, thereby explaining the observed monotonic increase in the activation energy. This finding provides ways of designing new proton conducting oxides by avoiding dopant cluster formation and lattice distortion.

The effects of non-stoichiometry and lattice strain on proton conduction in Y-BZO were further studied. Non-stoichiometry, or barium deficient Y-BZO was created by high temperature annealing of the thin film samples. The result suggested a decreased barium content after annealing, with the formation of darker contrast regions, where barium vacancy sites are substituted with yttrium and barium. This results in a smaller lattice distortion in the major lattice of Y-BZO. The activation energy for proton transport significantly decreases from 0.65 eV to 0.55 eV after annealing, indicating a smaller energy barrier and better proton transport properties. In addition, the effect of Y-BZO lattice strain

on proton transport is studied. A variety of lattice strains were created by epitaxial deposition of Y-BZO on different substrates. The result showed that both the compressive strain and tensile strain led to an increase of activation energy for proton transport, from 0.65 eV up to 0.70 eV. This novel discovery promises new ways of devices design to enable future electrochemical applications with higher performance.

CHAPTER 1. INTRODUCTION

1.1 Ionic Dynamics in Solid Oxides

The rapid development of human society and the depleting of fossil fuels necessitate environmental friendly and highly efficient technologies for energy generation, storage and conversion.[1-3] Many of these technologies are underpinned by ionic conducting oxides, which are attracting significant scientific attention due to their considerable promise in electrochemical devices and energy related applications, such as solid oxide fuel cells (SOFCs),[4-6] gas sensors,[7-9] and hydrogen permeation membranes.[10] In order to improve the performance of these applications and designing the next generation of devices, it is vital to understand the basic functionalities of the ionic dynamics on the nanoscale.

The electrochemical reactions and ionic transport phenomena have been investigated worldwide for over a hundred years.[7, 11] However, these processes are often complex, controlled by the interplay of charge injection and field-controlled and diffusion-controlled transport. They often originate in multiple reactions and transport stages, involving the generation of ionic species and charge injection on the surfaces, interfaces, and triple phase boundaries (TPBs), and surface and/or bulk transport of charge carriers including electrons and ions. Therefore, they are easily affected by the material's microstructure and environmental conditions. Moreover, as device miniaturization becomes a trend in the modern-day micro electromechanical systems (MEMS) study, chemical phenomena are intertwined with physical phenomena in micron or nanometer scales, making the ionic dynamics even more complicated.

In order to understand the fundamental mechanisms underpinning electrochemical functionality, it is vital to separate the spatial localization of reaction and transport processes of each charged carrier species, as well as the physical parameters that control the phenomena. If achieved, this will allow exploring complex ionic dynamics on the nanoscale, providing insight of mechanisms of the energy applications.

In the following part, the working principles and materials for two major applications, solid oxide fuel cells and gas sensors are introduced in details, both of which are based on electrochemical reaction and ionic conducting solid oxides.

1.2 Basics of Ionic Conduction in Solid Oxides

1.2.1 Definitions of Electric Conductivity

The electrical resistance (R) of a material is a measure of the difficulty to pass an electric current through it. R is defined by the Ohm's law:

$$I = U/R \tag{1}$$

where I is the current passing through the material in units of amperes, and U is the voltage applied across the material in units of volts, R is in units of ohms.

For a given material, the resistance depends on its shape. R is inversely proportional to the cross-sectional area, and is proportional to the length. Therefore, the R can be written as Equation 2, where l is the length of the conductor, A is the cross-sectional area of the conductor and ρ is the electrical resistivity of the material. The electrical resistivity is an

intrinsic property of the material that quantifies the inability of a material to conduct electric current.

$$R = \rho \frac{l}{A} \tag{2}$$

The electrical conductivity σ, as shown in Equation 3, is the reciprocal of electrical resistivity. It is a measure of the ability of a material to conduct an electric current in units of Siemens per meter (*S/m*).

$$\sigma = \frac{1}{\rho} \tag{3}$$

1.2.2 Types of Electric Conduction

1.2.2.1 Electric Conduction in Metal

Metals are typically a type of material that exhibit very good electric conductivity. The high conductivity in metal originates from the delocalized outer electrons. A metal consists of a lattice of atoms, each with outer shell of electrons that freely dissociate from their parent atoms and form a sea of electrons that conduct electric current. When a voltage is applied across a metal, an electric field forms, which provides driving force for electrons to drift towards the positive end.

From electron band structure's perspective, in metal, conduction bands and valence bands are overlapped and therefore there is no energy gap between them (Figure 1-1). Then

conduction band is partially occupied by electrons, who are available to move under electric field, resulting in a high electrical conductivity.

1.2.2.2 Electric Conduction in Semiconductor and Insulator

Besides electric conductors such as metals, solid state materials can be categorized into two other groups according to their conductivity: insulators and semiconductors. Typically, insulators are materials having an electrical conductivity $\sigma < 10^{-8}$ *S/cm*, and semiconductors have a conductivity between 10^{-8} and 10^{3} *S/cm*. In insulators, there is no free electrons to conduct current. In these materials, there may be forbidden electron bands (band gaps): energy intervals that contain no electrons, as shown in Figure 1-1. The Fermi level lies in the band gap, meaning that at absolute zero degree, the electrons fully occupy valence band and do not occupy conduction band. There are no free conduction electrons, and the resistance is infinite. In insulators, the band gap typically exceeds 9 eV, therefore thermal energy at room temperature is not sufficient to allow electrons from the valence band to be activated to the conduction band. Whereas for semiconductors, the band gap is lower compared to insulators (~1 eV). The electrons in valence band can be partially activated into conduction band, allowing electrons passing through, although much smaller compared to conductors.

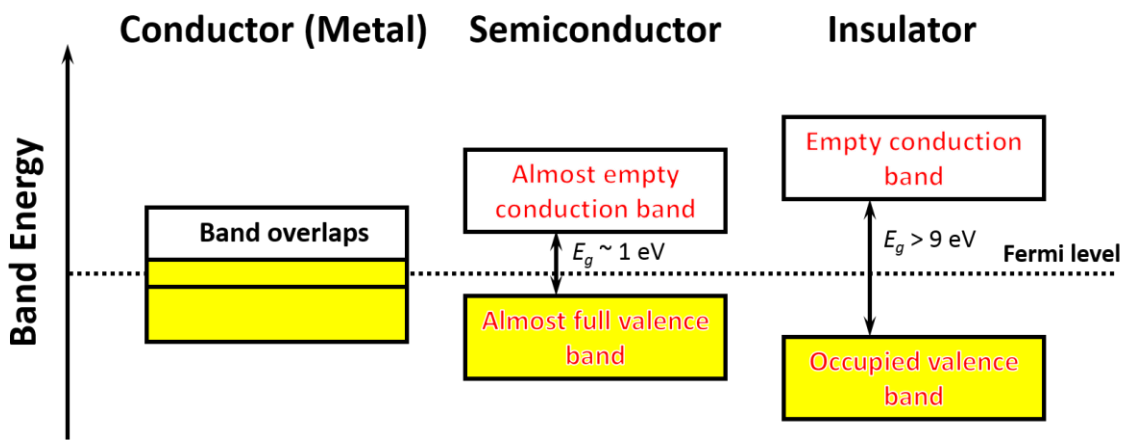

Figure 1-1 – Electron band structures of conductor, semiconductor and insulator.

1.2.2.3 Electric Conduction in Ionic Electrolytes

The electric conduction introduced above are based on band electrons or holes. However, in many solid or liquid electrolytes, charged ions are the main charge carriers that show electric conduction under electric field, which have wide applications such as batteries, fuel cells and sensors. In liquid electrolytes, the resistivity of ionic conduction is largely dependent on the concentration of movable charged ions in the solution. In solid ionic conductors, the material contains defects such as vacancies and interstitials that allow the migration of ions in an electric field. In such materials, high temperature is often needed, and the electric conduction is not only determined by the ionic concentration, but also the activation energy for ions to hop within the lattice.

The total conductivity of a material is contributed by different charge carriers. In solid electrolytes, the relevant charge carriers include both ions such as O^{2-}, OH^- and H^+, and electrons (e^-) and holes (h^+), as shown in Equation 4:

$$\sigma = \sigma_{O^{2-}} + \sigma_{OH^-} + \sigma_{H^+} + \sigma_{e^-} + \sigma_{h^+} \quad (4)$$

In most of the applications of solid oxides, it is desirable to optimize the ionic conductivity and minimize the conductivity of electrons and holes. Therefore, factors affecting the ionic conductivity and ways to improve the total conduction is further introduced in the following part.

1.2.3 Diffusion and Mobility

Diffusion is a process whereby molecules or atoms in a material move from a high concentration region to a low concentration region. Such concentration gradient is the driving force for diffusion, and is described by Fick's laws of diffusion.

Fick's first law, as shown in Equation 5, relates the diffusive flux to the concentration under the assumption of steady state (concentration does not change with time).

$$J_D = -D\frac{dn}{dx} \quad (5)$$

In the equation, J_D is the diffusion flux in units of mol/m^{2}s, which is defined as the amount of the materials passing through a unit area per unit time. D is the diffusion coefficient or diffusivity, which is the proportionally constant in units of m^2/s. n is the concentration in units of mol/m^3 and x is position in units of m. The negative sign of the equation indicates that the diffusion flux and the concentration gradient are in the opposite directions.

The diffusivity in solid is a temperature dependent parameter and is found to be well-described by the Arrhenius equation:

$$D = D_0 e^{-E_a/(kT)} \tag{6}$$

where E_a is the activation energy, *k* is Boltzmann's constant, *T* is the absolute temperature and D_0 is the pre-exponential factor.

Fick's second law is a derivation of the first law, which describes how the concentration changes as a function of time in a non-steady state conditions (concentration changes with time).

$$\frac{dn}{dt} = -D\frac{d^2n}{dx^2} \tag{7}$$

In addition to diffusivity, another useful term to describe conduction in ionic conducting materials is mobility, which is the ability of charge carriers to move through a medium in response to the electric field. It is defined as Equation 8:

$$\mu = \frac{\upsilon_d}{E} \tag{8}$$

where υ_d is the velocity in units of m/s, *E* is the electric field in units of V/m, and μ is the mobility in units of m^2/Vs.

The relationship between diffusivity and mobility is described by Nernst-Einstein Equation:

$$D = \frac{\mu kT}{ze} \tag{9}$$

where e is the elementary charge and z is charge number per each charge carrier.

1.2.4 Factors Affecting the Ionic Conductivity

Incorporating Equation 1 and Equation 2 into Equation 3, the electrical conductivity can be expressed as Equation 10:

$$\sigma = \frac{J}{E} \tag{10}$$

where *J* is the current density in units of A/m^2. In a conductor, the current density is equal to the total amount of charge, *Q*, that travels though length *l* in unit time and unit area. Therefore, it can be expressed as:

$$J = \frac{Q}{At} = \frac{nzeAl}{At} = nzev_d \tag{11}$$

where *n* is the charge concentration of the material. Applying Equation 8 and Equation 11 to Equation 10, the ionic conductivity in a material can be further expressed as:

$$\sigma = nze\mu \tag{12}$$

Apply Nernst-Einstein equation into Equation 12, we have:

$$\sigma = \frac{nz^2e^2D}{kT} \tag{13}$$

Therefore, from Equation 12 and Equation 13, the important factors that affect the conductivity in solid oxide can be obtained. This includes temperature (*T*), charge carrier concentration (*n*) and the diffusivity/mobility of ions (*D* or μ). Similar as diffusivity, ionic mobility is also a thermally activated parameter, as can be expressed as Arrhenius equation:

$$\mu = \mu_0 exp(-\frac{E_a}{kT}) \tag{14}$$

Some conclusions can be obtained from the above derivations. To optimize the ionic conductivity, high operating temperature is desired, because *D* or μ increases exponentially with increasing temperature. That is why most of the ionic conductors in solid oxide fuel cells are operating at above 800 °C. However, high temperature often creates problems such as high degradation rate due to high electrochemical reactivity and poisoning effects, and high mismatch due to the difference in thermal expansion coefficient of different components.

Another way to optimize ionic conductivity is to develop new materials or dopant elements that can decrease the activation energy. Proton conducting solid oxide fuel cell has been attracted great attention in recent years mostly because that the proton conduction often exhibits much lower activation energy than oxygen ion conductors, allowing better conductivity at intermediate temperatures (400-700 °C). Ionic concentration also needs to

be taken into consideration, because the conductivity linearly increases with increasing concentration of charge carriers that transport in the material.

However, these factors cannot be optimized at the same time, and improving one parameter often is in compromise to another parameter. For example, there is a trade-off effect of the proton concentration and the activation energy: increasing dopant concentration increases the amount of defects and thus ionic concentration *n*; on the other hand, the stronger trapping effect of dopants increases the activation energy that traps the ions stronger, impeding the conduction. As another example, while operating at high temperature is good for conductivity due to higher charge mobility, further increase the temperature at above 700 °C in proton conductors does not result in higher conductivity, due to the proton dissociation from the material at this temperature.

1.3 Solid Oxide Fuel Cells

1.3.1 Introduction to Fuel Cells

A fuel cell is an electrochemical device that directly converts chemical energy into electric energy.[3, 12] Fuel cells are different from batteries in that they only convert energy and fuels are required to be continuously supplied from other source, while batteries store chemicals as energy source.

From historical perspective, fuel cell was invented nearly 2 centuries ago. In 1839, Sir William Robert Grove invented an electrochemical device, where hydrogen and oxygen are supplied to a series of electrodes emerged in solutions. He called his invention “gas voltaic battery”, which was the first prototype of fuel cell. The name “fuel cell”, however,

was from Mond & Langer, who invented the device in 1889 and achieved a current density up to 0.2 A/cm^2. However, full cells have not come into real use until in the 1960s. During 1961 to 1969, NASA began to use fuel cells in the spacecraft computers and life-supporting systems in Apollo Project, because they were safer than nuclear energy resources and smaller than solar cells. In addition, the astronauts drank the water produced from the electrolysis. Since then, fuel cells have been used in many other applications. In the past few decades, thousands of studies have been focused on improving the energy density and reliability of fuel cells. With much better performance, fuel cells are used for energy source of vehicles, and primary and backup power for commercial, industrial and residential buildings in remote or inaccessible areas.

A typical fuel cell consists of anode electrode, cathode electrode, and an electrolyte between the electrodes. The working principle of a fuel cell is illustrated in Figure 1-2. The reacting gases, for example hydrogen and oxygen are supplied to the electrodes. Oxygen molecules are reduced in the cathode, generating oxygen ions that are transported through the electrolyte. They react with hydrogen molecules supplied in the anode, generating water as the only exhaust product. Meanwhile, the electrons are transported through the outer circuit, providing power to the load.

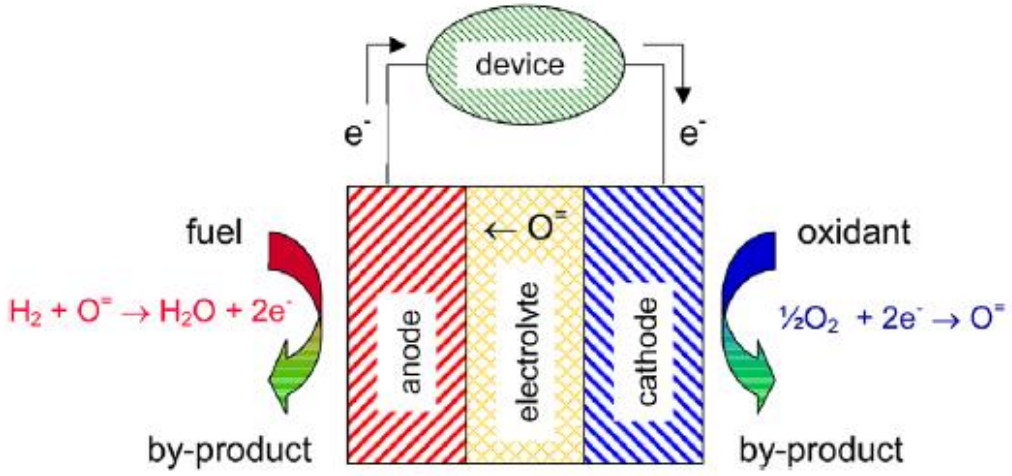

Figure 1-2 – Schematic of fuel cell working principle.[13]

Fuel cells are advantageous over other types of energy generating devices. Compared with the combustion engines, which have fuel conversion efficiency less than 40% due to the limitation of Carnot cycle, fuel cells offer a direct conversion from fuel to electricity, making it much higher efficiency (>60%) than most of the other power sources. Fuel cells are also clean and low-noise devices which are desirable for modern applications.

Fuel cells are usually categorized according to their electrolytes used, shown in Table 1-1. The electrolyte determines the electrochemical reactions, operating temperatures and applications.

Proton exchange membrane fuel cells (PEMFCs), alkaline fuel cells (AFCs) and phosphoric acid fuel cells (PAFCs) work at low temperatures (room temperature to 200 °C). Therefore, they have rather simple structures compared to other types of fuel cells operating at higher temperatures. However, working at low temperatures requires complicated and high-performance catalysts and electrodes, leading to relatively high cost, which is a major drawback of these fuel cells. For example, platinum is usually used in

PEMFC. Due to the low operating temperature, they have potential applications as power sources for small energy devices and vehicles.

Table 1-1 – Types of fuel cells.

Fuel Cell Type	Mobile Ion	Electrolyte	Operating temperature, °C	Applications
AFC	OH^-	KOH	50-200	Space vehicles
PEMFC	H^+	Nafion	30-100	Mobile application, lower power systems
PAFC	H^+	H_3PO_4	100-200	Large systems
MCFC	CO_3^{2-}	Li_2CO_3 Na_2CO_3	600-700	Up to MW systems
SOFC	O^{2-}/ H^+	ZrO_2/Y_2O_3	500-1000	Multi kW systems, power plants

Proton exchange membrane fuel cells (PEMFCs), alkaline fuel cells (AFCs) and phosphoric acid fuel cells (PAFCs) work at low temperatures (room temperature to 200 °C). Therefore, they have rather simple structures compared to other types of fuel cells operating at higher temperatures. However, working at low temperatures requires complicated and high-performance catalysts and electrodes, leading to relatively high cost, which is a major drawback of these fuel cells. For example, platinum is usually used in PEMFC. Due to the low operating temperature, they have potential applications as power sources for small energy devices and vehicles.

Molten carbonate fuel cells (MCFCs) and solid oxide fuel cells (SOFCs) work at higher temperatures. They use less expensive nickel or perovskite oxide as catalytic materials, due to increased temperatures and thus electrochemical reactivity. Aside from their function as the catalysts, they work as well as part of the electrode. Due to the high operating temperature, these fuel cells are not easy to start and stop. Therefore, they are often used as a continues energy source, such as an alternative of a power grid.

1.3.2 Solid Oxide Fuel Cells

As stated previously, SOFC is a type of fuel cell that utilizes ionic conducting solid oxides as electrolytes. In a typical SOFC, an oxygen ion conductor, yttrium stabilized zirconia (YSZ), containing typically 8-10 mol% Y, is used as electrolyte; a porous ceramic-metal composite of Ni and YSZ (typically 1:1 NiO-YSZ weigh ratio) is used as anode; and $La_{1-x}Sr_xMnO_{3-\delta}$ (lanthanum strontium manganite or LSM, x is typically between 0.15-0.25) is used as cathode. During operation, the SOFC is heated up to 800-1000 °C. Air will be supplied though the cathode, and oxygen molecules interact with cathode/electrolyte interfaces, acquiring electrons and generate oxygen ions. The oxygen ions then diffuse through the electrolyte side into the anode side. On the anode/electrolyte interface, the oxygen ions will catalytically react with the fuel, such as methane and carbon monoxide, generating water and/or carbon dioxide. The electrons are transported through the outer circuits, generating electric power. SOFCs electrolytes not only operate as oxygen ion conductors: some electrolytes are proton conductors, or even exhibiting both types of conduction. The electrochemical reactions are widely believed to occur at triple phase boundaries (TPBs), which are defined as the sites where gas phase, electrolyte (ionic conductor) and electrode (electron conductor) occur. Any breakdown of the TPBs will limit

the reactivity of the electrode reactions. Factors such as microstructure and composition greatly affect the size and distribution of the TPBs, which is crucial in determining the SOFC performance.

Besides the advantages as being a fuel cell stated previously, SOFC is also superior to other types of fuel cells in several aspects. Firstly, cheaper catalysts are used in SOFCs, which greatly reduces their cost. Secondly, operating at high temperatures, they are able to use a wider selection of fuels, without previous external reforming. Thirdly, the exhaust vapours can be further used for collecting electricity, which provides even higher efficiency than other fuel cells. In addition, SOFCs also have longer cell life expectancy due to higher impurities (e.g. sulphur) tolerance.

However, SOFCs still have some disadvantages that limit their commercialization. Due to the high electrolyte resistance for ionic conduction, high operating temperatures, often above 800 °C is required for most of the traditional SOFCs, which results in severe degradation and causes reliability issues. High electrode polarization is another disadvantage, which is due to the relatively low electrochemical reactivity, especially at the cathode. This leads to a high internal resistivity that results in a decreased working potential. To overcome these challenges, a number of studies have been focused on SOFCs aiming to lower the operating temperatures or the inner resistance. Generally, there are three ways to improve the SOFC performance:

1. Developing new materials systems. Researchers are actively looking for electrolyte materials that exhibit higher ionic conductivity, which can allow comparable performance when operating at lower temperatures.[14, 15] New

cathode materials and catalysts with higher performance are also being developed. For example, proton conducting oxides are considered promising electrolytes for SOFC, due to their lower activation energy for ionic transport.[7, 16] In addition, mixed ionic-electronic materials are being developed as electrode materials, which provide extended electrochemical reactions sites, increasing the reactivity of electrode reactions and reducing the total potential drop during operation.

2. Developing advanced microstructures of SOFC components. Although using same materials, the efficiency may change, due to the accessibility of the gas into the reaction site. For example, porous electrodes are preferred for better interaction between gas and electrode/electrolyte interfaces, which overcomes the gas deficiency problem when operating at high power. However, porous structure has lower strength, which may cause pulverization over time, reducing the performance. Therefore, research has been focused on designing nanometer-sized electrodes for higher surface area, meanwhile maintaining similar strength and reliability.[17]
3. Designing advanced SOFC structures for better performance and reliability. This is an engineering problem, an important step for large-scale production. So far, SOFC have mainly three different configurations, tubular, planar and monolithic. However, detailed design can be optimized to ensure the uniformly distribution of temperature in a SOFC: high local temperature may cause severe degradation of the fuel cell component, decreasing the total operating hours;

lower operating temperatures, on the other hand, decreases the power output and efficiency.

In this thesis, we will mainly focus on the first way to improve SOFC performance, and several promising oxides are chosen for ionic dynamics study. Traditional and new materials for solid oxide electrolytes are introduced in the following.

1.3.3 Materials for Solid Oxide Electrolytes

As previous introduced, developing good solid oxide electrolyte is crucial in decreasing operating temperature, thus greatly reduce the cost and improve the performance of a SOFC. Some of the properties for designing new types of electrolytes include:

1. High ionic conductivity
2. Low electric conductivity
3. Structural stable under working temperature (no phase transformation, compositional change or pulverization)
4. Chemically stable under fuel and oxidant environment
5. Thermal compatibility with other fuel cell components (thermal expansion coefficient match)

The materials used for SOFC electrolyte are generally categorized into two basic types: oxygen ion conductors and proton conductors, both have its advantages and disadvantages, as detailed in the following.

1.3.3.1 Oxygen Ion Conductors

1. Fluorite-structured oxides

Traditional oxygen ion conducting material for SOFC applications are based on fluorite structure, AO_2, including zirconium oxide (ZrO_2) and cerium oxide (CeO_2). The fluorite crystal structure is illustrated in Figure 1-3, where the cations occupy the face-centered positions and anions occupies the tetrahedral sites between them. With acceptor dopants, oxygen vacancies are generated, enabling oxygen vacancies to migrate in the lattice, as shown in Equations 15 and 16 (Kröger-Vink notation), where M is a divalent dopant and R is a trivalent dopant.

$$V_A'''' + 2V_O^{\cdot\cdot} \overset{MO}{\Leftrightarrow} 2M_A'' + O_O^x + V_O^{\cdot\cdot} \tag{15}$$

$$2V_A'''' + 4V_O^{\cdot\cdot} \overset{R_2O_3}{\Longleftrightarrow} 2R_A' + O_O^x + V_O^{\cdot\cdot} \tag{16}$$

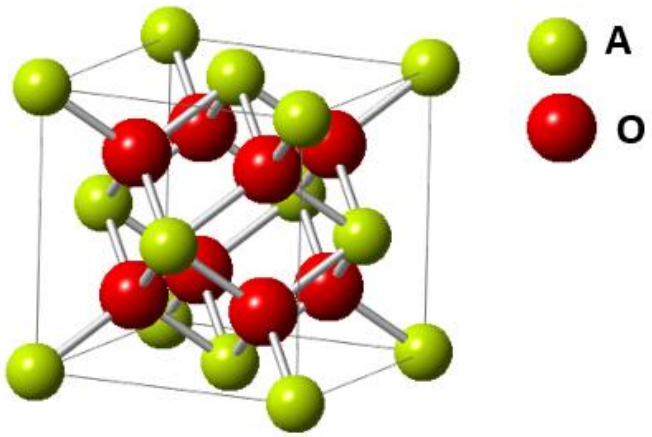

Figure 1-3 – The fluorite crystal structure (AO_2). Red spheres represent O^{2-} ions and yellow spheres represent A^{4+} ions.

In SOFC applications, the most widely acknowledged electrolyte is zirconia, with 8-10 mole % of yttrium dopant, forming yttrium-stabilized zirconia, or YSZ. The word "stabilize" means that such dopant can help such crystal structure maintain the fluorite phase at high temperature: without yttrium, pure zirconia only adopts cubic fluorite structure at above 2300 °C.

Ceria based material, with typical dopants including Gd_2O_3 and Sm_2O_3, is another fluorite system widely studied for SOFC applications.[14, 18] Compared to its zirconia counterparts, ceria based material displays better ionic conductivity in lower temperatures (500 – 800 °C), so it is potential electrolyte for the development of intermediate temperature SOFCs. However when operating, especially under reducing environment, it shows some electric conductivity due to self-reduction, which is detrimental to the efficiency of SOFCs. Detailed introduction of ceria is introduced later in this thesis.

2. Perovskite-structured oxides

Perovskite structure, shown in Figure 1-4, is another type of structure that is widely used as SOFC electrolytes.[11, 16] Although the name perovskite was originally used to describe $CaTiO_3$, it is commonly used today to describe a more general group of oxides with a similar structure, ABO_3, where the A site cation is a metal with +2 or +3 valence state, and the B site cation is a different metal with +4 or +3 charge, respectively. The A site cation is usually bigger than B cation, surrounded by 12 nearest oxygen ions, and the B site cation forms an octahedron with six nearest oxygen ions surrounding it. Perovskite structure allow stoichiometric changes by dopant, creating a wide range of properties, such

as magnetic, electrical optical and catalytic. Due to the tunable electron structure, perovskites can vary from insulating material to superconductor materials.

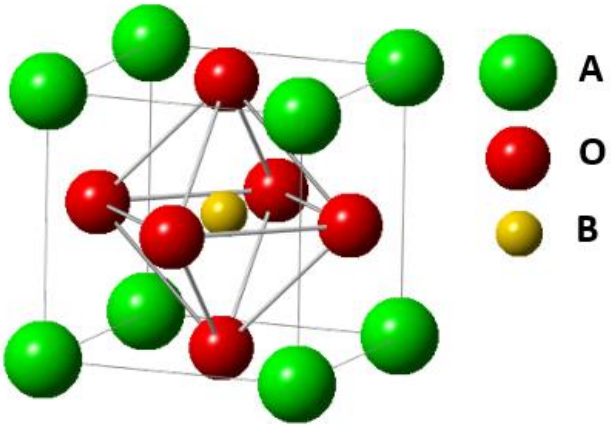

Figure 1-4 – The perovskite crystal structure (ABO_3). Green and yellow spheres represent two types of cations, and red spheres represent O^{2-} ions.

3. Other types of oxygen ion conductors

Besides fluorite- and perovskite-based materials, there are also plenty of studies focusing on the development of other material systems that have higher oxygen ion conductivities or lower operating temperatures than traditional YSZ.[14] Some of these materials include $La_9Sr(SiO_4)_6O_{2.5}$, $La_2Mo_2O_9$ (LAMOX) and apatites. However, they are still facing challenges before widely applied into SOFC. For example, $La_9Sr(SiO_4)_6O_{2.5}$ is difficult to synthesize; LAMOX undergoes a phase transition to a highly conducting phase at 580 °C, but suffers from chemical and thermal incompatibility with electrode materials. These drawbacks need to be overcome before widely applied in SOFC electrolytes.

1.3.3.2 Proton Conductors

Proton conducting oxides are another type of materials that can be used as SOFC electrolytes. Water is generated at the anode in oxygen-conducting SOFCs, which dilutes the fuel and reduces the Nernst potential. However, proton-conducting SOFCs overcome this problem. In addition, proton conducting oxides usually have lower activation energy, and therefore exhibit relatively high conductivity at intermediate temperatures. Although the research of proton conducting oxides is still in an early stage compared with oxygen conducting counterparts, they have shown great potential in lowing the operation temperature and improving the efficiency.

1. Intermediate-temperature proton conductors

With proper acceptor doping, perovskite-type oxides have been shown to exhibit high proton conductivity at intermediate temperatures (400-700 °C).[7] This phenomenon was first discovered three decades ago by Iwahara et al.,[19] who showed cerate perovskites exhibiting proton conducting in humid air. Since then, proton conducting oxides have been widely investigated, such as barium zirconate ($BaZrO_3$), barium cerate ($BaCeO_3$) and strontium cerate ($SrCeO_3$).[4, 13, 20]

Kreuer et al. have investigated a variety of different proton conducting oxides, as shown in Figure 1-5.[7] These materials show Arrhenius behavior of proton conductivity from 200 °C to 800 °C. At higher temperatures, the proton conductivity drops drastically due to dehydrating of the materials. From the figure, the materials that shows the highest proton conductivity are mostly perovskites.

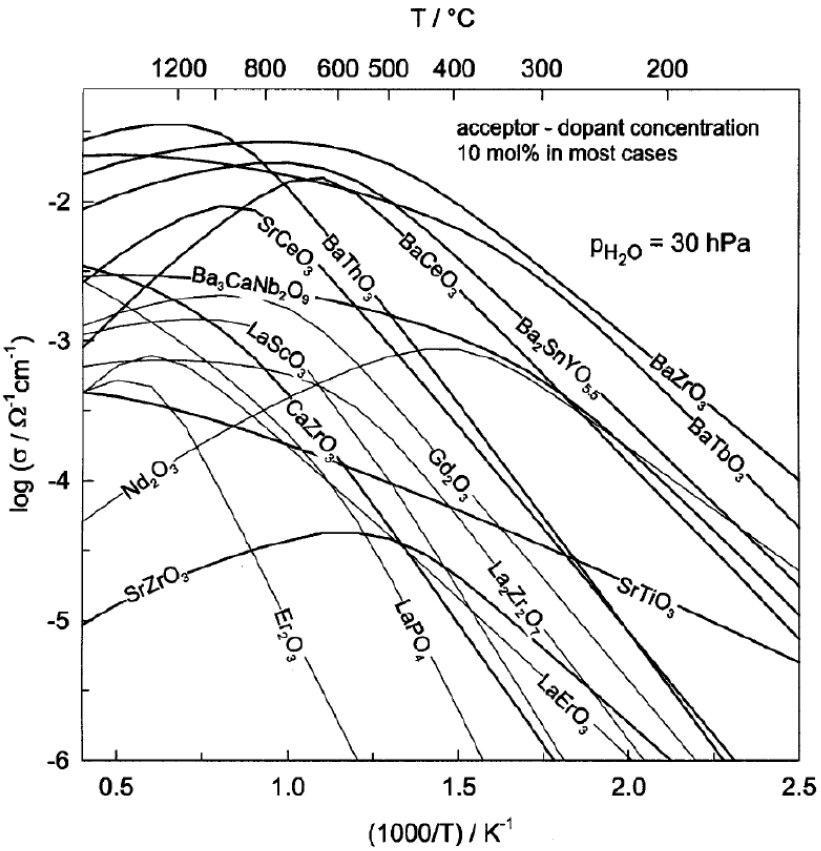

Figure 1-5 – Proton conductivities of various oxides as calculated from data on proton concentrations and mobilities.[7, 21]

In these proton conduction perovskites, protons are created as interstitial defects. Take Y-BZO as an example, the introduction of trivalent dopant Y induces oxygen vacancies in the crystal structure. In Kröger-Vink notation,[22] this can be written as Equation 17. In dry conditions, oxygen vacancies provide the charge compensation for the acceptor dopants. However, the material is hydrated when it is supplied with water or hydrogen. For example, oxygen vacancy can be filled with a water molecule from ambient, dissociating into a hydroxyl group and a proton. The proton forms a covalent bond with a lattice oxygen ion (Equation 18).

$$Y_2O_3 \xrightarrow{ZrO_2} 2Y'_{Zr} + 3O_O^{\times} + V_O^{\cdot\cdot} \quad (17)$$

$$H_2O(g) + V_o^{\cdot\cdot} + O_o^{\times} \Leftrightarrow 2OH_o^{\cdot} \quad (18)$$

The proton transport in perovskites is then enabled through a Grotthuss mechanism, as opposed to the vehicle mechanism. The vehicle mechanism is the transport of hydronium or hydroxyl groups as a whole, which is usually encountered in aqueous solutions and polymer membranes. In solids, such as perovskites, vehicle mechanism is limited and Grotthuss mechanism is the main transport mechanism. Grotthuss mechanism includes two elementary steps, as shown in Figure 1-6: (1) proton transfer between adjacent oxygen atoms through breaking and reforming hydrogen bonds; and (2) rotation of hydroxyl group in between such transfers. The long-range distance of the proton transport is believed to go through a series of such transfers and rotations. The overall proton transport rate is dependent on the energy barriers of each step. The dopant site is believed to act as a trap for protons, which results in an increase of energy barrier.[23] In these proton-conducting perovskites, protons are not part of the crystal structure, but are interstitials in the lattice, in equilibrium with the ambient water vapor. Therefore, the proton incorporation and concentration within the crystal and the resulting proton conductivity is largely affected by the ambient gas, humidity and temperature. For instance, since proton incorporation is found to be an exothermic reaction,[24] higher temperature will result in a reversible loss of protons.

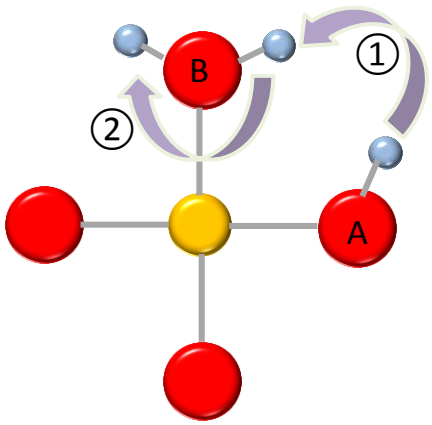

Figure 1-6 – Sketch of Grotthuss proton transfer mechanism from the oxygen ion A to oxygen ion B.

Phosphates are another type of materials that exhibit proton conduction, such as $LaPO_4$.[25] When doped with Ca or Sr, they show proton conductivity up to ~800 °C. Brownmillerite structure such as $Ba_2In_2O_5$ is another material that shows proton conductivity. With the presence of intrinsic oxygen vacancies, the conductivity can achieve for example 1.12×10^{-5} S/cm at 400 °C.[26]

2. Low-temperature proton conductors

Low-temperature (<300 °C) proton conduction has been found in a number of metal oxides, such as yttrium-stabilized ZrO_2 (YSZ),[27-32] yttrium-doped barium zirconate,[23, 33] titania,[34] and doped and undoped ceria.[35-40] While at inter-mediate temperature range, proton conducting are mostly enabled though transporting along the lattice, at low temperature range, water from the ambient can condense on the surface and grain boundaries, and more routes are available for proton conduction, including chemisorbed water layer on the surface, physisorbed water layer that are in immediately approximation to the oxide, and though the inner bulk. Given that protons are not a structural element in

such crystal systems, and are very small in size, proton conductivity of these systems is extremely sensitive to the environment and defect structures. In fact, with varying environmental conditions – e.g. temperature, humidity and atmosphere – multiple proton conduction mechanisms have been reported in ceramics such as YSZ and TiO_2.[27, 30, 34]

1.4 Solid State Gas Sensors

1.4.1 Gas Sensors

Gas detection and monitoring is important in a number of industrial and domestic activities.[41-44] For example, flammable gas and toxic gas should always be monitored to prevent fire or other safety issues. In chemical industry, the concentration of different gas should also be monitored in order to insure the quality of the final product. The exhaust of factories or vehicles need to be monitored to reduce pollution. A gas sensor, which is a device that detects the presence of gases in an area, finds applications in these areas. In recent years, there is a growing demand of gas sensors with higher sensitivity, selectivity and reliability, as the need to protect the environment has grown.[45-47]

The gas sensor work by measuring a physical property changed by adsorption/desorption processes or chemical reactions on the surface of a gas-sensitive material. Typically, gas sensors are produced to detect a single gas, such as CO, CH_4, H_2, SO_2, etc. Newer development of gas sensors also allows detection of several gas, or even a combination of a mixed gas.

Based on the operating mechanisms, gas sensors can be classified into physical process based sensors and chemical process based sensors. The previous category utilizes

physical property of the gas, including energy adsorption (infrared point gas sensors), ionization (photoionization gas sensors), acoustic characters (ultrasonic gas sensors), etc. The latter usually include chemical reactions between gas and sensor materials, such as electrochemical sensors, semiconductor sensors, etc.

Infrared (IR) point gas sensors use IR light that pass through a known volume of gas.[48-51] At certain frequency, some of the energy of IR light will be adsorbed by the gas. The amount of energy loss is proportional to the gas concentration. By comparing the energy change at certain frequency before and after passing though the gas, the concentration of the target gas can be determined.

Photoionization gas sensors use an ultraviolet (UV) light to ionize the target gas.[52-54] If the compound has an ionization energy below that of the UV energy, the gas will be ionized, generating electrons that is detected by the current change.

Ultrasonic gas sensors detect the background noise of the environment.[55-58] Because most high-pressure gas leaks generate ultrasonic sound, these sensors are able to pick up these frequencies from the background noise, determining whether or not there is a gas leak.

Semiconductor gas sensors detect the concentration of target gas though chemical reactions that take place on the surface of sensor material.[59-62] The electrical resistance in the sensor material will change when interacting with gas, and is used to calculate the gas concentration.

Electrochemical gas sensors measure the concentration of a gas though electrochemical reaction.[63-66] In a typical electrochemical gas sensor, electrochemical reactions are taking place on electrode with the presence of the target gas. The target gas is either chemically oxidized or reduced, generating ions that diffuse though the working material. Meanwhile electrons transport through the outer circuit, which is detected though an ampere meter. Thus, the amount of current produced is indicative of how much of the gas is reacted at the electrode, indicating the gas concentration.

There are a lot more types of gas sensors not introduced here. However, all of them are based on detecting a physical change due to the gas or gas/sensor interaction. They are summarized in Table 1-2.

Table 1-2 – Types of gas sensors and the corresponding principles.

Types of gas sensors	Physics detected
Infrared point gas sensors	Energy adsorption by target gas
Photoionization gas sensors	Current change due to ionization of target gas
Ultrasonic gas sensors	Background noise change due to gas leakage
Semiconductor gas sensors	Electrical resistance change when contacting with the target gas
Electrochemical gas sensors	Current change due to electrochemical reactions
Catalytic gas sensors	Voltage or temperature change
Field effect gas sensors	Work function change

1.4.2 Solid Oxide Gas Sensors

In contrast to the physical process based gas sensors, chemical sensors, which detect the gas by means of a selective chemical reaction with a reagent, mainly utilize solid-state chemical detection principles. Solid oxide gas sensors are one of the best candidate for commercial gas sensors, and have a wide range of applications. Compared to other types of sensors, they have numerous advantages, like small sizes, high sensitivities in detecting very low concentrations.

1.4.2.1 Semiconductor Gas Sensors

Semiconductor gas sensors are typically based on metal oxides. Since the 1920s, studies have shown that the semiconductor material surface is highly sensitive to chemical reactions, and result in a dramatic change of charge carrier concentration. Such metal oxides include Cr_2O_3, Mn_2O_3, NiO, CuO, SrO, In_2O_3, WO_3, TiO_2, V_2O_3, Fe_2O_3, GeO_2, Nb_2O_5, MoO_3, Ta_2O_5, La_2O_3, CeO_2, Nd_2O_3. Most of them are transition metal oxides, due to their higher sensitivity and easier conductivity measurements. Table 1-3 summarizes selected metal oxides for semiconductor gas sensors.

Table 1-3 – Summary of selected materials reported for semiconductor gas sensors.

Material	Target gas	Operating temperature (°C)	Reference
CeO_2	Ethanol/NO_2	200	[67]
	O_2	700-1000	[68]
Cr_2O_3	H_2	450	[69]
	Ethanol/Isopropanol/Acetone	N/A	[70]
CuO	NO_2	200	[71]

Table 1-3 continued

Fe_2O_3	Acetone/Acetic acid/Ethanol/etc.	150	[72]
In_2O_3	Ethanol/Formaldehyde	25	[73]
La_2O_3	Ethanol	300	[74]
Nb_2O_5	H_2	440	[75]
NiO	Formaldehyde	600	[76]
	H_2S/Ethanol/NO_2	150	[77]
SnO_2	NO_2	280	[78]
Nd_2O_3	CO/CO_2/Ethanol	300-400	[79]
TiO_2	NH_3	25-500	[80]
	O_2/H_2/Ethanol	300-400	[81]
	NO_2/CO	190/170	[82]
WO_3	H_2S/NH_3/Ethanol/CS_2/CH_3CN/etc.	400	[83]
	NO_x	200-500	[84]

1.4.2.2 Electrochemical Gas Sensors

Electrochemical gas sensors typically consist of an ionic conducting electrolyte sandwiched between two electrodes. Reducible gases, such as O_2, Cl_2, CO_2 and NO_2 obtain electrons at the cathode, while oxidizable gases such as CO, H_2S and CH_4 give away electrons at the anode. They form ions that are transported through the electrolyte. Detailed sensor information are summarized in Table 1-4.

Table 1-4 – Summary of selected materials reported for electrochemical gas sensors.

Material	Target gas	Operating temperature (°C)	Reference
$SmFeO_3$	CO/NO_2	200-450	[85]
La_2NiO_4	Methanol	300-460	[86]
$Ba(TiLa)O_3$	CO	175-400	[87]
$Ba(ZrY)O_3$	H_2O	400-700	[88]
$LaFeO_3$	Methanol	400-500	[89]
$BaSnO_3$	$O_2/CO/NO_2$	400-700	[90]
YSZ	H_2	500	[91]
$La(NiFe)O_3$	Ethanol	270	[92]
$LaMnO_3$	Methanal/CO	N/A	[93]

1.5 Ionic Conducting Oxides

As introduced previously, ionic dynamics in oxides are crucial in a number of electrochemical applications such as SOFCs and gas sensors. Ceria and Y-BZO are two promising candidates for these applications. As a result, they are chosen in this thesis study. Here these two materials are introduced in details.

1.5.1 Nanostructured Ceria

Stoichiometric ceria has a cubic fluorite structure over a wide temperature range. Each Ce^{4+} cation is surrounded by eight equivalent nearest O^{2-} anions forming corners of a cube, and each O^{2-} anion is surrounded by a tetrahedron of four cerium ions. Typically, ceria is an insulator, but doping of trivalent atoms such as Gd^{3+} can create a large amount

of oxygen vacancies in the lattice (Equation 19), while keeping the fluorite structure mostly unchanged. Doped ceria shows excellent oxygen ion conductivity at intermediate to high temperatures (500-1000 °C), and therefore is a promising candidate as an electrolyte for SOFCs.[14]

$$2V_{Ce}'''' + 4V_O^{\cdot\cdot} \overset{Gd_2O_3}{\Longleftrightarrow} 2Gd_{Ce}' + O_O^x + V_O^{\cdot\cdot} \tag{19}$$

Nanostructured ceria (NC) is, however, a mixed ionic-electronic conductor (MIEC), and has been widely studied as electrolyte for water-gas shift catalyst,[94] SOFCs,[95-98] and gas sensor active components.[68, 99, 100] Most of these applications are based on the ability of NC to conduct O^{2-} ions, as well as store and release oxygen from the crystal structure through oxidation and reduction reactions, as shown in Equation 20.

$$2Ce^{4+} + O_O^x \Leftrightarrow 2Ce^{3+} + V_O^{\cdot\cdot} + \frac{1}{2}O_2 \tag{20}$$

The property to reversibly adsorb and release oxygen is often referred to as "oxygen storage capacity", or OSC. This unique property in NC ensures its ability to strongly catalyze redox reactions, and the ability to serve as a solid-state oxygen buffer for redox reactions.

Besides oxygen ion conduction, at low temperature, NC also exhibits proton conduction. Generally, porous materials are found to adsorb moisture due to their high surface areas. Therefore, the dependence of relative humidity on the conduction behavior of materials has been widely studied decades ago. As an example, Gerhardt et al. have performed fundamental studies on the humidity effect of porous silica gels/thin films via

EIS.[101-104] Similarly, water molecules can be adsorbed on NC surface or grain boundary areas, which may strongly affect the conduction property of NC.[105-108] Under electric field, water may split into protons and/or hydroxyl groups, allowing additional conduction pathways on NC. While it is believed that the proton conduction of NC is controlled by the nanoscale details of the NC structure, the direct correlation of the NC's microstructure with conduction properties is still not fully understood.

The oxygen vacancy that is abundant in NC and the oxidation state of Ce cations play a vital role in determining the catalytic and transport properties of the materials, and underpins its fundamental applications. Therefore, interaction between the NC surface defects and chemical species that is present in atmosphere or surface such as water, oxygen and peroxo groups has been intensely studied.[105, 107, 109-111] However, the surface electrochemical behavior is a complex process, with multiple reaction steps and transport pathways. As a result, there is still no consensus with respect to the principle mechanisms governing MIEC conductivity in NC. Zhang et al. [112] gave an amount of anisotropic oxygen conductivity behavior, in which the cubic (100) ceria facets result in high OSC, whereas Molinari et al.[106] and Maier et al. [113] have reported a proton-based conduction on the surface or open pores area facilitated by either water adsorption or surface defects as catalytic sites. In addition, questions also remain on whether proton transport pathways involve grain boundaries,[35, 36, 38, 40] or air-exposed surfaces and residual pores.[35, 37]

The electrochemical reactivity of NC and subsequent transport processes are also greatly affected by TPB, which is the interface of NC, electrode and gas phase.[114, 115] As an example, ceria with embedded Pt group metal particles is reported to show great enhancement of catalytic activity in water-gas shift reactions.[116] The metal/NC interface is

also an active site for low-temperature CO oxidation.[117] The electrochemical reactions such as water-gas shifting and water splitting that take place at the TPB are expected to be highly sensitive to the environment, since one or more reactants or products come from the ambient, to which the electrochemical processes often have direct access. Thus, the effects of environmental conditions and the role of TPBs in water-NC surface interactions need to be studied in details. These ionic dynamics on the nanoscale are crucial to the development of high-performance ceria biased electrochemical devices, and thus calls for further investigation.

1.5.2 Yttrium-Doped Barium Zirconate

A longstanding aim of proton conducting perovskites is to find proper dopants and preparation methods that exhibit both high proton conductivity and good chemical stability, for energy applications such as electrolyte in proton conducting SOFCs. $BaCeO_3$ based materials have exceptionally high proton conductivity; for example, Gd doped $BaCeO_3$ exhibits a proton conductivity as high as 0.05 S/cm at 600 °C.[118] However, the commercial realization of such proton conductors has been substantially hampered because of their instability under CO_2 and/or H_2O containing environment (Equation 21 and 22), which is inevitable in fuel cell operation. This reactivity causes severe degradation of the material and precludes the applications of electrochemical devices in severe conditions, such as proton conducting SOFCs.

$$BaCeO_3 + CO_2 \rightarrow BaCO_3 + CeO_2 \quad (21)$$

$$BaCeO_3 + H_2O \rightarrow Ba(OH)_2 + CeO_2 \quad (22)$$

In contrast, $BaZrO_3$ based material has very good chemical stability in the same operating environments, making it a promising material for energy applications. According to Kreuer' review on proton conduction oxides, among all the materials studied, yttrium doped $BaZrO_3$ (Y-BZO) has shown the highest conductivity.[7] Therefore, Y-BZO has been widely studied in the past decade. It is worth noting that the earliest studies of Y-BZO in the early 1990s suggested that this material exhibits poor proton conductivity. This conclusion was revised in 1999, when Kreuer reported that the proton conductivity of Y-BZO is $\approx 5 \times 10^{-5}$ S/cm at just 140 °C. Although theoretically Y-BZO exhibits superior bulk proton conductivity, most of the reported proton conductivities of Y-BZO are much lower than the theory value and are inconsistent.[119] This discrepancy is likely originated from the presence of extended defects in Y-BZO lattice. Due to the high refractory nature of this material, high temperature sintering (T_{sint}>1700 °C) is often needed to obtain high density samples. However, grain boundaries still largely remain, which have much lower proton conductivity than the inner grains. In addition, the high sintering temperature may also leads to Ba loss and emergence of lower conductivity phases (Y_2O_3).[33] This challenge has largely limited the future development of Y-BZO as proton conducting electrolytes.

It is reported by a number of researchers that the proton conductivity of grain boundaries in Y-BZO is several orders of magnitude lower than that of the bulk, and the activation energy for proton transport in is usually 0.7-1.0 eV, much higher than that reported for the bulk (0.4-0.6 eV).[120] It has long been speculated that the grain boundary resistance may be resulted from the space charges effects. The proton concentration is

much lower in proximity to the grain boundary core, where two crystals with different surface orientation join. Space charge zones form in this region, which is highly resistive to proton transport.[121-123]

To achieve proton conductivity that is close to its bulk value, different approaches have been developed to obtain high-density and large-grained materials at reduced sintering temperatures. Nanometer-sized sintering powder with excess barium is essential to avoid barium loss and achieve high density.[119] Inclusion of sintering aids such as ZnO,[124-126] CuO,[127, 128] NiO,[129] InO[130] and CaO[131] has been shown to effectively promote the sintering ability of doped BZO. However, the addition of sintering aids, in principle, is detrimental to the total proton conductivity, therefore the amount of sintering aids must be precisely controlled. Fabrication of $BaZrO_3$ and $BaCeO_3$ composites is also a strategy to combine the good chemical stability of the former and high proton conductivity of the latter.[132, 133]

Since the space charge layer in grain boundaries is likely the reason for low conductivity of Y-BZO, another approach to prepare high conductivity samples is to prepare Y-BZO sample with limited grain boundaries at relatively low temperature. Using pulsed later deposition (PLD), highly textured, grain-boundary-free Y-BZO films have been studied by several groups, and they not only show excellent proton conductivity (0.11 S/cm at 500 °C),[33] but also has potential use in the micro-sized proton conducting SOFCs.

The development of high and reproducible proton conducting Y-BZO necessitates elucidation of the fundamental mechanisms of ionic dynamics on the nanometer or atomic scale. Computational simulations such as density functional theory (DFT) and the

molecular dynamics (MD) are considered one of the most significant techniques. They have been successfully applied in a number of previous investigations to explain proton stability at interface,[134] proton diffusion,[135, 136] and the role of dopant in proton conduction.[137] On the other hand, experimental investigation of ionic dynamics at the same length scale is largely limited, with the characterization method being mostly electron microscopy and SPM technologies.[138] TEM is widely used as to analyze crystal structure, whereas EDX and EELS are spectroscopic methods in TEM, which can measure the local chemical composition of the sample.[139, 140] Recently Yang et al. used electrochemical strain microscopy (ESM) and STEM to show a correlation between the conductivity and the interface structural defects.[141] To understand the fundamental ionic dynamics underpinning its functionalities, further efforts are needed to uncover how conductivity is related to oxygen vacancy ordering and dopant concentration in Y-BZO. Furthermore, correlation between the computed and experimental data is crucial: experimental result is significant to build and validate model, and model can in turn guide effectively experiment through "discover by design".

1.6 Thesis Organization

Based on the literature reviews presented above, this thesis is organized as follows:

Experiment procedures and methods (Chapter 2)

This chapter describes the experimental techniques used for thin film deposition and structural characterization. The principles of techniques used for structural characterization and in-situ ionic dynamics measurement are introduced. Meanwhile, the

methods for finite element analysis and ab-initio calculations on the transport mechanisms are also presented.

Ionic dynamics of NC – the effect of external conditions (Chapter 3)

In this chapter, the ionic dynamics of NC thin films is investigated. The surface potential mapping as a function of distance and time is obtained on NC. The effects of temperature, humidity and applied bias on the surface potential mapping are studied, and the activation energy for the potential change are quantitatively compared. The possible transport species, electrochemical reactions and ionic conduction routes are discussed.

To identify the electrochemical reaction site taking place on NC, the behavior of exposed and non-exposed TPB are compared as a function of temperature and humidity. To understand the effect of ambient gas, the measurements were performed in nitrogen and oxygen atmosphere. The effects of external conditions, such as temperature, humidity, applied bias, ambient gas and the absence of TPB on the ionic dynamics are identified.

Finite element modeling of ionic dynamics of NC (Chapter 4)

The electrochemical reaction and ionic transport taking place on NC are then quantified via finite element analysis. Four physical parameters associated with these processes, i.e. proton injection rate at TPB (S), proton dissipation constant (f), proton diffusivity (D) and mobility (μ) are obtained via fitting to the experimental data at each environmental condition. The activation energy for charge injection and proton diffusivity processes are obtained and correlated with the experiment value. The environmental regimes for proton transport in NC are obtained, where proton generation and conduction

is enabled either through the surface physisorbed water layer or through the chemisorbed water, with possible catalytic support from oxygen vacancies.

Effect of microstructure on ionic dynamics of NC (Chapter 5)

The effect of microstructure on the ionic dynamics of NC is investigated at temperatures below 200 °C. Five NC thin films with different microstructures, including surface roughness, grain boundary density and orientation, were prepared by a variety of deposition methods. The proton generation rate and diffusivity is quantified for each sample at each environmental condition via finite element modeling. The correlation between these quantified ionic dynamics parameters and microstructures such as surface roughness, grain size and surface orientation are investigated.

Ionic dynamics study of grain-boundary-free Y-BZO (Chapter 6)

Energy discovery platforms are also used to study the ionic dynamics of Y-BZO. Stoichiometric Y-BZO thin films, both single crystal and polycrystalline, with dopant concentration ranging from 0% to 20% are prepared by pulsed laser deposition. The surface potential mapping is obtained as a function of temperature and humidity, and the conduction species and pathways are identified. The density functional theory analysis and lattice distortion analysis are performed as a function of dopant concentration, and is correlated with the activation energy for proton transport.

Effect of non-stoichiometry on proton conduction in Y-BZO (Chapter 7)

The effect of non-stoichiometry on the proton transport of Y-BZO is studied. The non-stoichiometry, or barium deficiency is created through annealing Y-BZO thin films at

high temperature. The local distortion and compositional analysis are performed at atomic scales. The activation energy for proton transport is obtained via surface potential mappings. The effect of barium deficiency on the proton transport is obtained through structural-property correlations.

Conclusions and future work (Chapter 8)

Finally, the thesis work and achievements are summarized in this chapter. Future work is also suggested to further understand the physical and chemical behavior of nano-devices through improved characterization capabilities via energy discovery platforms.

CHAPTER 2. EXPERIMENTAL PROCEDURES AND METHODS

This chapter presents the techniques used for NC and Y-BZO thin film growth and for characterizing the crystal structure, microstructure, composition and ionic transport properties. In addition, the theoretical analysis used for identifying the conduction mechanisms are also discussed.

2.1 Deposition of Proton Conducting Oxide Thin Films

2.1.1 NC Thin Films Deposition

In this work, NC thin films were prepared by chemical solution deposition (CSD), sputter deposition (SD) and pulsed laser deposition (PLD). Detailed deposition parameters are detailed as follows.

2.1.1.1 Chemical Solution Deposition

CSD is advantageous in that it allows preparation of thin films with good control of the composition and homogeneity. It is also simple to implement, with relatively low cost on equipment. In this work, NC thin films prepared by CSD were used as the main sample for proton transport studies, including the effect of external conditions study (CHAPTER 3) and the effect of microstructure study (CHAPTER 5).

The preparation of NC thin films through CSD is achieved via four steps: 1) preparation of ceria precursor; 2) preparation of substrates used for CSD of NC thin films; 3) spin coating of ceria precursor on substrates; 4) heat treatment of the coated films. They are detailed in the following description.

The NC precursor preparation and deposition procedure was based on previous literatures.[18, 142-146] A 0.2 M ceria precursor was prepared by dissolving 4.342 g of $Ce(NO_3)_3 \cdot 6H_2O$ (Sigma-Aldrich, Inc.) into 47 mL of ethylene glycol (Sigma-Aldrich, Inc.) in glove box, followed by mixing at 80 °C in an oil bath for 3 days.

For most of the studies, Si substrate coated with a layer of Si_3N_4 was used for CSD growth of NC thin films. Silicon substrates were chosen because they are compatible with most of the commercial MEMS devices and circuits and therefore are expected to have a number of practical applications. In addition, as the etching process for Si is well developed, such devices can be further used to fabricate freestanding membranes for *in-situ* transmission electron microscopy (TEM) characterization of electrochemical processes. However, the transport characterization of NC such as time-resolved Kelvin probe force microscopy (tr-KPFM) and electrochemical impedance spectroscopy (EIS) in this thesis requires insulating substrates. Therefore, Si_3N_4 insulating layer was deposited on Si wafer, before the deposition of NC thin films.

Si (100) substrate was purchased from Nova Electronic Materials Inc. and the thickness was 500 μm. An insulating Si_3N_4 layer (≈500 nm thick) was deposited onto Si substrate by low-pressure chemical vapor deposition (LPCVD). The LPCVD of Si_3N_4 films was processed in a Tystar diffusion furnace in a mixture of NH_3 (17 sccm) and H_2SiCl_2 (100 sccm), and the total pressure was kept at 158 mTorr. The deposition temperature was 835 °C.

Besides Si/Si_3N_4 substrates, quartz substrates were also used for comparison purposes, so that the effects of dielectric coefficient of substrate on the transport process can be better understood.

Before spin coating, the substrates were squirt-washed by acetone and isopropyl alcohol (IPA) and dried with a nitrogen gun. The substrates were further dried by placing on a hot plate at ≈150 °C for 1 minute. The ceria precursor solution was then spin-coated onto the Si/Si_3N_4 substrate at 3000 rpm for 30 s, followed by pyrolysis at ≈400 °C on a hot plate surface for 1 min. The resulting thickness of NC thin films was characterized by profilometer. The spin coating and pyrolysis processes were repeated to achieve desired thickness. Finally, the samples were rapidly thermally annealed (rapid thermal processor, SSI Inc.) for 1 minute at 700 °C (ramping rate ≈100 °C/s) to crystalize the film and remove the eventual remaining organics.

2.1.1.2 Sputter Deposition

SD is a physical vapour deposition (PVD) method for thin film growth. When a high bias (>1 kV) is applied between the target and the substrate in a chamber filled with argon gas, electrons released from the target collide with argon atoms, ionizing them, leaving them positively charged. These atoms are then accelerated towards the target and strike it at high energy, releasing target material and depositing onto the substrate.

In this work, a Kurt J. Lesker PVD 75 sputterer with a 99.9% CeO_2 target (Kurt J. Lesker Co. Ltd.) was used for NC films deposition. NC films were deposited at 80 W in 5 × 10^{-3} Torr argon atmosphere. The growth rate was about 2.5 nm/min. The resulting thickness of NC thin films was characterized by profilometer.

2.1.1.3 Pulsed Laser Deposition

PLD is a PVD method where a high-power pulsed laser beam is focused inside a vacuum chamber to strike a target of the material that is to be deposited. This material is vaporized from the target in a plasma plume, depositing onto the substrate facing the target. By adjusting the substrate temperature, background gas and pressure, laser energy and pulse frequency, the film orientation, density and grain size can be controlled.

To prepare the NC target for PLD, 25 grams of CeO_2 (99.99% Reactor Grade, Sigma-Aldrich Inc.) was milled in a high density polyethylene bottle with 1 cm yttria-stabilized zirconia milling media and 20 mL of isopropanol (HPLC Grade, Fisher Scientific International, Inc.) for 24 hours. The powder was dried and heated to 800 °C for 12 hours. The powder was then collected and milled in a high-density polyethylene bottle with 3 mm yttria-stabilized zirconia milling media for 30 minutes. The powder was collected and pressed into a 1 ¼" disk. The resulting pellet was annealed at 1200 °C for 24 hours to form the final target.

A KrF excimer laser (Coherent Lambda Physik GmbH) with a wavelength of 248 nm and a pulse width of 25 ns was focused on the target with a spot size of about 2 mm^2. The PLD system was equipped with a reflection high-energy electron diffraction (RHEED) system for the *in-situ* diagnostic of the deposition process. The NC thin films were deposited at 500 °C and 700 °C substrate temperature under 0.1 Torr oxygen base pressure, and at 500 °C substrate temperature under high vacuum ($<10^{-6}$ Torr). Si/Si_3N_4 substrates with size 10×10×0.5 mm were used for PLD deposition. The target-to-substrate distance was 40 mm, and silver paste was used to provide thermal contact between the sample holder

and the deposition substrate. The laser energy density was about 1.5 J/cm^2 with a repetition rate of 10 Hz. The total deposition time was 5 min, and the estimated growth rate was about 0.3 nm/s.

2.1.2 Y-BZO Thin Films Deposition

In this thesis, PLD was used for Y-BZO thin film growth. 0%, 5%, 10%, 15% and 20% mole percent Y-BZO pellets were prepared by powder sintering. Ceramic targets were fabricated using standard solid state reaction processing. 20 gram batches of starting material were prepared by mixing stoichiometric amounts of $BaCO_3$ (99.95% Reaction Grade, Alfa Aesar), Y_2O_3 (99.9% Reaction Grade, Alfa Aesar), ZrO_2 (99% nanopowder, Alfa Aesar) in a high density polyethylene bottle with 1 cm yttria-stabilized zirconia milling media and 20 mL of isopropanol (HPLC Grade, Fisher Scientific International, Inc.) for 24 hours. The powder was dried and heated to 800 °C for 12 hours. The powder was collected and SpexMilled in a high density polyethylene bottle with 3 mm yttria-stabilized zirconia milling media for 30 minutes. The powder was further collected and pressed into a 1 ¼" disk using Duramax binder. The resulting pellet was annealed at 1550 °C for 24 hours to form the target used for the film growth.

Same as the PLD set-up used for NC thin film growth, an excimer laser (Lambda Physik GmbH, Germany) with a wavelength of 248 nm was used for Y-BZO deposition. RHEED system was used for the in-situ diagnostic of the deposition process. The target-to-substrate distance was 40 mm, and the oxygen partial pressure was 40 mTorr. The thermal contact between the sample holder and the deposition substrate was provided by silver paste. The laser energy density was about 1.5 J/cm^2 with a repetition rate of 10 Hz.

To prepare highly oriented Y-BZO films with limited defects, a good crystallographic matching between the film and substrate material is required. Different substrates were selected in this study. MgO (100) substrates (Princeton Scientific Corp.) were used to prepare grain-boundary-free epitaxial Y-BZO films, since the cubic structure of MgO (a=4.21 Å) is very close to Y-BZO (4.20-4.22 Å).[33] The epitaxial Y-BZO samples were deposited at 750 °C substrate temperature. It was found that lower the substrate temperature will result in less textured film, thus polycrystalline Y-BZO films were also prepared on MgO (100) for comparison, and the substrate temperature was set at 600 °C. The thickness of Y-BZO films ranged from 30 nm to 500 nm.

The effect of lattice non-stoichiometry on the ionic dynamics of Y-BZO is also investigated. To create non-stoichiometry, 20Y-BZO thin films were annealed in atmosphere at 1050 °C for 24 h in a tube furnace. To create strain on Y-BZO lattices, substrates with a slight mismatch were chosen. (100) oriented $(LaAlO_3)_{0.3}(Sr_2TaAlO_6)_{0.7}$ (LSAT, cubic perovskite structure, a=3.86 Å) and (110) oriented $NdGaO_3$ (NGO) orthorhombic perovskite structure (a=b=3.863 Å, c=3.854 Å in the pseudocubic cell) were used. These films provide a compressive strain between Y-BZO films and the substrate. For tensile strained Y-BZO, there is no commercial substrate available with a cubic structure where a is slightly greater than 4.21 Å. Considering that $BaCeO_3$ (BCO) is perovskite structure with a=4.5 Å, the BCO films is deposited as a buffer layer for Y-BZO, where ≈8% tensile strained Y-BZO substrate can be achieved. The obtained Y-BZO thin films were used for energy discovery platforms in tr-KPFM potential measurements as well as *in-situ* STEM characterization.

2.2 Structural Characterization of the Films – X-Ray Diffraction

X-ray diffraction (XRD) is a widely used, non-destructive technique that provides both crystal structure and chemical composition information. A monochromatic X-ray beam is incident on a crystal and scans at a range of incident angles, and the reflected beam forms diffraction pattern due to constructive interference only at some specific angles.

In θ-2θ scans, the diffracted beam intensity is collected at an angular position of twice the incident beam. As 2θ increases, the Bragg equation is satisfied at certain position, shown in Equation 23, where n is an integer, λ is the wavelength of the incident X-ray, a is the interplanar distance of the material, and θ is the incidence angle. At this condition, the detector reads high X-ray intensity, showing a peak at this 2θ angle in the diffraction pattern. The position of these peaks in the plot of the diffraction pattern represent the incidence angle corresponding to a specific family of atomic planes in the crystal, as determined by the Bragg equation. This provides information regarding the interplanar distance and thus the crystal structure of the material of interest (Figure 2-1).

$$n\lambda = 2a \sin\theta \tag{23}$$

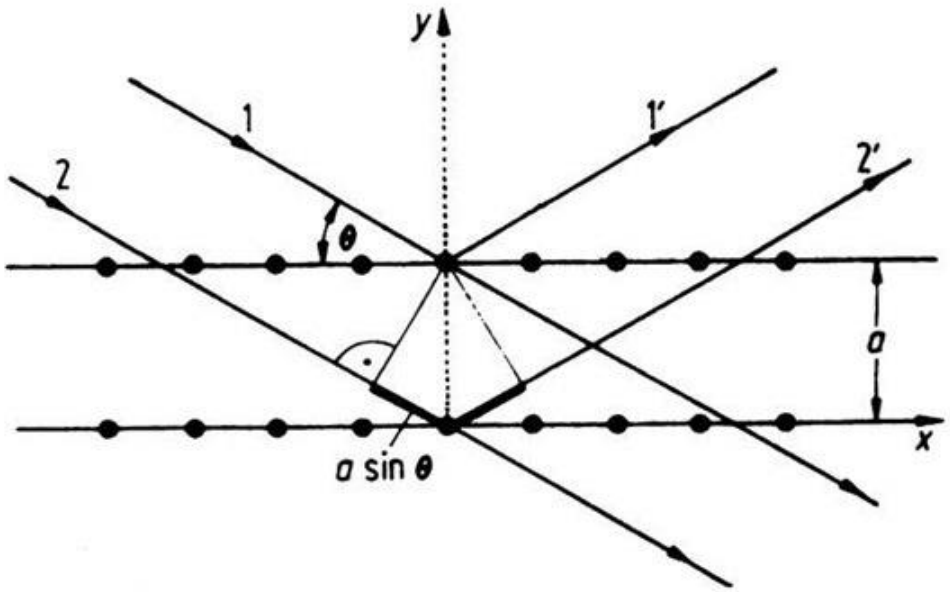

Figure 2-1 – Schematic of Bragg's law of diffraction in a crystal.

Rocking Curve, or Omega scan, is also performed in this study to detect perfection of crystals. In this measurement, the detector is set at the center of the expected Bragg angle and the sample is tilted (Ω is changed). A perfect crystal will produce a very sharp peak, observed only when the crystal is properly tilted so that the crystallographic direction is parallel to the diffraction vector. In reality, defects like mosaicity, dislocations, and curvature create disruptions in the perfect parallelism of the atomic planes, broadening the measured rocking curve.

A phi(φ)-scan provides information about the orientation of a specific set of diffraction planes in the material. In this measurement, the sample is rotated around the axis perpendicular to the sample plane while the detector is fixed at a curtain position. According to the symmetric property of the measured crystal, the diffraction peak of a certain plane will periodically appear when the sample is rotating.

These measurements were characterized by a Philips Xpert XRD (Cu Kα=1.5418 Å). The acquisition conditions were 45 kV and 40 mA. Scans were typically obtained with 2θ ranging from 20° to 70°, with a step size of 0.02°, and a scan rate of 1 s/step. The obtained diffraction patterns are compared with the Joint Committee on Powder Diffraction Standards (JSPDS) data, as shown in Table 2.1.

Table 2-1 – Powder diffraction file numbers used for XRD scan (from JCPDS).

Material	PDF card number
CeO_2	34-0394
$BaZrO_3$	6-0399
$BaCeO_3$	22-0074
MgO	4-0829
$NaGdO_3$	70-3810

The degree of crystallographic texturing of the films along a certain orientation of the films was characterized by the Lotgering factor, as detailed in CHAPTER 5. [147, 148]

2.3 Surface Topography and Thickness Characterization

2.3.1 Scanning Electron Microscopy

Scanning electron microscopy (SEM) is a type of electron microscopy that is widely used to detect the surface morphology of a sample by scanning it with a focused beam of electrons. The electrons interact with atoms in the sample, producing various signals that contain information about the sample's surface topography and composition. The resolution SEM can achieve can be better than 1 nanometer.

In this study, field emission SEM (Zeiss Merlin SEM and Ultra 60 Zeiss, Carl Zeiss Microscopy, LLC) was used for morphological characterization of sample surface and cross-section of NC thin films. SEM images were normally performed at an acceleration voltage of 3 kV with in-lens detection mode.

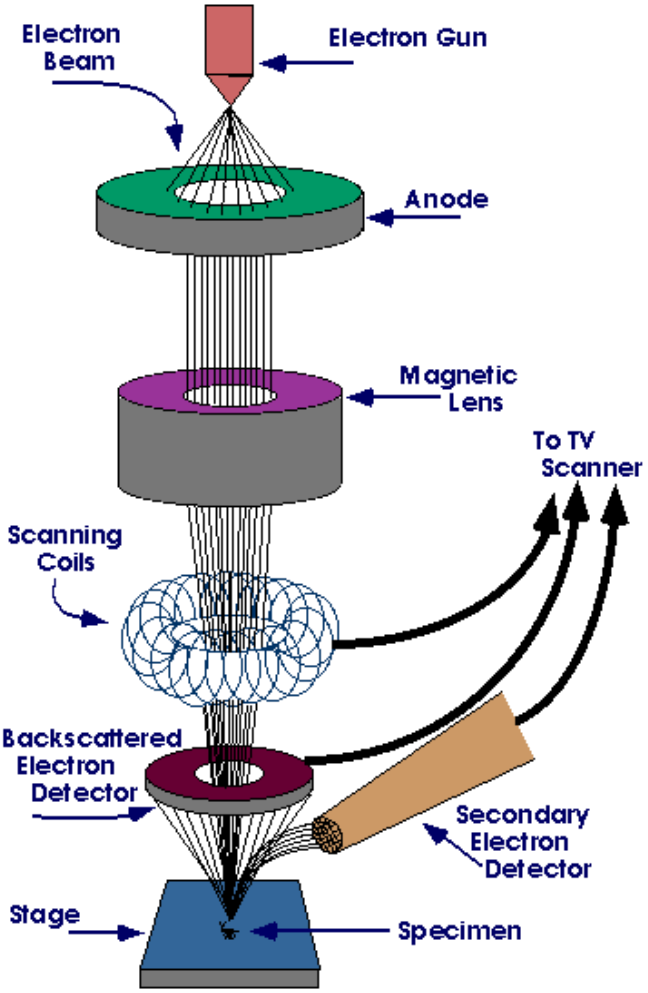

Figure 2-2 – Schematic of a scanning electron microscope.[149]

2.3.2 Atomic Force Microscopy

Atomic force microscopy (AFM) is a type of scanning probe microscopy (SPM) that can detect the surface topography by scanning the sample with a vibrating cantilever.

When the tip is brought close to the sample surface, the force that the sample imposes on it can be used to form an image of the three-dimensional shape of a sample surface with a sub-nanometer resolution.

In this study, an AFM (Bruker Inc.) was used for surface microstructure characterization. The standard tapping mode was used to examine the surface roughness of the films. Silicon cantilevers (Budget sensors, Co.; 300 kHz resonance frequency) were used.

2.3.3 Profilometer

Profilometer is a measuring instrument used to measure a surface's profile, where information of thickness and roughness can be obtained. In this work, the thickness of the NC films was characterized by a profilometer (P15 profilometer, KLA-Tencor Corp.).

2.3.4 Refractometry

Refractometry is a measurement technique to characterize the thickness and refractive index of transparent thin films. The intensity of reflected light is measured as a function of wavelength. The constructively interfere of the incoming light and the reflected waves will result in an optical maximum, while the destructively interfere will result in a minimum. Then the thickness (t) of the films can be determined by determining difference in the wavelength between the maxima or minima ($\Delta\lambda$):

$$t = \frac{\Delta\lambda}{2n} \tag{24}$$

where *n* is the real component of the refractive index and is assumed to be independent of the wavelength. In this work, the thickness of Si_3N_4 was determined by refractometry (NanoSpec 3000 film analyzer, Nanometrics Inc.).

2.4 STEM-EELS Characterization

2.4.1 Sample Preparation

2.4.1.1 Mechanical Preparation

Mechanical preparation is the most common method for STEM samples. For the thin films samples in this study, it usually takes 8-16 hours to prepare. The preparation procedure can be divided into four steps: cutting, polishing, mounting and ion milling.

1. Firstly, two pieces of samples of the same size (thickness = 0.5 mm) were sandwiched together using M-bond glue, with the film side facing each other. After placing on hot plate at 150 °C for 4 hours, the sample was then cut into smaller pieces (about 1 mm × 1 mm × 0.5 mm) using a diamond saw.
2. The sample was mounted onto a mounting plate using mounting wax, with the film plane perpendicular to the mounting plate. The plate was then mounted on Multiprep polishing system (Allied High Tech Inc.). Lapping paper with roughness of 6 μm, 3 μm and 1 μm was used sequentially to polish each side of the sample, until the final thickness of the sample decreases to about 20 μm, measured by a micrometer depth tool.

3. After polishing, the sample was glued on TEM copper ring using M-bond. Acetone, methanol and isopropanol (IPA) was used sequentially to remove the remaining wax and clean the sample.
4. The center thickness of the sample is further decreased using ion milling machine (Fischione Inc. Model 1010 Ion Mill), until a hole appears, at below -50 °C environment using liquid nitrogen. The films area that is close to the hole is usually around tens to hundreds of nanometers and can be used for STEM.

2.4.1.2 Focused Ion Beam

STEM samples were also made with focused ion beam (FIB). FIB has a similar set-up as SEM; however, while the SEM uses a focused beam of electrons for imaging, a FIB uses a focused beam of ions instead. FIB utilizes liquid metal ion sources, typically Gallium ions, due to its low surface free energy, low volatility and low melting temperature. Ga metal is placed in contact with a tungsten needle and heated gallium flows from the reservoir to the tip of the tungsten needle via the application of electric field between the needle and the opposite electrodes. The electric potential causes surface tension that forms the gallium into a cusp shaped tip called a Taylor cone. When a threshold voltage is reached, the Taylor cone releases a source of ions that travel down the ion column with a controlled acceleration voltage and beam current. When the Ga ions collide with the sample's surface, the moment is transferred from the incident ion to the sample. At high beam current, surface ions can be ejected, and can be applied for site specific sputtering or milling.

The STEM sample preparation with FIB has four steps: deposition, cut-out, transfer and thinning. It usually takes about 2-4 hours to prepare one sample. During deposition

process, a layer of conductive materials, such as carbon or platinum is deposited on top of the sample. Then the bulk sample is gradually cut-out by Ga ions from the bulk, forming a thin sample that is about 20 μm long (X), 1.5 μm thick (Y) and 6 μm deep (Z). During the transfer process, the sample is lift out from the original sample, and transferred to a copper pose of the sample holder. The sample is then further exposed in Ga ion to reduce the thickness.

2.4.2 Scanning Transmission Electron Microscopy

Scanning transmission electron microscopy (STEM) is a microscopy technique in which a beam of electrons is transmitted through ultra-thin specimen, interacting with the specimen and forming an image from the electron-specimen interaction. STEM is advantageous over other characterization techniques due to the unprecedented high spatial resolution, which enables the user to examine fine details of the material, including atoms and defects within sub-angstrom resolution. By using STEM and a high-angle STEM detector, it is possible to form atomic resolution images where the contrast is directly related to the atomic number (Z-contrast image), as shown in Figure 2-3.

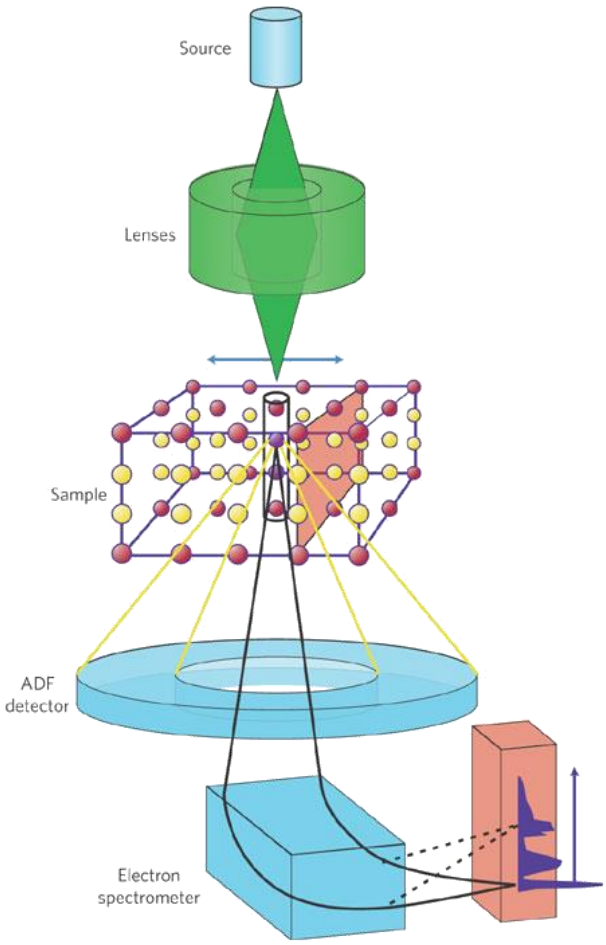

Figure 2-3 – Schematic of a scanning transmission electron microscopy.[150]

There are, however, several drawbacks of the STEM technique. The exceptional spatial resolution inevitably results in the field of view being relatively small, raising the possibility that the analyzed region may not be characteristic of the whole sample. In addition, ultra-high vacuum and room temperature is often required during imaging, which is contrary to the working environment of most of the materials investigated. To solve this challenge, environmental holder is developed. By introducing gas into the sample chamber with controllable pressure from room temperature up to ≈1000 °C, the interaction between the sample and the environment can be studied in real time.[151]

In this study, an aberration corrected Nion UltraSTEM 100 (operated at 100 kV) was used to obtain atomic resolution images of the Y-BZO specimens. High-angle annular dark field (HAADF) STEM images were acquired with an electron probe convergence semi-angle of 31 mrad and 86-200 mrad collection semi-angle. The STEM images were averaged from 10 fast frames acquired with a pixel dwell time of 4 μs and 512×512 frame size. The frame averaging process significantly reduces scan distortion and enhances signal-to-noise ratio. The locations of atomic columns were identified using normalized cross-correlation and fitted using a 2D Gaussian distribution, which were used for lattice distortion analysis.

2.4.3 Electron Energy Loss Spectroscopy

Electron energy loss spectroscopy (EELS) is based on the same equipment of STEM, with the addition of an electron spectrometer. A material is exposed to a beam of electrons with a known, narrow range of kinetic energies. When passing through the material, electrons will undergo inelastic scattering, causing energy loss and deviation of the traveling path. With EELS, element information and even chemical bonding information of the material is possible in atomic resolution. In this study, Nion UltraSTEM 100 (operated at 100 kV) was used to obtain chemical composition mapping of the Y-BZO specimens via EELS.

2.5 Atom Probe Tomography

Atom probe tomography (APT) is a material analysis technique that has capabilities for three-dimensional imaging and chemical composition mapping at the sub-nanometer length scale.[152-155] The sample is prepared in the form of a very sharp tip using FIB. The

cooled tip is biased at high DC voltage, typically 3-15 kV. This induces high electric field on the tip of the sample, just below the point of atom evaporation. Under pulsed laser, one or more atoms are evaporated from the surface by field effect, and projected onto a position sensitive detector with a high detection efficiency. The detector is able to measure the position (x and y position) and m/q ratio (mass over charge ratio) of each ion by measuring the time between the laser pulse and the arrival on the detector. The former can provide information to reconstruct the original position of each atom on the tip, and the latter determines the chemical composition of this atom. As the atoms are progressively removed from the tip, the 3D compositional image of the material can be reconstructed at the atomic scale.

An FEI Nova 200 dual-beam focused ion beam (FIB) instrument was used to perform lift-outs and annular milling to fabricate the needle-shaped APT specimens containing the Y-BZO layer. A wedge lift-out geometry was used to mount multiple samples on a Si microchip coupon to enable the fabrication of multiple needles from one wedge lift-out. APT was performed with a CAMECA instruments LEAP 4000X HR (≈36% detection efficiency) and a 5000 XS (≈80% detection efficiency) local electrode atom probe. Samples were run at a base temperature of 40 K, applying laser at 355 nm wavelength, 10 ps pulse time and 50 pJ power at a repetition rate of 200 kHz. The datasets were reconstructed and analyzed using the IVAS 3.6.12 software (CAMECA Instruments). The sample preparation and APT measurements were done in ORNL, by Dr. Wei Guo. The

In this study, the normalized χ-square statistics was used to track the changes in the degree of solute segregation from APT:

$$\mu = \sqrt{\frac{\chi^2}{N + \chi^2}} \tag{25}$$

Where N is 50, which is the number of groups that the whole data is partitioned into; χ^2 is the deviation of an experimentally measured distribution from binominal distribution; and the calculated μ ranges from 0 to 1, with 0 to be a random distribution and 1 to be a complete association in the occurrence of the solute atoms.

2.6 Ionic Transport Characterization

2.6.1 MEMS Fabrication of Energy Discovery Platforms

Lateral Cr/Pt electrodes (20 nm/80 nm thick) were created on or underneath the ceria layer by evaporation and patterned by a lift-off method, for application of the external voltage. The electrodes were 10 μm wide with an inter-electrode distance ranging from 50 to 70 μm. Each die was glued to a chip holder using epoxy and the appropriate ground and bias electrodes were wire-bonded to the chip-level copper boards.

The ionic dynamics affect materials in a wide range of length scales. As shown in Figure 2-4. To fully understand the functionalities of the devices at macroscopic level, it is crucial to uncover the role of microstructure, grains, TPBs, and defects and dopant structures, from micrometer down to sub-nanometer scale. To achieve this, there are a number of characterization techniques available, such as electrochemical impedance spectroscopy, scanning probe microscopy and micro-Raman spectroscopy; however, each of them has its own strengths and drawbacks, and is only optimized at a specific range of

length scale. The thorough study of structure-property relationship necessities the integration of multiple techniques and a smooth transition between each other.

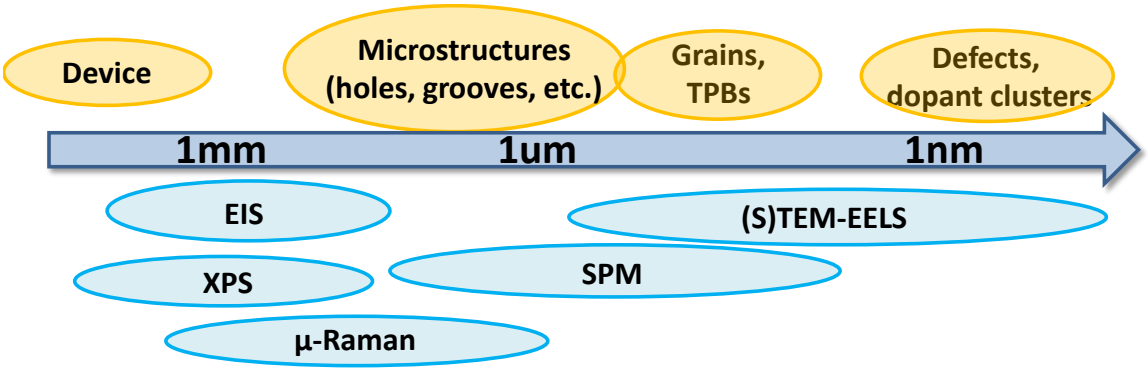

Figure 2-4 – The range of length scales of materials and characterization techniques.

In order to overcome this challenge, energy discovery platforms – a synergy of microfabricated devices and in-situ microscopy and spectroscopy techniques – are developed as a method for local probing of electrochemical and transport phenomena.[156] A typical microfabricated device for tr-KPFM characterization is shown in Figure 2-5. Through photolithography techniques, thin films are deposited on the substrate with parallel electrodes for external bias. Thanks to the platform design flexibility offered by the microfabrication techniques, the structure can be engineered by tuning materials' composition and geometry to establish a broad variety of driving electrostatic fields. At the same time, surfaces and interfaces can be fabricated to introduce open or covered TPB regions or surface coatings (comparison between Figure 2-5a and b), allowing for chemical and physical control of reaction space. The atmosphere and environmental conditions such as temperature and humidity can also be adjusted to create controllable electrochemical reaction parameters.

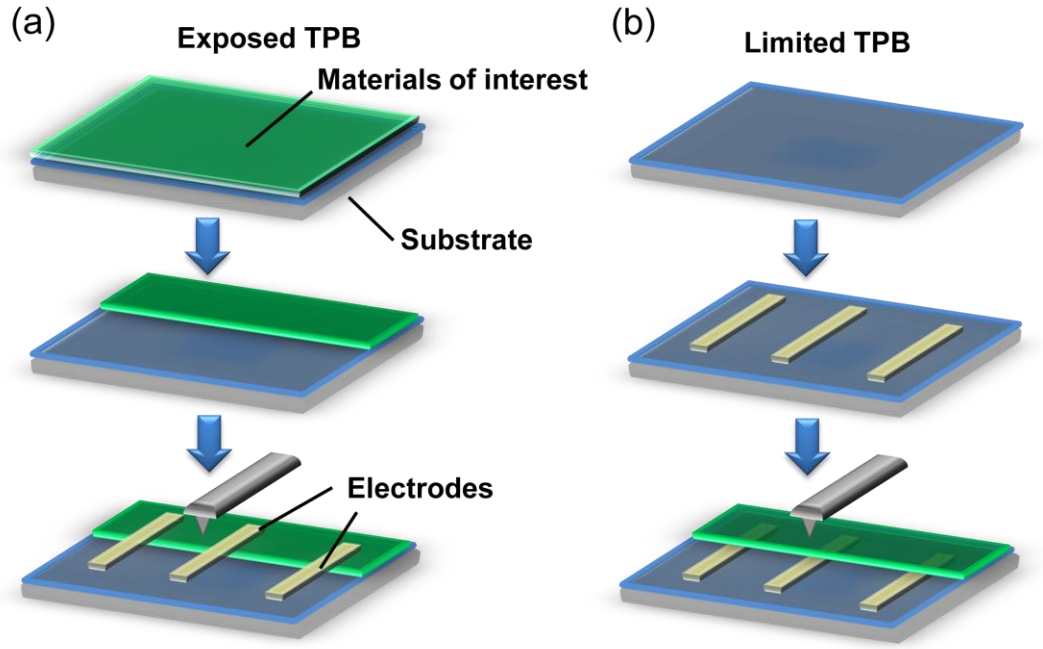

Figure 2-5 – Preparation procedure of the lateral devices with (a) exposed TPBs and (b) limited TPBs.

The same devices can be readily used for other techniques such as EIS and micro-Raman spectroscopy. In addition, energy discovery platforms offer more characterization opportunities by extending characterization methods to other SPM techniques. Scanning impedance microscopy (SIM) and non-linear SIM can be used to explore the transport phenomena in the 0.1 kHz – 1 MHz range. Piezoresponse Force Microscopy (PFM) can be used to characterize polarization properties and domain structures in ferroelectric materials. These are beyond the scope of this thesis. The application of energy discovery platforms can also be extended to environmental (S)TEM techniques. A free-standing membrane can be fabricated by back-etching of silicon substrate, creating a window for in-situ observation

under (S)TEM. If achieved, this will fill the long-existing gap between SPM characterization (sub-micron resolution) and (S)TEM imaging (sub-nanometer resolution).

In sum, the special advantages of energy discovery platforms are presented as follows:

1) Easy fabrication;
2) Flexible and designable device configuration and microstructure;
3) Controllable external stimuli (T, RH, atmosphere and bias);
4) Availability for in-situ/in-operando characterizations;
5) Potentially compatible with many techniques.

2.6.2 Time-Resolved Kelvin Probe Force Microscopy

Time-resolved Kelvin probe force microscopy (Tr-KPFM) one of the main characterization technique for the ionic dynamics study in this work. KPFM is a non-contact scanning probe microscopy (SPM) based technique providing the capability of imaging the local surface potential of a sample with sub-micron spatial resolution. Tr-KFPM extends the application of KPFM by allowing the acquisition of surface potential variation over a period of time (2 s to 100 s in this work), with a 10 ms temporal resolution.[157, 158] The schematic and principle of the tr-KPFM technique is illustrated in Figure 2-6. The measurement is carried out in a conventional AFM in dual pass mode. The cantilever is coated with Pt, with free oscillation frequency to be ω_0. During measurement, a waveform voltage is applied to the tip:

$$V_{tip} = V_{dc} + V_{ac}\cos(\omega t) \tag{26}$$

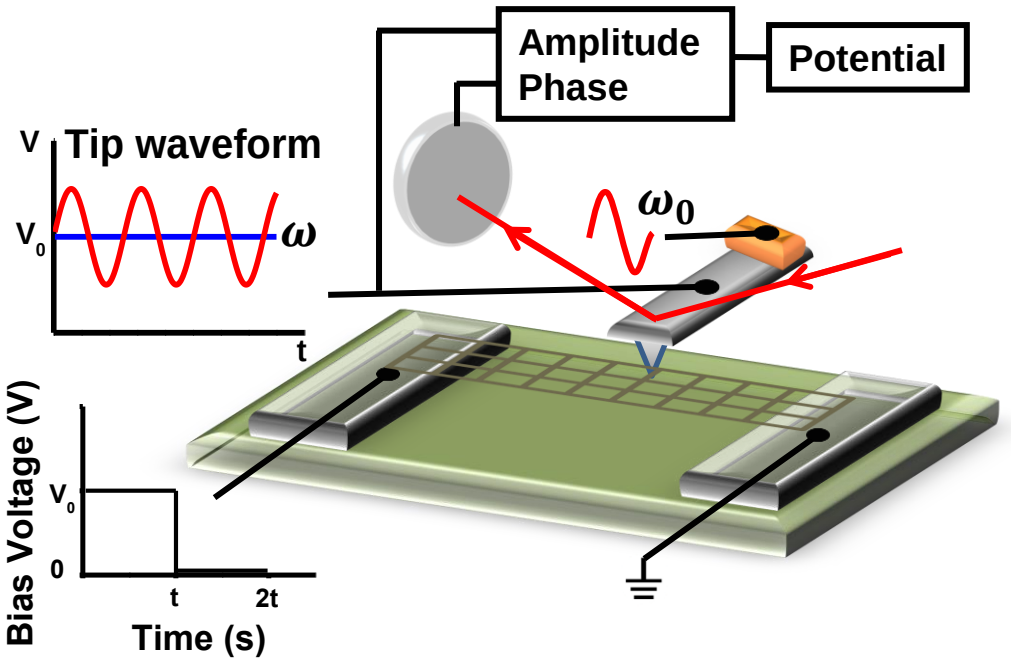

Figure 2-6 – Schematics of the tr-KPFM technique used in this study.

The oscillation frequency ω is chosen to be much lower than ω_0 to avoid cross-talk. Considering the tip-sample system as a capacitor, the electrostatic force between the tip and the surface is given by:

$$F_{el} = -\frac{1}{2}C_z'\left(V_{tip} - V_s\right)^2 \tag{27}$$

where C_z' is the capacitance gradient of the tip-sample system and the V_s is surface potential of the sample. The first harmonic of Equation 27 is expressed as:

$$F_{\omega_{ac}} = -C_z'(V_{dc} - V_s)V_{ac}\cos(\omega t) \tag{28}$$

When the cantilever is held at a fixed distance (z) above the surface, a change in the surface potential is reflected in the variation in deflection signal, which is detected by the lock-in amplifier as the amplitude and the phase of the signal:

$$\mathrm{A}(\omega) = \frac{F_{c1\omega}}{m\sqrt{(\omega^2 - \omega_0^2)^2 + \omega^2\gamma^2}} \tag{29}$$

$$\tan(\theta) = \frac{\omega\gamma}{\omega^2 - \omega_0^2} \tag{30}$$

Here, m is the effective mass of the cantilever, ω_0 is its free mechanical oscillation frequency, and γ is the damping coefficient. The surface potential can then be derived from the amplitude and phase of the signal:

$$V_s = V_0 - \frac{1}{f_{1\omega} \times C_z'|_{z_0} \times V_{ac}} \times A = V_0 - K \cdot Asin(\theta) \tag{31}$$

where K is the calibration coefficient and $f_{1\omega}$ is the transference function of the cantilever for the first harmonic. The obtained surface potential, however, is different from the actual surface potential in vacuum, and the difference is given by

$$V_s = V_{abs} - \frac{\Delta\chi}{e} \tag{32}$$

where V_{abs} is the true surface potential, e is the elementary charge and $\Delta\chi$ is the work function difference between the tip coating and the sample surface. As the difference is usually smaller than 1 eV, this is not taken into account in the proposed research.

In a typical tr-KPFM measurement, time- and space-resolved surface potential data of sample surface are recorded, as the tip scans over a spatially defined grid points. At each point of the grid, a two-step low-frequency probing voltage waveform is applied to the lateral electrodes. During step 1, a DC voltage, V_p, is applied between the electrodes for a period of time (t). In this stage, which is referred to bias-on, or polarization stage, field-induced charge injection and transport is expected to be activated, causing a continuous potential variation. During step 2 (bias-off, or relaxation stage), both electrodes are grounded to allow the surface potential to relax.

While direct impedance measurements could be difficult in micro- or nano-sized devices at low temperatures due to large resistance, characterization of variation in the surface potential provides an alternative way of studying ionic dynamics, and can be related to the variation of local charge concentration and distribution. Based on its outstanding spatial resolution, this technique overcomes the limitations of traditional macroscopic characterization methods. And with respect to temporal resolution, the slow dynamics of ionic processes are comparable with the time scale of SPM techniques, and therefore the use of such SPM techniques should prove a great tool for the electrochemical kinetics studies.

In this work, the local electrochemical and transport phenomena were studied by tr-KPFM under the externally applied voltage. The measure time (t) for polarization and

relaxation stage ranges from 2 s to 100 s. The surface potential evolution was recorded at each pixel of a rectangular grid (mostly 30×3), which was overlaid on the NC surface and spanned the distance between the electrodes. The surface potential was averaged for each of the measurements performed on the pixels of the grid equidistant from the biased electrode. The characterization was performed in a temperature range from 25 °C to 200 °C, with input relative humidity ranging from 0% to 90% (as measured at 25 °C) using a gas cell.

2.6.3 Electrochemical Impedance Spectroscopy

EIS is one of the most common characterization methods for electrochemical properties of materials. Different from direct current measurements, EIS has the ability to distinguish different responses of the total conduction behavior, because each electrochemical process typically has a unique time constant that can be resolved in the frequency domain.

When performing EIS measurements, a small alternating voltage, $v(t) = V_0 sin(wt)$ is applied on two electrodes connecting to the samples to be investigated. The responding current, $i(t) = I_0 sin(wt+\theta)$ is obtained. The phase shift and the amplitude of the resulting current are measured as a function of frequency, ranging from mili-Hz to mega-Hz. The complex impedance, Z, is calculated by taking the ratio of the voltage and current in the frequency domain:

$$Z(j,\omega) = \frac{V_0 e^{j\omega t}}{I_0 e^{j(\omega t+\theta)}} = Z_0 e^{-j\theta} \tag{33}$$

The complex impedance is usually shown in a Nyquist plot, where the real part of the impedance is presented in *x* axis and the imaginary part is presented in *y* axis. A typical Nyquist plotting from EIS measurements shows several arcs, representing different electrochemical processes. Equivalent circuits can be modelled corresponding to the Nyquist plot.

EIS is advantageous in that it is non-destructive, and can allow time dependent characterization for ongoing electrochemical processes. For example, when EIS measurement is applied to electrochemical devices such as fuel cells, a series of impedance values are obtained as a function of alternating current frequency. The modeling procedure uses electrical circuits built from components such as resistors and capacitors to represent the electrochemical behavior observed of the material. The quantified value of each component can then be used to analyze conduction mechanisms and pathways within the materials. This technique is useful for studying electrochemical processes such as ionic transport in electrolytes, [31, 33, 36] anodic behaviors of metals,[159] corrosion,[160, 161] and many other complex electrochemical phenomena. In addition to the complex impedance plot and the quantified impedance value, the EIS also provides further physical parameters such as modulus and dielectric constant. The comparison of these factors allows easier interpretation of the microscopic processes responsible for the local relaxation/long range conduction as well as the role of pores and/or grain boundaries.[162]

On the other hand, EIS does not allow an unambiguous resolution of the individual components, considering that the equivalent circuit is not unique, especially for complex systems. In addition, EIS is a macroscopic method, and individual elements cannot be easily resolved in space below the 10-50 μm limit. Moreover, as resistance is proportional

to the length to area ratio (l/A) and capacitance is proportional to A/l, the scaling down of electrochemical systems necessarily leads to increased resistance and reduced capacitances, which drastically limits the accuracy and accessible frequency range of EIS under such conditions.

2.7 Finite Element Method

Finite element method (FEM) is a numerical approach to obtain approximate solutions of equations for complex physical or mechanical phenomena. For most of these problems, there are a number of equations describing them, including partial differential equations. For most of the time, obtaining the exact solution is impossible. Then effort is needed to find a solution that approximates the exact solution. FEM subdivides a large problem to smaller and simpler ones that are called finite elements. The simple equations that model these finite elements are then assembled into a larger system of equations that models the entire problem. Through iteration of the calculations, the solution to the problem becomes closer to the reality by minimizing an associated error function. In FEM, dividing a big problem into smaller parts provides the following advantages: it accurately represents the whole complex geometry; and it also makes complex calculation much simpler and less time-consuming.

In this work, FEM was performed using COMSOL Multiphysics 4.4. The transport parameters were exported from COMSOL and was further analyzed in COMSOL LiveLink for MATLAB 4.4. The physical processes such as electrochemical reactions and ionic transport were modeled in FEM, and the parameters governing each process were obtained

through fitting with the experimental data. Details of how FEM were performed is introduced in CHAPTER 4.

2.8 Density Functional Theory

Density functional theory (DFT) is a computational quantum mechanical modelling method that computes the electronic structure of matter.[163, 164] Its applicability ranges from atoms, molecules and solids to classical fluids.[165, 166]

In this study, the DFT calculations corresponding to the defect formation energies and defect migration energies were performed employing Vienna Ab initio Simulation Package (VASP) with the generalized gradient approximation (GGA) according to Perdew, Burke, and Ernzerhof and the projector augmented-wave method.[167, 168] All the calculations on a 3×3×3 super cell encompassing 135 atoms. A Γ point centered 2×2×2 k-point mesh was used for Brillouin zone integration and a plane wave energy cut off of 400 eV was used in all calculations. The lattice constant was chosen to represent the experimental value (4.197 Å). The structural relaxations were performed to relax the internal coordinates without any change to the volume until the residual force of each atom was less than 0.01 eV/Å. The DFT calculation in this study was performed in ORNL, by Dr. Janakiraman Balachandran

CHAPTER 3. IONIC DYNAMICS OF NC – THE EFFECT OF EXTERNAL CONDITIONS

This chapter focuses on the analysis of electrochemical reactions and transport phenomena taking place on the surface of NC. The role of external conditions such as temperature, humidity, interface and atmosphere on the ionic dynamics is also discussed.

3.1 Materials and Experimental Set-Up

In this chapter, most of the measurements were done on NC thin films prepared by CSD on Si/Si_3N_4 substrates (detailed in CHAPTER 2), unless otherwise stated in the text. The electrodes were deposited on top of the NC film, creating exposed TPB structures. A typical X-ray diffraction pattern of the NC film deposited by CSD is shown in Figure 3-1, which confirms its good crystallinity by peak comparison to the literature data (PDF card number: 34-0394). Figure 3-2 shows the scanning electron microscope (SEM) image of the as-prepared NC film. Nano-grooves, which are about 50 – 100 nm long and ≈10 nm wide, are observed on the surface.

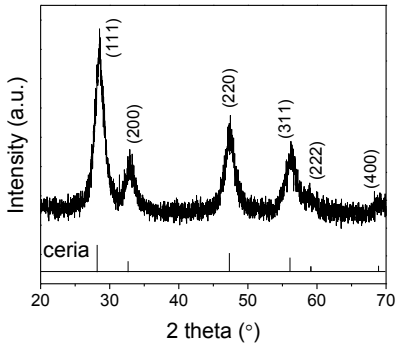

Figure 3-1 – X-ray diffraction pattern of the as-prepared ceria thin film.

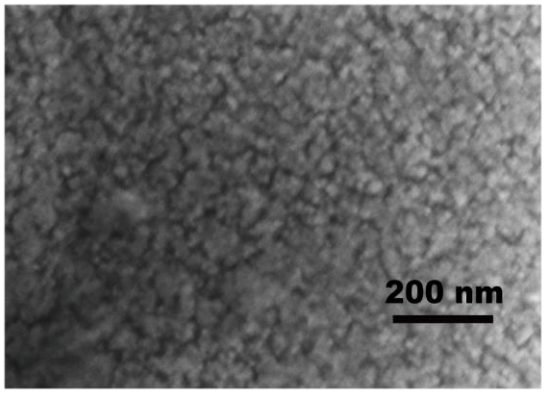

Figure 3-2 – Scanning electron microscopy image of the as-prepared ceria thin film.

Figure 3-3 shows a representative surface potential mapping as a function of distance and time obtained by tr-KPFM. The measurement was done at 25 °C and 80% RH, and the external applied bias during polarization stage was 30 V. The measure time for polarization and relaxation stage was 10 s each. The surface potential evolution was recorded at each pixel of a rectangular 100×12 grid, which was overlaid on the NC surface spanning the distance between the electrodes. The same data was separately presented in Figure 3-4a and b for polarization and relaxation stages, respectively. The local potential variation over time is a result of redistribution and transport of charge carriers along the surface. The potential profile at the initial moment (darkest blue curve) is assumed to represent the original equilibrium state in the absence of any electrochemical reactions or charge carrier transport. Biasing of the electrodes may initiate electrochemical processes, and migration of charge carriers in response to the applied electric field and concentration gradients. The arrow in Figure 3-4a shows that the surface potential profile gradually evolves to higher values (dark blue to light blue curve), which indicates the accumulation of positive charges in proximity to the biased electrode. Meanwhile, the surface potential slightly decreases in proximity to the ground electrode, indicating a weak accumulation of

negative charges at this region. When bias is turned off (green to red curve), both electrodes are grounded to allow the accumulated charge carriers to redistribute. During this time period, no new charge carriers are generated and the potential profiles tend to level out with time, as shown in the arrow in Figure 3-4b.

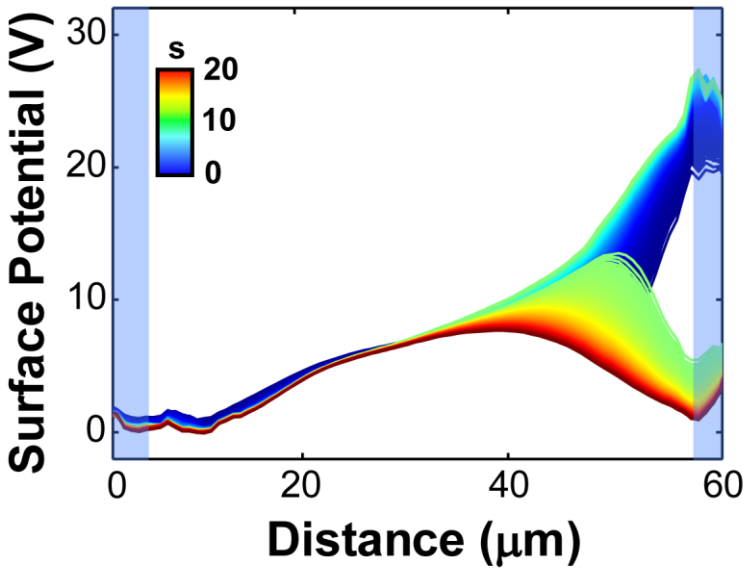

Figure 3-3 – Representative surface potential mapping as a function of distance and time measured at 25 °C and 80% RH. The two shaded areas on the left and right side of the graphs represent the areas overlapping with the grounded and biased electrode, respectively.

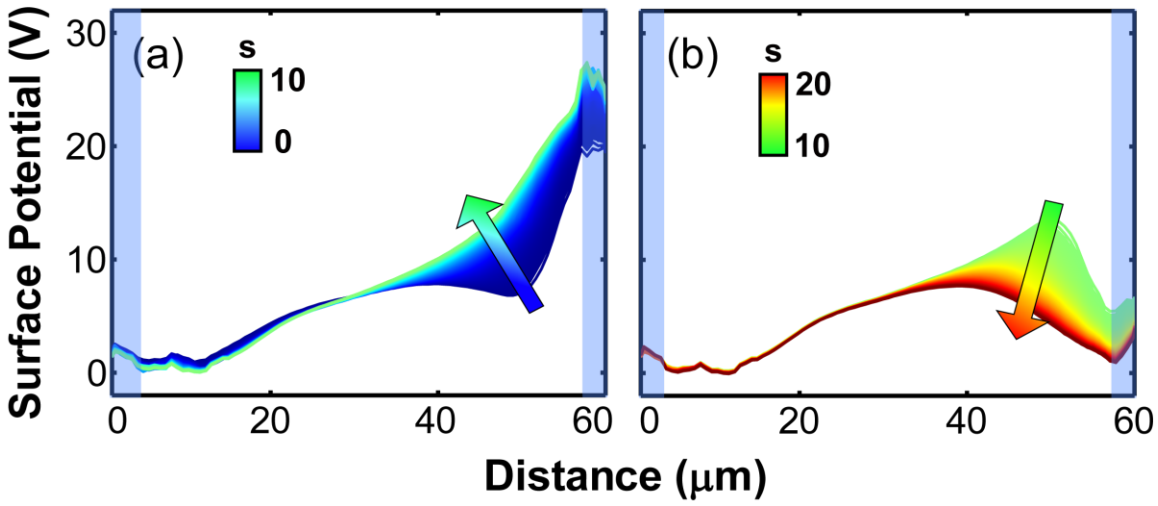

Figure 3-4 – (a) polarization stage (initial 0 to 10 s) and (b) relaxation stage (subsequent 10 to 20 s) of the surface potential mapping in Figure 3-3. The arrows indicate the surface potential increase and decrease with time during polarization and relaxation stage, respectively. The blue shaded areas correspond to the position of electrodes.

Figure 3-5 presents the surface potential evolution over time as a function of distance, which is obtained from the same tr-KPFM measurements and contains the same information as presented in Figure 3-3. However, it is clearly seen that in proximity to the biased electrode where the surface potential change is the strongest (in this case d>40 μm), the surface potential has a decreased slope over time, and reaches a saturation at the end of each stage. Therefore, the surface potential variation at each point of NC can be quantified by an exponential model:[169, 170]

$$\Phi = A + B \cdot e^{-t/\tau} \tag{34}$$

where Φ is the surface potential, A is the offset parameter, B is the pre-exponential factor, t is time, and τ is the mean lifetime, inversely proportional to the diffusion coefficient of

charges. Thus, a faster change in surface potential is an index of a reduction of τ, i.e. an enhancement of charge diffusivity.

τ is an important factor to calculate the activation energy for ion transport. To understand the accuracy and reliability of tr-KPFM measurement, the exponential fitting is obtained on each grid point. The standard deviation of τ was obtained as a function of distance, as shown in Figure 3-6. At distance between 45-55 μm, where the strongest electrochemical reaction takes place, the error of τ is lower than 5%. Therefore the data obtained from this region are collected for fitting in this study. We note that, if we partly choose a part of data from this 100x12 grid points, say 30x3, the value of activation energy and fitting parameters are almost not affected. Additionally, 120x10 grid measurment is time consuming: for each environment condition, it will typically take a day to measure the full sample, with possible resulting variations of the surface at higher temperature and humidity. Therefore, data from 30x3 grid is representative for data with higher special resolution, and is used for most of the following studies.

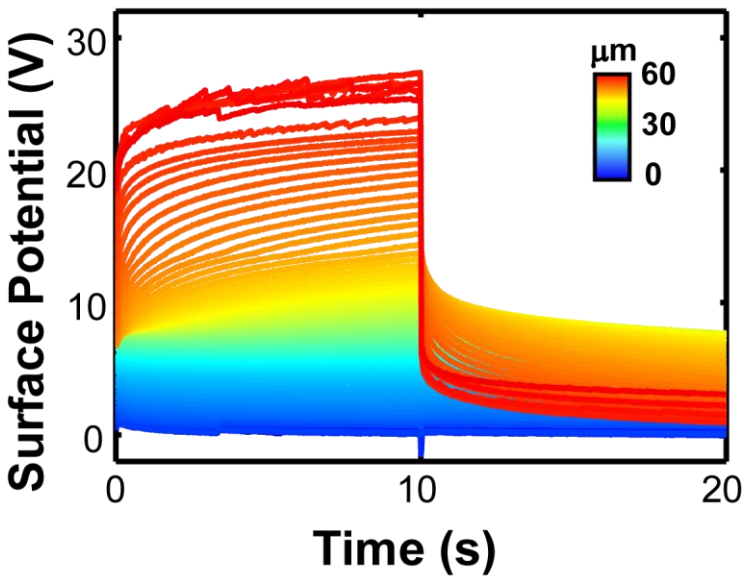

Figure 3-5 – Surface potential evolution over time as a function of distance measured at 25 °C and 80% RH.

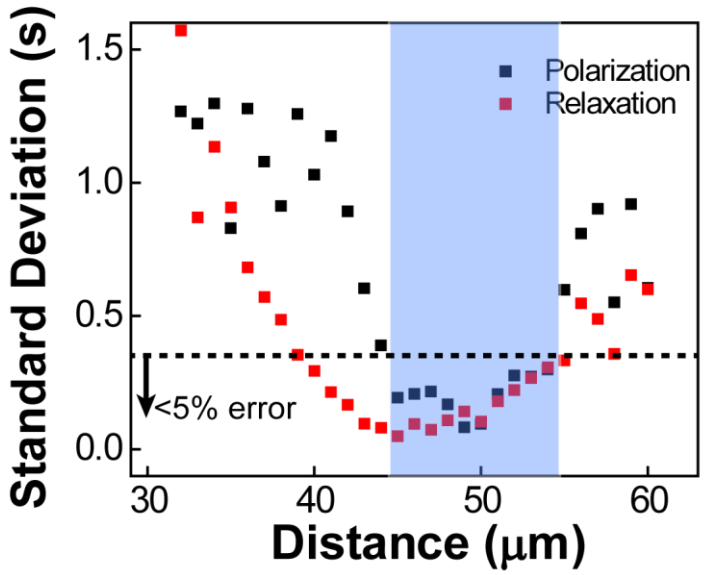

Figure 3-6 – Standard deviation of τ as a function of distance corresponding to Figure 3-5.

With these basic understandings of tr-KPFM measurements, the following sections report ionic dynamics study at controlled external conditions, with temperature ranging from 25 °C to 135 °C, RH from 0% to 90% (as measured at 25 °C), external bias from 5 V to 30 V.

3.2 Effects of Humidity, Temperature and Bias

The surface potential evolution is strongly dependent on the ambient humidity, as reported in Figure 3-7. While recording surface potential via tr-KPFM, the inter-electrode current was also recorded at each polarization and relaxation measurement (Figure 3-8), that is, 90 times in total for each sample (3×30 spatial grad = 90 individual measurements). The color scale indicates the sequence of data capture: from measurements of surface potential close to the grounded electrode (yellow lines), to those recorded close to the biased electrode (red lines).

At 0% RH and 25 °C (Figure 3-7a), the surface potential does not show any noticeable potential variation. The inter-electrode current (Figure 3-8a) is not detectable over the space and time domain probed, indicating that the electrochemical reactivity and charge transport is limited at low temperature and low humidity. However, with increase of RH to 40% (Figure 3-7b) and 90% (Figure 3-7c), stronger polarization and relaxation processes are observed, and the strong potential variations extend to almost the whole inter-electrode NC surface at 90%. During the relaxation stage the potential profile levels down, and finally forms an arched curve with a local maximum of ≈8 V, indicating the presence of residual positive charge carriers on the NC surface. The inter-electrode current is independent of the AFM tip position, but shows a weak memory effect at 90% RH

(previous measurements influence the subsequent ones), as shown in Figure 3-8c. In addition, the current slightly decreases with time for each measurement. Such phenomenon is resulted from the accumulation of positive charges in proximity to the electrode over time, which will result in a slightly reduction of the charge generation rate and thus a decreasing current. The inter-electrode current is about 0.2 nA during polarization stage, showing a higher conduction at high humidity atmosphere. This may indicate that either more conduction species are generated or additional conduction pathways are created (e.g. thicker water layer), facilitating the overall ionic transport.

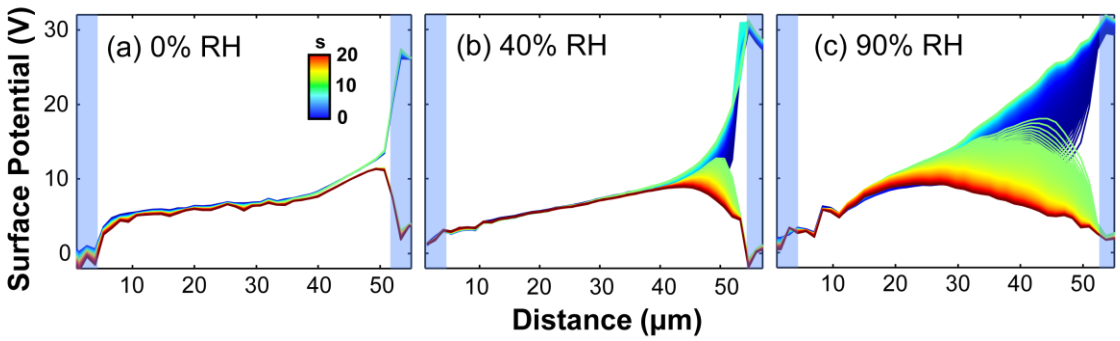

Figure 3-7 – Humidity dependence of surface potential vs. time and position measured at 25 °C and (a) 0% RH; (b) 40% RH and (c) 90% RH. The blue shaded areas correspond to the position of electrodes.

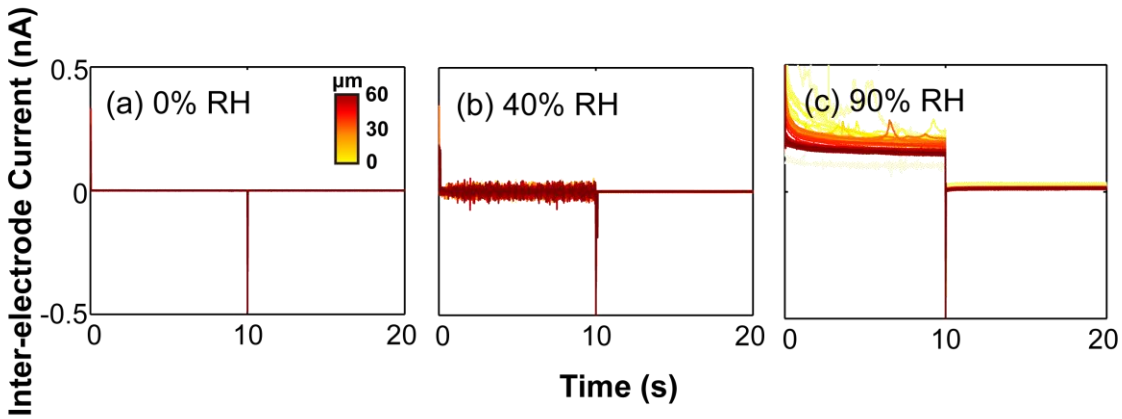

Figure 3-8 – Inter-electrode current evolution over time as a function of distance measured at 25 °C and (a) 0% RH; (b) 40% RH and (c) 90% RH.

Figure 3-9 shows the surface potential evolution as a function of temperature in absence of humidity. As temperature increases, the surface potential variation becomes much stronger. It is worth noting that the remnant charge at the end of the relaxation stage (20 s) decreases from about 8 V at 75 °C to almost 0 V at 125 °C, consistent with faster charge dissipation at higher temperatures. The inter-electrode current is almost zero for all cases (Figure 3-10), suggesting a substantially limited pathway for charge transport at elevated temperatures.

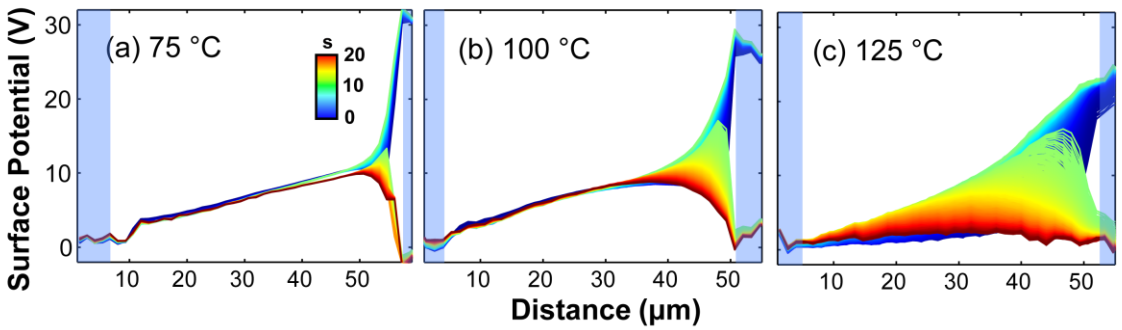

Figure 3-9 – Temperature dependence of surface potential vs. time and position measured at 0% RH and (a) 75°C; (b) 100°C and (c) 125°C. The blue shaded areas correspond to the position of electrodes.

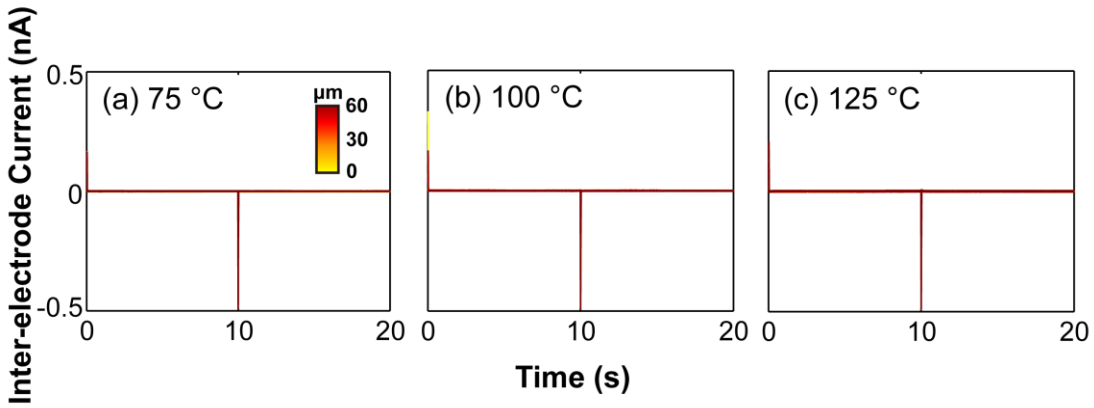

Figure 3-10 – Inter-electrode current evolution over time as a function of distance measured at 0% RH and (a) 75 °C; (b) 100 °C and (c) 125 °C.

Figure 3-11 shows the surface potential mappings as a function of applied bias during polarization stage. All measurements were done at 25 °C and 60% RH. It is found that when lower bias is applied to the electrode, especially 5 V, the surface potential signal is more unstable due to a relatively larger error, and there is a lot more noise, probably caused by unexpected vibrations due to air flow, or a sudden jump on the rough surface. When higher voltage is applied to the electrode, the signal becomes less noisy. So 30 V is applied to the biased electrode during tr-KPFM measurements for the rest of the study.

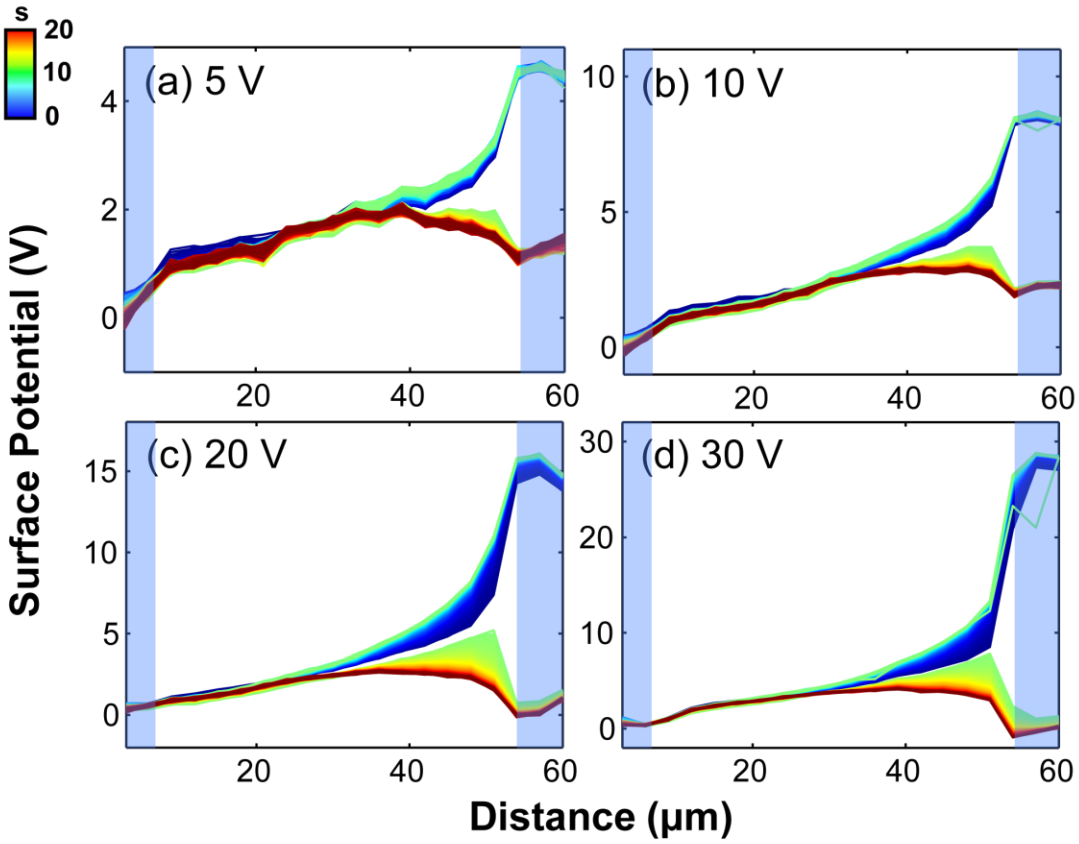

Figure 3-11 – Bias dependence of surface potential vs. time and position measured at (a) 5 V; (b) 10 V; (c) 20 V and (d) 30 V. The measurements were performed at 25 °C and 60% RH. The blue shaded areas correspond to the position of electrodes.

3.3 Ionic Dynamics Taking Place on NC

3.3.1 Transport Species

The observed surface potential change over time should be caused by migration and redistribution of charge carriers under electric field. According to the previous section, the surface potential variation is largely dependent on temperature and humidity, suggesting a crucial role of the surface water in the ionic dynamics. In Figure 3-7a, without atmospheric humidity, the water layer on NC surface is limited. The potential does not

show any obvious change with time, suggesting that any charge present on NC surface is neither accumulating nor moving, i.e. the charge is static. Whereas the observed surface potential variation is very different at higher RH (Figure 3-7b and c). This suggests that the addition of humidity in atmosphere and thus the electrochemical reactions on surface water layer would be the main reason for the observed ionic dynamics rather than the movement of other charges in the underlying NC surface or substrates.

It has been previously shown that a significant amount of water is adsorbed on the surface of ceria and intergranular area even under dry atmosphere at above 300 °C,[171] and the amount of water layer is sensitive to the environmental conditions. Therefore, protons and hydroxyl groups, generated from water are assumed to be the most probable charge carriers within the temperature range probed in this work. This assumption will be further confirmed in the following study.

Electrons are another charge species that may contribute to the surface potential mapping. However, the electronic response time is determined by the RC constant of the NC lateral device and circuitry. The resistivity was estimated from the interelectrode current data as a function of time and the capacitance was measured by impedance spectroscopy. The RC constant of the NC lateral device is estimated to be on the order of 100s (resistance is $\approx 10^{14}$ Ω, and capacitance is $\approx 10^{-12}$ F), indicating that even electrons did transport along the surface, they respond rather slowly to the electrical field and still are not be able to detected by the current settings.

It is reported that surface defects such as oxygen vacancies are active spots for electrochemical reactions, and therefore may also contribute to the charge transport of NC.

However, direct oxygen vacancy migration is not likely to be activated due to the higher energy barrier for oxygen diffusion through lattice. In fact, oxygen ion conductivity is significant only at temperatures as high as 500 °C for doped ceria.[172] The surface oxygen vacancies, on the other hand, may facilitate the transport of protons and hydroxyl groups, which will be illustrated in the following section.

Therefore, possible electrochemical processes that facilitate conduction and cause the surface potential variation can be identified.

3.3.2 Electrochemical Reactions

3.3.2.1 Charge Generation at TPBs

Water molecules on the NC surface can split into protons, electrons and oxygen molecules under the electric field (Equation 35). The electrochemical potential for water splitting is E_{red}° =1.23V.[12] Since this reaction includes ions, gas and electrons, it is thus expected to take place in the proximity of TPBs, where the surface potential is above 20V. The generated protons are continuously injected into the NC and can migrate towards the grounded electrode. Meanwhile, the compensating electrons are transported through the electrodes.

$$2H_2O(l) \rightleftarrows 4H^+(aq) + O_2 + 4e^- \quad (35)$$

3.3.2.2 Charge Transport Along the NC Surface

Surface water dissociates into proton and hydroxyl group (Equation 36), with their concentrations defined by the dissociation constant, K_w. As water layer is formed on the

NC surface, the generated ions may electromigrate in the liquid. When surface water is limited at higher temperatures, the protons can also be adsorbed onto the surface of ceria, and migrate on the solid surface under an applied electric field (Equation 37).[105, 107] $O_o^x\_H^+$ in the equation stands for a proton chemisorbed onto the surface oxygen ion in the NC lattice through the hydrogen bond.

$$H_2O(l) \rightleftarrows H^+(aq) + OH^-(aq) \tag{36}$$

$$H^+(aq) + O_o^x(s) \rightleftarrows O_o^x\_H^+(s) \tag{37}$$

Charge transport on NC can also go through chemical reactions at higher temperatures. Water molecules can be chemisorbed onto NC, filling oxygen vacancies that are present on NC, each releasing two protons. The two protons can both bond to a single lattice oxygen ion (Equation 38) or each bond to one oxygen ion (Equation 39).[105, 107] In this case, defects (oxygen vacancies) take part in the reaction and facilitate the water dissociation. Equation 39 is more common due to the stronger steric effect of double-proton configuration in Equation 38.[105]

$$H_2O(l) + V_o^{\cdot\cdot}(s) \rightleftarrows O_o^x\_2H^+(s) \tag{38}$$

$$H_2O(l) + V_o^{\cdot\cdot}(s) + O_o^x(s) \rightleftarrows 2O_o^x\_H^+(s) \tag{39}$$

The charge generation and transport processes determine the ionic dynamics of the NC, and are the result of the surface potential evolution observed in tr-KPFM. Driven by the applied electric field, protons are generated at the TPB and accumulate in the proximity

of the biased electrode, which causes a potential increase in this area. During relaxation, without an external driving force provided by electric field, the accumulated charges slowly dissipate toward two grounded electrodes, which are infinite reservoir of electrons, and later they discharge on the electrodes. The above summarized ionic dynamics are illustrated in a schematic, as shown in Figure 3-12.

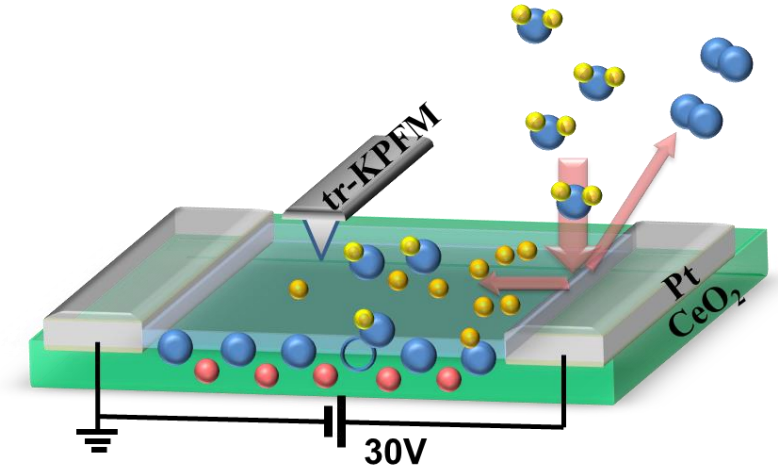

Figure 3-12 – Schematic of the ionic dynamics taking place on NC surface.

3.3.3 Conduction Pathways

To understand the conduction pathways of these films, i.e. whether the protons and hydroxyl groups are transported through the surface or the bulk of NC films, the tr-KPFM measurements were performed as a function of thin film thickness. As shown in Figure 3-13a, for sample as thin as 10 nm, obvious potential variation is still observed at 110 °C and 0% RH. Increasing the thickness of the samples (Figure 3-13b and c) does not show a stronger polarization and relaxation behavior, on the contrary, the potential variation even slightly decreases. This suggests that the bulk of NC does not significantly contribute to the proton generation and transport. For a thicker film, protons generated on the surface

may transport towards the grain boundaries and nano-grooves of NC, lowering the proton concentration at the NC surface, and therefore results in the slightly decreased surface potential variation.

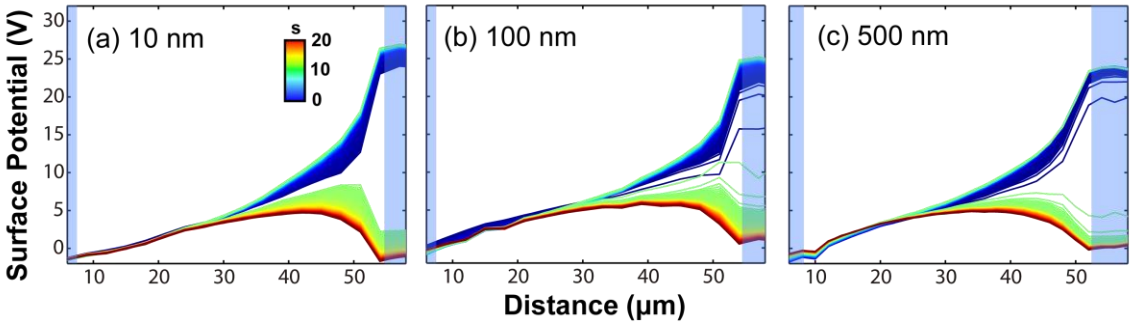

Figure 3-13 – Surface potential vs. time and position as a function of the thickness of NC thin films. The measurements were performed at 110 °C and 0% RH. The blue shaded areas correspond to the position of electrodes.

From the above analysis, it is suggested that the protons are mostly generated on the surface of NC within 10 nm thick. The inner grains have limited access to water, therefore have less contribution to the proton generation. Moreover, the protons generated on the surface may transport inside the bulk, either through open pores or through inner grain boundaries, which lower the detected surface potential variation.

3.3.4 Other Factors

In addition to the contributions from the electrochemical reactions at the triple phase boundary (TPB) discussed in the previous section, the surface potential measured by tr-KPFM may also depend on several other factors. First and foremost, the surface potential measured by tr-KPFM is obtained from the contact potential difference (CPD) between the NC surface and the scanning tip. So it differs from the absolute surface potential by a factor

of the work function difference ($\Delta\chi$) between NC and platinum, i.e. $V_{act} = V + \frac{\Delta\chi}{e}$, where V_{act} is the actual surface potential, V is the measured surface potential and e is the elementary charge. The work functions of ceria and platinum are 4.69 eV and 5.4 eV, respectively.[156] Therefore, the measured surface potential differs from the actual value by no more than 0.71 V, which is negligible compared to the potential changes caused by proton and hydroxyl transport (several or tens of volts).

The surface potential may also have contributions of band bending behavior near a junction (TPB). When two materials are in contact (in this case, ceria and Pt), the band structure of these materials will change, due to a local imbalance of charge neutrality. However, the width of the depletion region due to band bending is typically less than 100 nm, and cannot be in the micron range. The active area, where the surface potential significantly changes spreads tens of microns away from the TPB. Therefore, the effect of band bending behavior is negligible in this study.

We note that not only contributions of CPD and band bending to surface potential are negligible in these experiments, they are also not dynamically active: the surface potential variation caused by CPD and band bending is static, and will not change over time, while the generation and transport of proton and/or hydroxyl groups keeps changing over time, resulting in surface potential variation. Therefore, any of these factors does not influence the analysis and theoretical simulations of the water splitting and ionic transport processes on NC.

3.4 Effects of Triple Phase Boundaries

To study the effects of triple phase boundaries (TPBs), a second configuration of lateral device with limited TPBs was prepared. While the exposed-TPB devices has NC/Pt electrode interface directly exposed to the ambient, in the limited-TPB devices, the electrodes were deposited prior to the deposition of NC, so the Pt/NC interface has limited interaction with the environmental gas. Figure 3-14 shows the potential profiles measured on limited-TPB devices at various temperature and humidity. The potential profiles at 25 °C (Figure 3-14a and b) are somewhat similar to the ones observed on the exposed-TPB devices. However, at 125 °C and in absence of humidity (Figure 3-14c), the surface potential variation is substantially limited compared to the fully exposed-TPB platforms (Figure 3-9c).

At lower temperatures, while TPB is not macroscopically present in the limited-TPB devices, nanostructured grooves present on NC can serve as water and gas delivery micro-channels to the platinum, creating localized TPB. At higher humidity levels, water and oxygen molecules can permeate the NC film, resulting in electrochemical reactivity at the microscale TPB locations. Meanwhile, the generated protons are transported through the channels rapidly, resulting the strong polarization and relaxation behavior all over the surface. At higher temperatures and low humidity levels, however, the condensed water layer begins to desorb from the NC surface, substantially reducing proton transport pathways. Therefore, the charge transport is assumed to be a diffusion-limited process: the protons generated at the Pt/NC interface in the limited-TPB samples are “buried” under the NC layer and therefore, the accumulated products substantially reduce the electrochemical reactivity on the surface.

The inter-electrode current for each of the samples are shown in Figure 3-15. For samples measured at 25 °C and 125 °C in absence of humidity, the current was not detectable (Figure 3-15a and c), which is the same as the current measured for the exposed-TPB samples. At 90% RH and 25 °C, the current is detectable as expected, due to a rather strong proton generation. However, instead of a decreasing current observed in the exposed-TPB samples, the current increases during polarization, and reaches saturation of about 0.05 nA, as shown in Figure 3-15b. This is because protons are first generated beneath the NC film, where the current is relatively small due to limited proton transport. Over time the protons diffuse onto the surface through the micro-channels of NC. Protons are transported more easily on the surface, therefore results in an increase of the current.

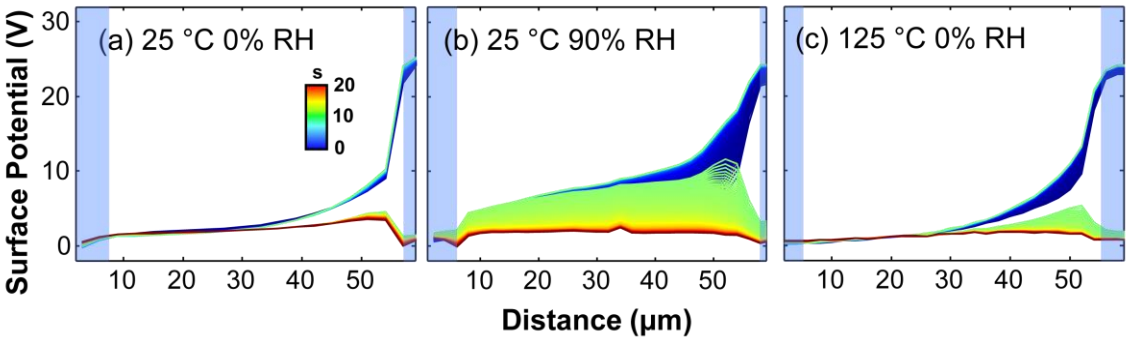

Figure 3-14 – Temperature and humidity dependence of surface potential vs. time and position for limited-TPB devices measured at: (a) 25 °C and 0% RH; (b) 25 °C and 90% RH and (c) 125 °C and 0% RH. The blue shaded areas correspond to the position of electrodes.

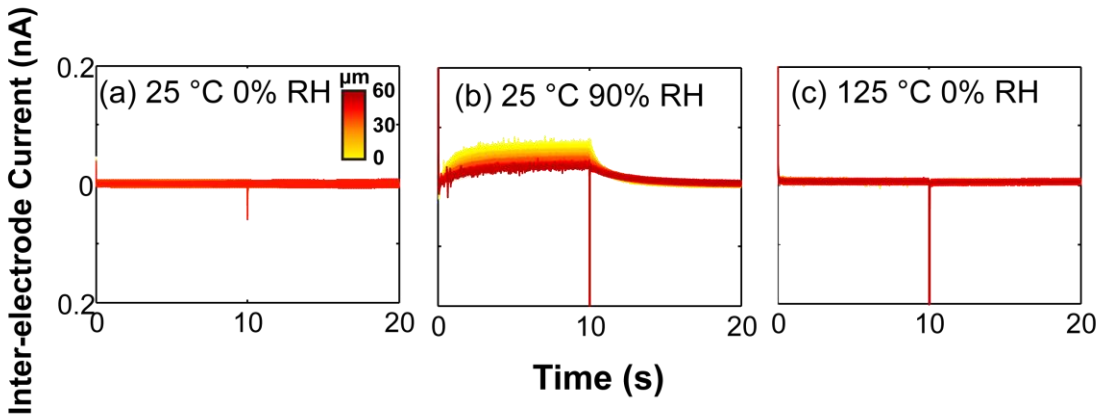

Figure 3-15 – Inter-electrode current evolution over time as a function of distance for limited-TPB devices measured at: (a) 25 °C and 0% RH; (b) 25 °C and 90% RH and (c) 125 °C and 0% RH.

3.5 Effects of Atmosphere

To further illustrate the role of oxygen pressure in the conduction mechanisms at TPB, tr-KPFM measurements were also performed in nitrogen atmosphere, as shown in Figure 3-16. At 25 °C (Figure 3-16a and b), no distinct difference of polarization and relaxation behavior is observed between nitrogen and air atmosphere. While at elevated temperatures (Figure 3-16c), the potential variation is much stronger as compared to the same conditions in air (Figure 3-9b), suggesting an enhanced proton accumulation and transport rate at such conditions.

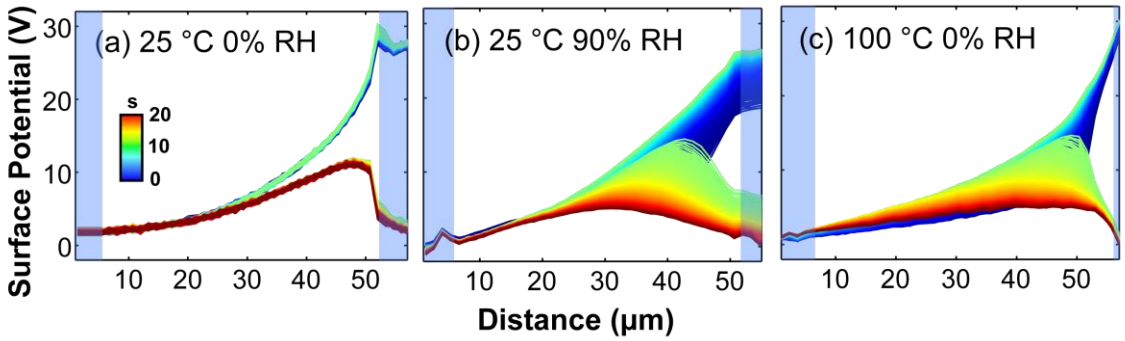

Figure 3-16 – Surface potential vs. time and position in nitrogen atmosphere measured at: (a) 25 °C and 0% RH; (b) 25 °C and 90% RH; (c) 100 °C and 0% RH. The blue shaded areas correspond to the position of electrodes.

In nitrogen atmosphere, the effective p_{O_2} is infinitesimally small or null, and a larger concentration of oxygen vacancies may form in the NC film (Equation 20). According to the Ellingham diagram, the equilibrium oxygen partial pressure for the reduction of CeO_2 to Ce_2O_3 at 400 K is as low as 10^{-14} Pa, indicating the CeO_2 phase is thermodynamically stable at measured temperatures. However a highly stable of Ce^{3+} can be expected on the NC surface.[173] A combination of low oxygen partial pressure, and high applied voltage may allow for an increase in oxygen vacancy concentration in NC in the measured experimental conditions. Oxygen vacancies are reported to be the active sites for many electrochemical processes, especially at elevated temperatures.[5, 109, 174-176] In fact, theoretical calculations suggest that water is more easily adsorbed onto a reduced ceria surface due to a lower energy barrier for water decomposition at oxygen vacancies,[105] which can serve as catalytic sites. At room temperature, in presence of physisorbed water layers, direct water dissociation at TPB is dominant. At the same time, the role of oxygen vacancies formed on the NC surface and TPB is limited, because most of the conducting species are not directly interacting with the NC surface. At elevated temperatures, however,

the water layer gradually evaporates, and a larger interaction of the charged species with the surface oxygen vacancy is expected, and more protons are generated due to the catalytic functionality of oxygen vacancies. Further quantitative analysis is carried out via theoretical simulation, which is presented in the next section.

3.6 Activation Energy and Conduction Pathways

The averaged time constant τ during both polarization and relaxation are obtained from fitting experimental data to Equation 34 at each temperature at RH = 0%. Figure 3-17 shows a clear Arrhenius-like behavior of τ, indicative of a thermally-activated process with two distinct regions, which implies contributions from two distinct conduction mechanisms. The activation energy for each region is calculated according to:

$$\tau = Ae^{-\frac{E_a}{kT}} \tag{40}$$

where A is the pre-exponential factor, k is Boltzmann constant, and E_a is the activation energy for charge transport.

At T < 100 °C, E_a are 0.10 ± 0.02 eV and 0.09 ± 0.02 eV for polarization and relaxation processes, respectively. These values are very close to the E_a reported for proton conduction in liquid water (0.12 eV),[177, 178] supporting the hypothesis of proton-assisted conductivity on the ceria surface in a physisorbed water layer. [179, 180]

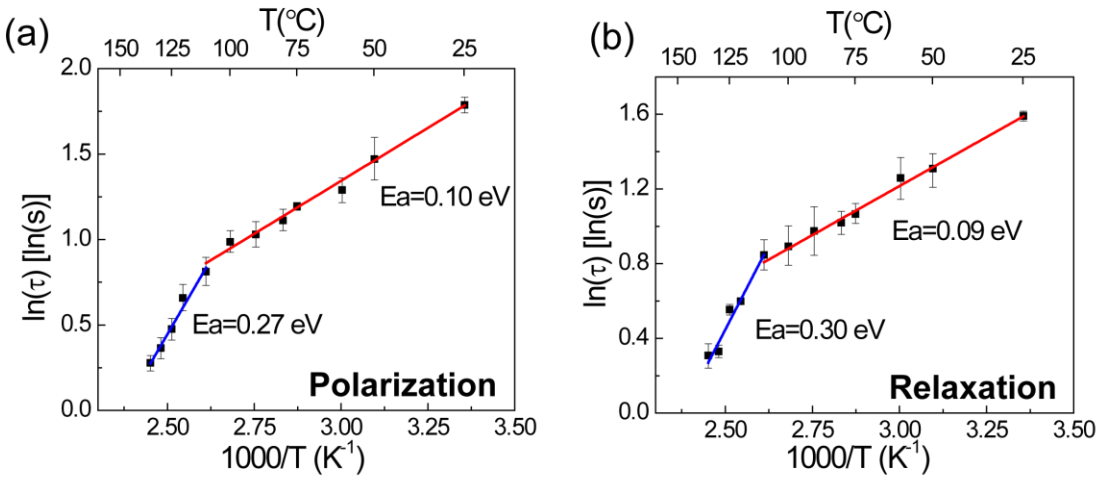

Figure 3-17 – The averaged time constant (τ) as a function of temperature (T) at 0% humidity in air during (a) polarization stage and (b) relaxation stage.

At temperatures from 100 °C to 135 °C, the activation energy is approximately 0.27 eV ± 0.02 eV and 0.30 eV ± 0.03 eV for polarization and relaxation, respectively. The oxygen ion conduction is likely not yet activated,[172, 181, 182] due to the much higher activation energy for oxygen transport (0.5 to 1.2 eV).[39, 113, 183] Under this condition, proton transport is still expected to be active via hopping between the first-layer water molecules that are chemisorbed on NC surface lattice, according to the Grotthuss mechanism (Equation 41).[7, 30, 179]

$$Ce_{Ce}^{\times} - OH_3^{\cdot} + Ce_{Ce}^{\times} - OH_2 \rightleftarrows Ce_{Ce}^{\times} - OH_2 + Ce_{Ce}^{\times} - OH_3^{\cdot} \quad (41)$$

The higher activation energy at elevated temperature is consistent with a reduced contribution of proton conduction, due to water desorption and the transition from physisorbed to chemisorbed water. The activation energy for ceria conductivity has been previously reported to be 0.26 eV in dry air at 125 °C to 200 °C, which is very close to the

value obtained here in the 100-135 °C range.[39] However, the same study did not report conductivity values below 125 °C, presumably due to the limitations of EIS measurement. The activation energy at higher temperatures found here is also similar to that reported by Raz et al. (0.30 eV) for proton transport in chemisorbed water, in yttrium-stabilized zirconia (YSZ).[30] Considering that both NC and YSZ have a fluorite structure, it is reasonable to assume that the proton conductivity behaviors are similar in the temperature range where the bulk conductivity is still inactive, i.e. protons are transported along the physisorbed water layer at lower temperatures, and along the chemisorbed water layer at higher temperatures.

3.7 Substrate Dependence

The effect of substrate on the ionic dynamics was also studied. Figure 3-18 presents the representative surface potential mapping of NC deposited on quartz substrate via CSD. Similar to the Si_3N_4/Si substrate, with increase of RH at 25 °C, the surface potential variation becomes stronger, and with increase of temperature at 0 RH, the surface potential changes much faster. However, it is worth noting that the surface potential profile at the initial state (t = 0 s) is different from that of Si_3N_4/Si substrate, which is probably due to the different dielectric constant and screening effect of these two substrate. For semiconductor Si, the accumulation of negative electrons under the biased electrode results in a much lower surface potential around this area, which may also trap more protons. This is an interesting effect that allows us to control surface ionic dynamics, either making it concentrate more at electrodes or at bulk using external screening by substrate, and hence explore differences in kinetics.

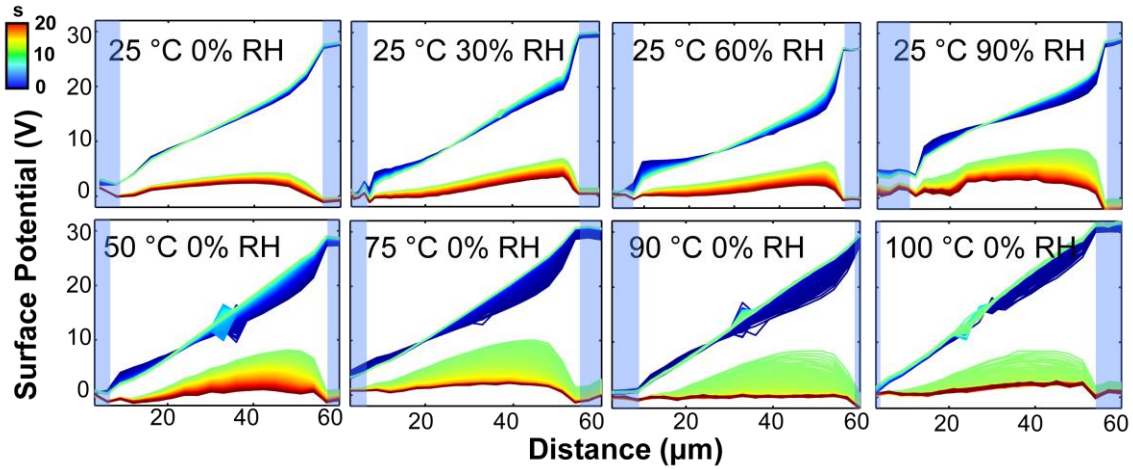

Figure 3-18 – Surface potential vs. time and position as a function of temperature and humidity measured on quartz substrates. The blue shaded areas correspond to the position of electrodes.

3.8 Conclusions

In this chapter, NC thin films grown by CSD are used for transport mechanisms study by tr-KPFM. We find that the detected surface potential change over time is mainly a result of transport of protons and hydroxyl groups. During polarization stage, water molecules in the ambient are decomposed into protons in proximity to the biased electrode. They accumulate and migrate to the grounded electrode under electric field, resulting in a potential increase. During relaxation stage, the accumulated charge carriers dissipates and move towards the two electrodes, resulting in a decrease of surface potential.

The electrochemical reaction and transport process are studied as a function of external conditions. With increasing humidity and temperature, the potential change becomes much stronger, suggesting a crucial role of the surface water in the ionic dynamics. It is concluded that water splitting reaction is taking place during polarization stage, and

the resulting protons and hydroxyl groups are the main conducting species along the NC surface. These charge carriers are mainly conducting within 10 nm of the sample surface.

It is also demonstrated that such electrochemical reactions are taking place at TPB. At 125 °C, the electrochemical reaction is limited for sample with limited TPBs. The proton transport on NC is stronger in nitrogen atmosphere than in air, suggesting that oxygen vacancies may facilitate the proton generation and migration along NC.

Quantified analysis shows an Arrhenius-like behavior of τ, suggesting a thermally-activated process of proton transport. The activation energy shows two distinct regions, which implies contributions from two distinct conduction mechanisms. At low temperatures (T<100 °C), protons are assumed to generate and transport on surface physisorbed water. Whereas at higher temperatures (T>100 °C), protons are conducted through chemisorbed water that has direct contact with NC.

CHAPTER 4. FINITE ELEMENT MODELING OF IONIC DYNAMICS OF NC

4.1 Introduction and Model Description

In this section, the finite element method (FEM) for ionic dynamics of NC was performed using COMSOL multiphysics® 4.4. The export of model solution and parameter fitting was done on COMSOL LiveLink™ for Matlab® 4.4. The observed surface potential variation over time is a result of two processes, i.e. proton generation at biased electrode, and the subsequent proton transport toward the grounded electrode under electric field and chemical gradients, as discussed in the previous chapter. These physical processes can be expressed by Equation 42 and 43:[156]

$$\frac{\partial n_i}{\partial t} = \nabla \cdot (-D_i \nabla n_i + z_i \mu_i n_i \nabla \Phi) + (S_i - f_i n_i) \tag{42}$$

$$\nabla^2 \Phi = -\Sigma n_i z_i F / \varepsilon_0 \varepsilon_r \tag{43}$$

$$(\mathrm{i} = H^+, OH^-)$$

where t is time, n_i is concentration, D_i is diffusivity, μ_i is charge mobility, z_i is charge number per each ion, S_i is the charge injection rate and f_i is the dissipation constant for the i[th] species $(\mathrm{i} = H^+, OH^-)$. Φ is the surface potential, F is Farady's constant, ε_0 is permittivity of free space, and ε_r is the relative permittivity of NC. In Equation 42, it is postulated that charge concentration n_i changing over time is determined by D_i from

Fick's law of diffusion (chemical gradient) and μ_i from electron migration (electric potential gradient). In addition, S_i is a source term, which describes proton generation during polarization stage due to the water splitting reaction at TPB. And the charge dissipation constant, f_i takes into account the possibility of charge annihilation due to electrochemical reaction or neutralization. Equation 43 is the Gauss's Law, which defines the surface potential variation due to proton concentration change over time.

The basic assumptions, boundary conditions and initial conditions for the model are as follows: a) We assume an ion blocking electrode, which means that ions will not migrate outside or inside ceria through the electrodes. b) $\Phi = 0\,V$ at the grounded electrode and 30 V at the biased electrode during polarization. c) Φ is assumed to be zero all over ceria, at $t = 0\ s$. d) The dissociation constant $K_w = 10^{-14}$,[176] hence at $p\mathrm{H} = 7$, initial conditions are chosen as $n_i = 10^{-7}\ mol/L$ for both protons and hydroxyl groups. e) Diffusivity and mobility of protons are assumed to be two times that of hydroxyl groups: $D_{H^+} = D = 2D_{OH^-}$, $\mu_{H^+} = \mu = 2\mu_{OH^-}$.[184] f) Protons are generated during polarization stage; according to water splitting reaction (Equation 35), no hydroxyl groups are generated: $S_{p\_H^+} = S$, $S_{r\_H^+} = S_{p\_OH^-} = S_{r\_OH^-} = 0$. S is assumed to be a step function of distance, with a non-zero constant value at 1-μm-long area in immediate vicinity of the anode TPB, and zero on the remaining 49-μm along the ceria stripe. g) The dissipation rate constant of hydroxyl groups are neglected, and that of protons is assumed to be the same for both polarization and relaxation processes, and is mainly effective at TPB region: $f_{p\_H^+} = f_{r_{H^+}} = f$.

Thus, four unknown parameters remain in this model: 1) Proton injection rate at TPB (S); 2) Proton dissipation constant (f); 3) Proton diffusivity (D); and 4) Proton mobility (μ). The first two parameters determine the electrochemical processes at TPB, and the last two determine the subsequent charge transport processes. For each set of the four unknown parameters, the finite element modeling is able to solve the proton concentration n as well as the surface potential Φ in real time as a function of distance. These physical parameters determine the electrochemical reactivity and transport properties of the ions, therefore control the shape of the simulated mapping of potential change. For example, a higher S results in higher potential change during the polarization stage, because more protons are generated and accumulated in the system; while a higher f and μ results in a faster dissipation of surface charge and thus a faster change rate of surface potential. This leads to a smaller time constant, or, in a visualized way, more separation between subsequent (in the temporal scale) potential curves. The finite element analysis in this chapter aims to find the optimized parameter values that best match the experimental potential change mappings, providing quantified physical processes at each condition. The details of the finite element analysis are introduced as follows.

The data obtained from tr-KPFM is a three-dimensional matrix, which is time- and x, y-dependent surface potential, $M(t, x, y)$. A typical measurement is 20 s long with 10 ms temporal resolution and 2 μm spatial resolution for 60 μm × 6 μm 2D surface scan region (30 × 3 grid points), so the obtained data size is 2000 × 20 × 3. By averaging each of the three data points equidistance from the grounded electrode, the data matrix is shrunk to 2000 × 30: $M(t, d)$, where d is the distance along x axis (perpendicular to the electrodes).

In simulation, for any input parameters S_1, f_1, D_1 and μ_1, Equations 42 and 43 are solved, which is surface potential value as a function of time and distance. This matrix has dimensionality determined by the COMSOL meshgrid, and is then converted into a matrix of the same size (i.e. 2000 × 30) as $M(t,d)$ via extrapolation, $N_{S_1,f_1,D_1,\mu_1}(t,d)$.

The degree of similarity is calculated in one step via correlation coefficient in Matlab (*corr*2):

$$corr2([M,N]) = C_{M,N} = \frac{\sum_i \sum_j (M_{ij} - \bar{M})(N_{ij} - \bar{N})}{\sqrt{(\sum_i \sum_j (M_{ij} - \bar{M})^2)(\sum_i \sum_j (N_{ij} - \bar{N})^2)}} \quad (44)$$

The output correlation coefficient between M and N, $C_{M,N}$, ranges from -1 (negatively correlated) to 1 (positively correlated). The primary goal of the fitting is to find parameters that generate results with largest $C_{M,N}$.[185] The optimized $C_{M,N}$ for each environmental condition varies, and typically ranges from 0.900 to 0.975. The surface potential data with strong polarization and relaxation behavior often has higher $C_{M,N}$, due to a lower relative error. A threshold of 0.9 was set to distinguish between poorly fitted data and well fitted data. The detailed steps for parameters fitting that optimize $C_{M,N}$ at each environmental condition are shown as follows:

1. Start with an arbitrary set of initial values, S_0, f_0, D_0 and μ_0, solve FEM and obtain the surface potential matrix, $N_0(t,d)$, and the corresponding degree of similarity C_{M,N_0} (assume the experimental data is $M(t,d)$).

2. Find *D* until getting the same time constant value as experimental one.

3. Utilizing the relaxation data, keep other parameters the same, and find *f* that gives largest $C_{M,N}$

4. Using the optimized *D* and *f*, find *S* that gives largest $C_{M,N}$ using the polarization data.

5. With fixed *D*, *S*, and *f*, find optimized μ that gives largest $C_{M,N}$.

6. With optimized *S*, *f* and μ, find *D* that gives largest $C_{M,N}$. Update all the four parameters.

7. Reiterate starting at step 3 until all parameters stabilize.

Thus, FEM not only allows quantification of the observed processes, but also decoupling of the various contributions to the measured signal. Examples of the experimental and simulated surface potential changes (as compared to initial stage of polarization or relaxation) are presented in Figure 4-1, with the optimized fitting parameters shown in the insets of Figure 4-1b and d. The corresponding proton concentrations are shown in Figure 4-2. The highest proton concentration the system can achieve in our tr-KPFM measurements is about $5\times10^{-6}\ mol/L$, or $p\mathrm{H} \approx 5.3$. Thus, the standard potential of NC is changed by $2.3\times\frac{RT}{nF}\times\Delta p\mathrm{H} = 0.059\times(7-5.3) < 0.1\mathrm{V}$. The standard potential change of NC system is negligible when compared to the potential changes of the surface potential, which are mostly several or tens of volts.

The finite element analysis was performed at a variety of external conditions on exposed-TPB NC/Si_3N_4/Si devices, i.e. the data obtained in CHAPTER 3. The "phase

diagrams" was constructed for each parameter as a function of temperature and humidity, in different atmosphere, which will be illustrated in the section 4.2.

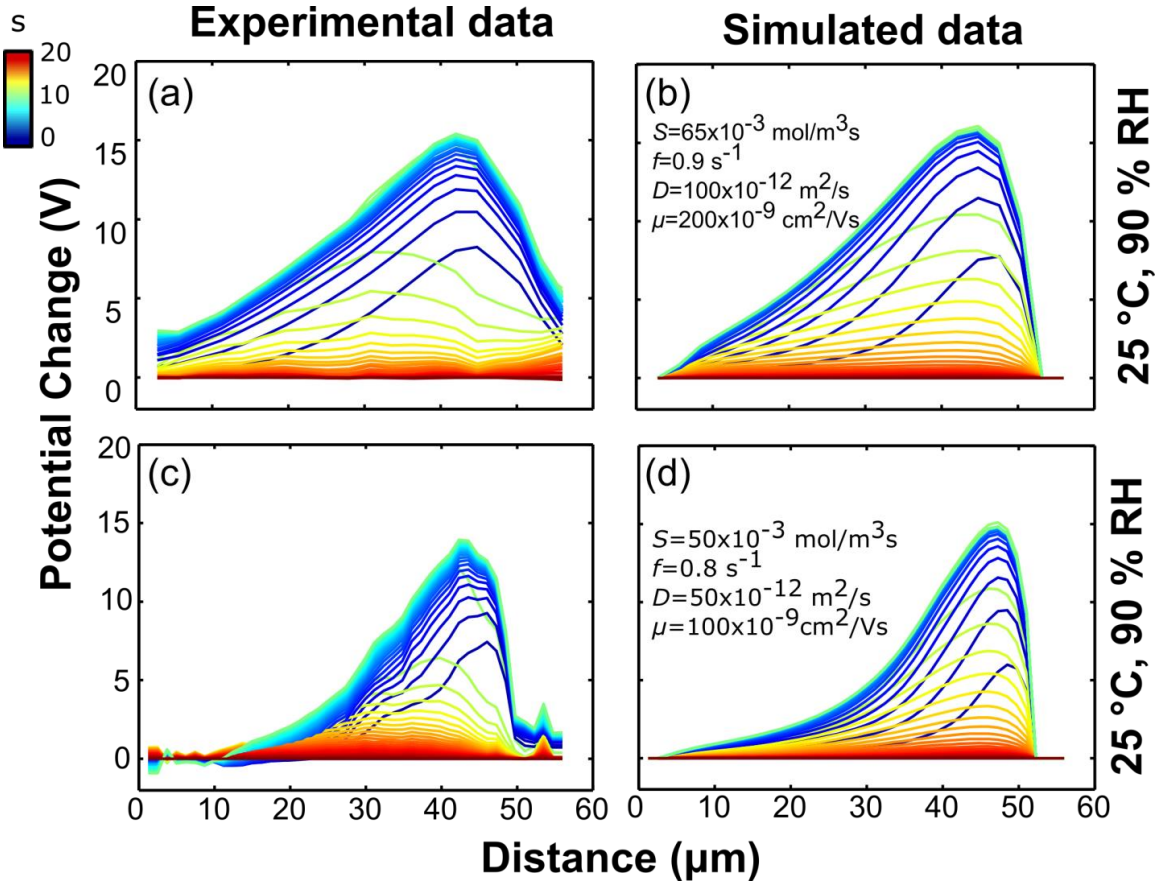

Figure 4-1 – Experimental and simulated data for potential change at (a, b) 135 °C and 0% RH and (c, d) 25 °C and 90% RH.

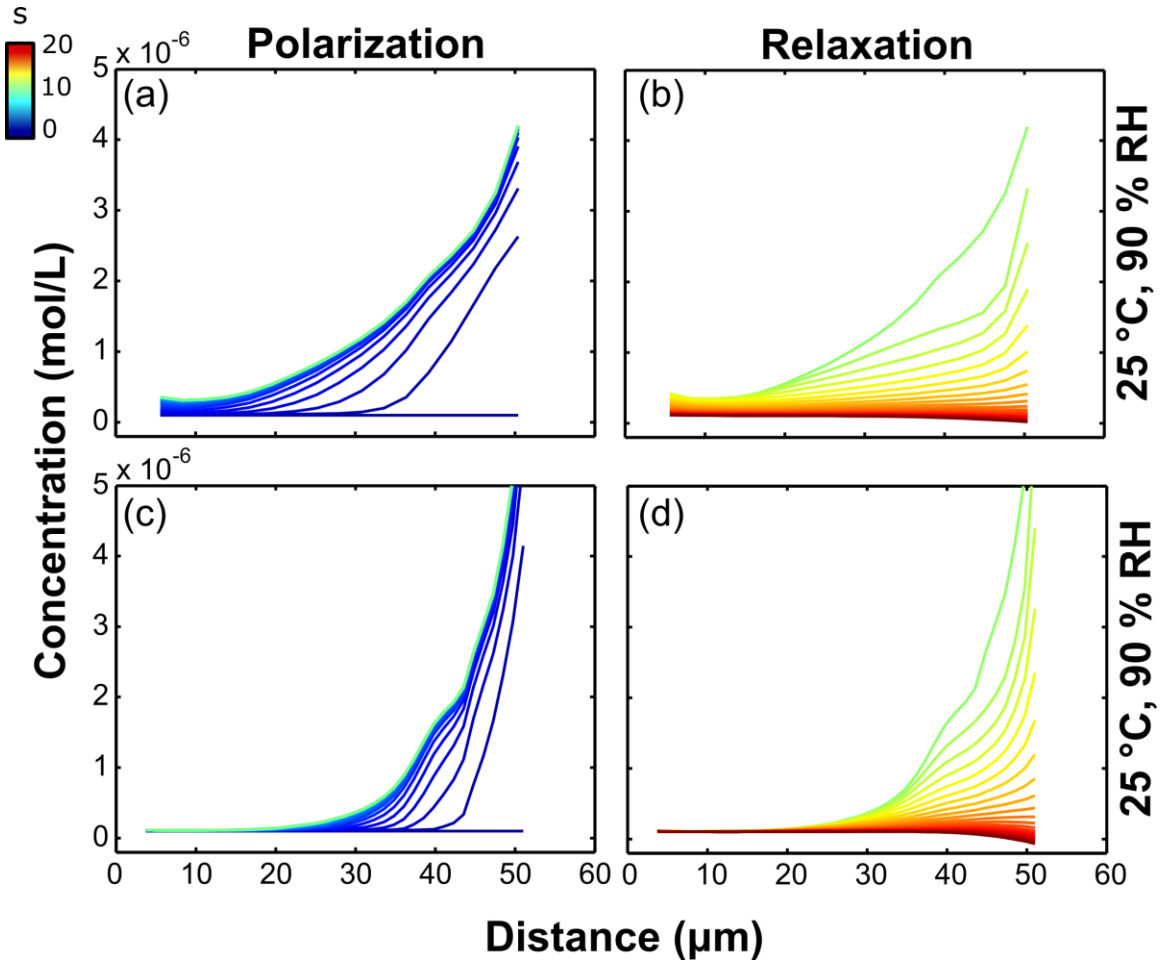

Figure 4-2 – Simulated proton concentration on NC surface as a function of time and distance for polarization (a, c) and relaxation (b, d) processes for (a, b) 135 °C and 0% RH and (c, d) 25 °C and 90% RH.

4.2 Phase Diagrams of Physical Parameters

4.2.1 The Reaction Rate Phase Diagrams

The rates of the forward and reverse reactions of water injecting reaction (Equation 35) are given by: $-\frac{d[H_2O]}{dt} = k \cdot [H_2O]$ and $-\frac{d[H^+]}{dt} = 2k' \cdot [H^+]^2 \cdot p_{O_2}^{1/2}$, respectively. Here the water concentration ($[H_2O]$), proton concentration ($[H^+]$) and partial oxygen pressure

(p_{O_2}) refer to those at the TPB interface, and k and k' are the reaction constants of the forward and reverse reaction. Comparing this to Equation 42, we obtain:

$$S = \frac{d[H^+]}{dt} = 2k \cdot [H_2O]; \;\; fn_{H^+} = -\frac{d[H^+]}{dt} = 2k' \cdot [H^+]^2 \cdot p_{O_2}^{1/2} \qquad (45)$$

The exponent for n_i in Equation 42 and $[H^+]$ in Equation 45 differ, since Equation 45 is a first approximation descriptor of the system. However, Equation 45 allows a direct look at the rate of proton injection S and the proton dissipation rate f, and how they are related to the concentration of chemical species and reaction constant.

Figure 4-3a and b show the dependence of S on the absolute humidity (AH) and temperature (T), as measured in air and nitrogen atmosphere, respectively. Experiments performed at 25 ˚C and low humidity have relatively weak polarization and relaxation responses, resulting in considerable inaccuracy, so those data points are not included in the phase diagrams. Comparison of the phase diagrams of S for air and nitrogen atmospheres qualitatively demonstrates the important role of oxygen partial pressure on the electrochemical processes. S is larger in nitrogen than in air, especially at higher temperatures, indicating the important role of oxygen partial pressure and possible catalytic behavior of oxygen vacancies on the electrochemical reactivity. This result is consistent with the experimental observations in CHAPTER 3.

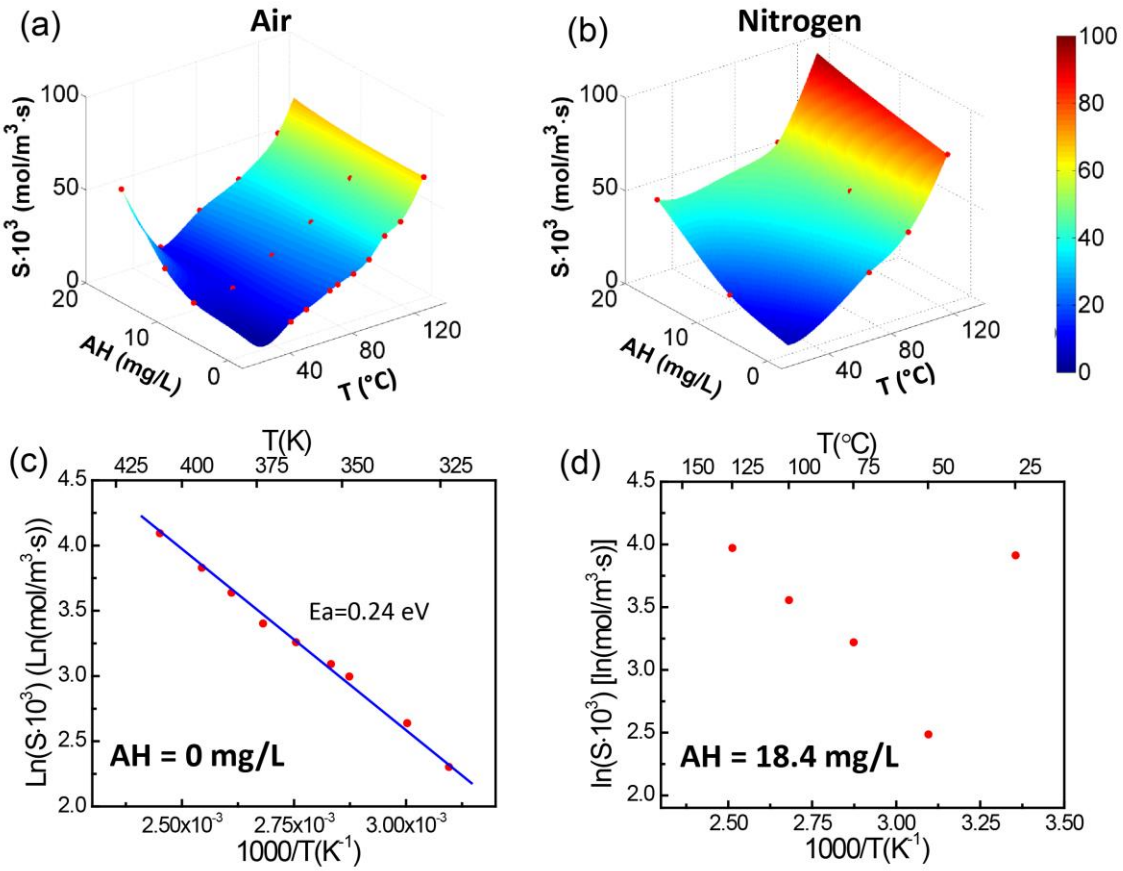

Figure 4-3 – Charge injection rate (*S*) phase diagrams as a function of absolute humidity (AH) and temperature (T) in (a) air atmosphere and (b) nitrogen atmosphere. The Arrhenius plot of S in air atmosphere are plotted at (c) AH = 0 mg/L and (d) AH = 18.4 mg/L. Red dots are experimentally measured data; colored surfaces in (a), (b) are interpolated data; blue line in (c) is linear fitting of experimental data.

Reaction rate *S* linearly depends on humidity at 25 °C in both air and nitrogen atmospheres, as water can freely condense on the surface, and [H_2O] increases with increasing humidity. Therefore, *S* is likewise proportional to humidity, in accordance with Equation 45. The temperature dependence of *S* in air at 0% humidity (AH = 0 mg/L) and at high humidity (AH = 18.4 mg/L) is extracted from Figure 4-3a, and the corresponding Arrhenius plots are shown in Figure 4-3c and d. The linear behavior of ln(*S*) in Figure 4-3c indicates that the proton injection at TPB is thermally activated, with activation energy to

be around 0.24 eV (23.16 kJ/mol). This value is much lower than the activation energy of water splitting reaction ($k \approx 1.1$ eV),[12] because S is proportional to both k and $[H_2O]$. While k is expected to increase exponentially with T, $[H_2O]$ slightly decreases due to water desorption. Similarly, at high humidity (Figure 4-3d), the high value of S at 25 °C can be assigned to the ease of water condensation on NC (i.e., due to high $[H_2O]$),[35, 171] which facilitates proton generation as discussed above. The desorption of this "thick" water layer at ≈30 to 60 °C causes tremendous decrease in $[H_2O]$, which results in a sudden drop of S. With further increase in temperature, the humidity has less effect on the surface water condensation, due to the low relative humidity, so S shows similar trend as that in absence of humidity. In fact, the slope of the temperature-dependence of S (0.24 ± 0.1 eV vs. 0.21 ± 0.02 eV) is similar in both cases for temperatures in excess of 325 K.

The phase diagrams of f in both air and nitrogen atmosphere are presented in Figure 4-4a and b. With increasing temperature, f increases due to the increase of k'. With increasing humidity, f also increases, presumably due to the larger proton pathways provided by the thick water layer, which provide more reaction sites for proton dissipation. A decrease of oxygen pressure may seem to decrease f according to Equation 45; however a higher f is obtained in nitrogen atmosphere. This indicates that compared to S, f is a much more complicated parameter and the reverse reaction of Equation 45 is only a first approximation descriptor of the system. In fact, f may also be affected by the charge neutralization of the ambient gas and screening effect of the surface. In nitrogen gas, the higher oxygen defects generated on the surface may also facilitate proton migration and dissipation.

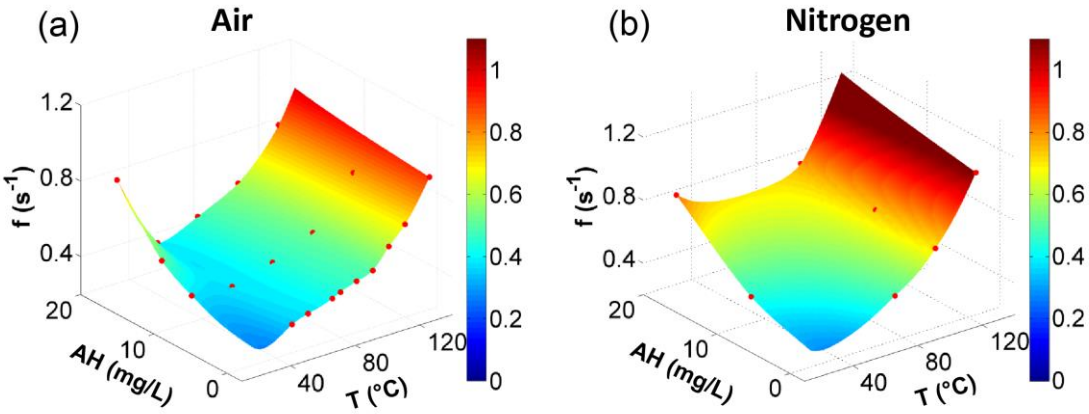

Figure 4-4 – Dissipation constant (*f*) phase diagrams as a function of absolute humidity (AH) and temperature (T) in (a) air atmosphere and (b) nitrogen atmosphere. Red dots are experimentally measured data, and others are interpolated data.

The phase diagrams for *S* and *f* as a function of T and RH are shown in Figure 4-5. At same absolute humidity, the RH at higher temperatures is much smaller, which explains why the parameters do not show obvious dependent on absolute humidity at elevated temperatures.

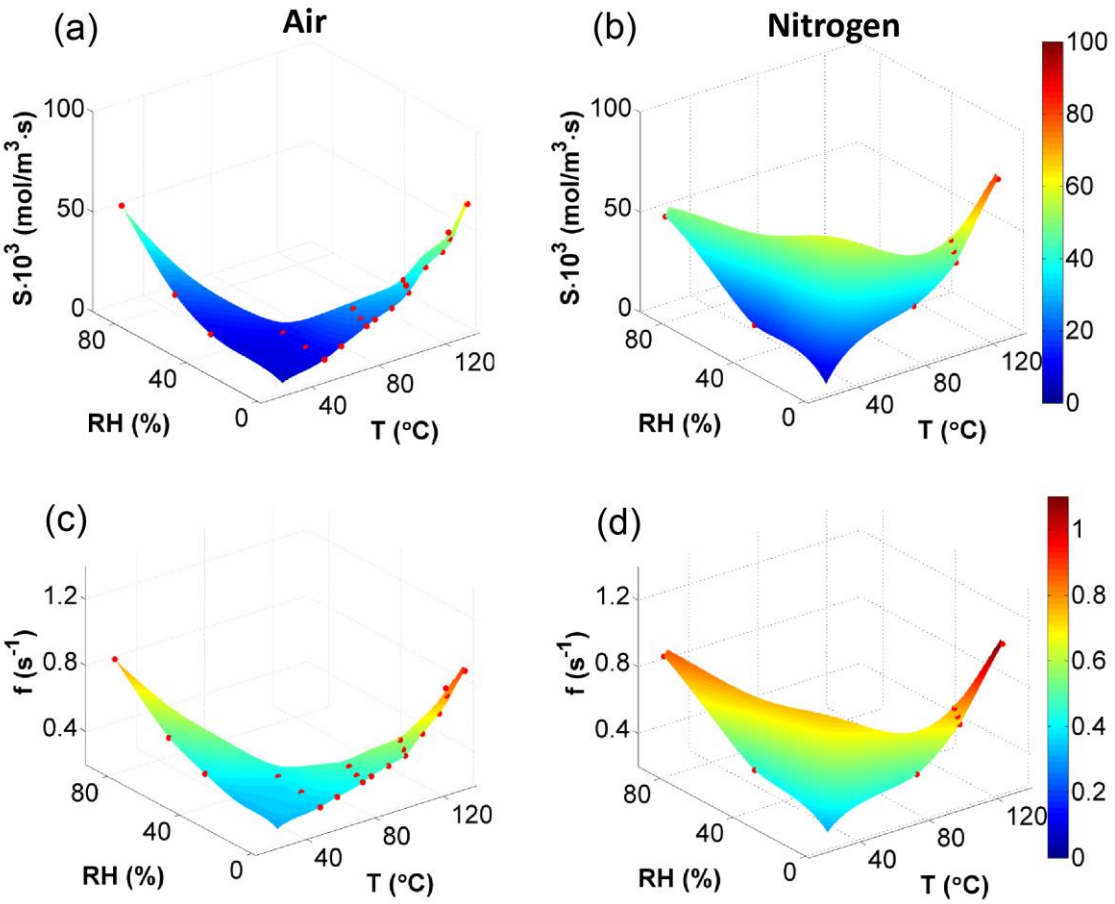

Figure 4-5 – Charge injection rate (*S*) and dissipation rate (*f*) phase diagrams as a function of relative humidity (RH) and temperature (T) in (a, c) air atmosphere and (b, d) nitrogen atmosphere. Red dots are simulated data, and colored surfaces are interpolated data.

4.2.2 The Transport Phase Diagrams

The behavior of diffusivity D and mobility μ reflects the proton transport process along the NC surface. The phase diagrams of D in air and nitrogen atmosphere are shown in Figure 4-6a and b, respectively. The phase diagrams of μ are presented in Figure 4-7, which exhibits similar behavior. The value of D is higher in nitrogen, especially at elevated temperatures. This behavior is also consistent with the higher oxygen vacancy

concentration formed in the NC film, which may facilitate proton transport. The Arrhenius plot of *D* in air atmosphere at 0% humidity (AH = 0 mg/L) and at high humidity (AH = 18.4 mg/L) are shown in Figure 4-6c and d. *D* exhibits a somewhat similar behavior as *S*; however, at 0% humidity, two distinct regions can be identified with activation energies of 0.11 ± 0.03 eV and 0.28 ± 0.02 eV at temperatures below and above ≈100 °C, respectively. This is in very good agreement with the activation energy values extracted from the analysis of τ (Figure 3-17). *D* is expressed as:

$$D = D_0 e^{-E_a/kT} \tag{46}$$

where E_a is the activation energy for proton diffusion and D_0 is the pre-exponential factor. As the activation energy for proton transport along physisorbed water and chemisorbed water may significantly change, the Arrhenius plot of *D* also results in a kink, representing different transport mechanisms. We note, again, that unlike the τ plots, the *S* and *D* phase diagrams and Arrhenius plots present the deconvoluted picture of the studied processes. The absence of any clear discontinuity in the *S* plots, and presence thereof in the τ and *D* plots indicates that the behavior of τ is mainly due to diffusion, rather than electrochemical reactions. Therefore, the surface polarization and relaxation processes at the measured environmental conditions are diffusion limited. From the extracted *D* value, the diffusion length *d* in τ seconds is estimated to be around 10 μm, according to $d = \sqrt{D\tau}$, and is on the order of magnitude of the inter-electrode distance of our devices (*d* = 50 μm).

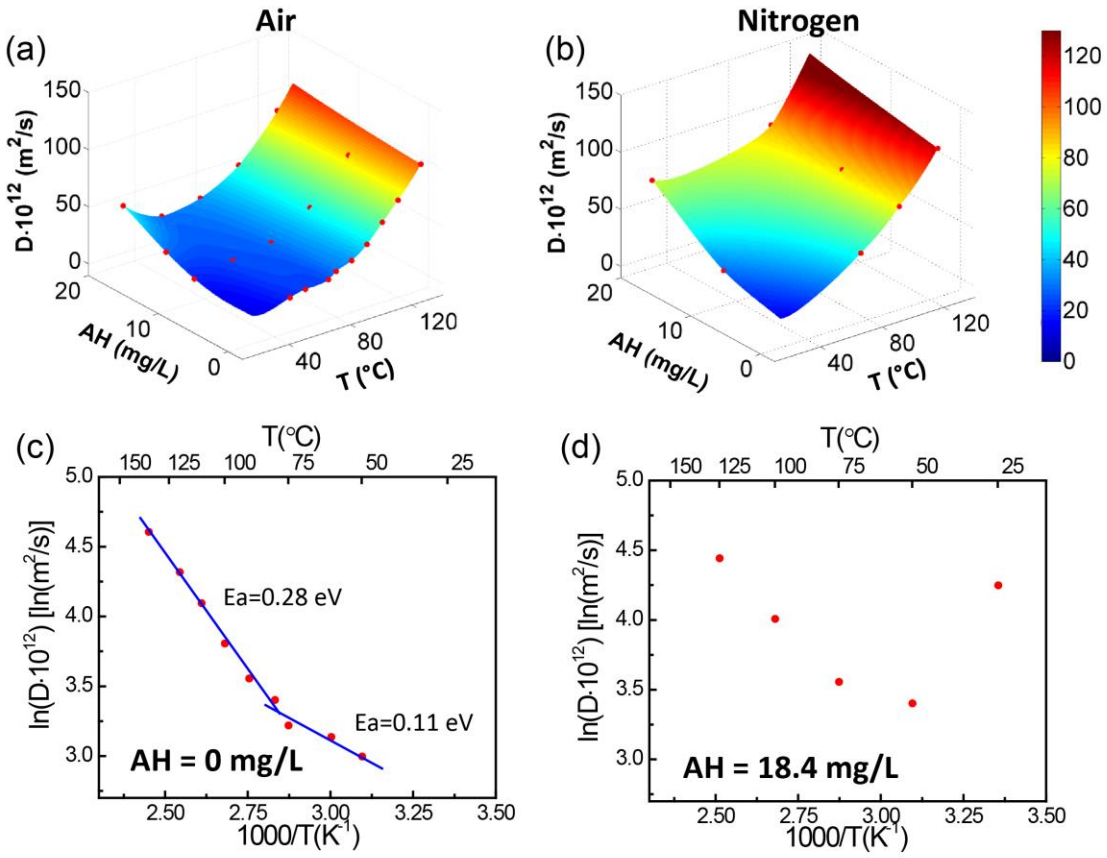

Figure 4-6 – Diffusivity (*D*) phase diagrams as a function of absolute humidity (AH) and temperature (T) in air (a) and nitrogen (b) atmosphere. The Arrhenius plot of *D* in air atmosphere are plotted at AH = 0 mg/L (c) and AH = 18.4 mg/L (d). Red dots are experimentally measured data; colored surfaces in (a), (b) are interpolated data; blue lines in (c) are linear fitting of experimental data.

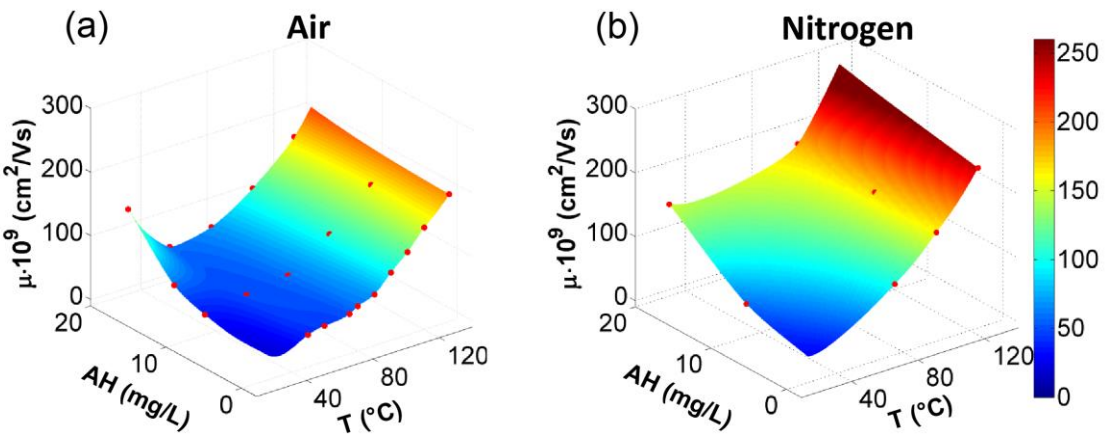

Figure 4-7 – Mobility (μ) phase diagrams as a function of absolute humidity (AH) and temperature (T) in (a) air atmosphere and (b) nitrogen atmosphere. Red dots are experimentally measured data; colored surfaces are interpolated data.

Similar to the analysis of the phase diagrams of *S*, the following descriptive model of the proton transport is put forward. At high humidity and room temperature, a thick layer of physisorbed water condenses on the NC surface, resulting in a larger number of pathways accessible for proton diffusion. This thick water layer desorbs from the surface at above ≈30 to 60 °C due to a decrease in relative humidity, and a thin physisorbed water layer remains on the surface, resulting the sudden drop of *D*. At temperatures above 100 °C, the physisorbed water mostly desorbs from the NC surface, leaving a limited amount of chemisorbed water, resulting in an increase of activation energy. *D* has a weak dependence on the ambient humidity level at high temperatures. This might be due in part to the conduction mechanism (i.e. chemisorbed water amount is relatively independent of the relative humidity in the atmosphere), but also owing to the very low amount of the remanent (relative) humidity at higher temperatures. Similar conductivity behavior in a wet atmosphere has been previously reported for nanocrystalline ceria and YSZ films.[38, 113]

4.3 Conclusions

In this chapter, electrochemical reaction and transport processes of the experiment performed in CHAPTER 3 were studied, and finite element method was used to quantify the physical parameters associated with these processes, which helps better understand the ionic dynamics on NC.

Specifically, the observed surface potential variation over time is mainly a result of two processes, i.e. proton generation at the biased electrode, and the subsequent proton transport toward the grounded electrode under electric field and chemical gradients. Four unknown parameters, i.e. proton injection rate at TPB (S), proton dissipation constant (f), proton diffusivity (D) and mobility (μ) were obtained via fitting to the experimental data at each environmental condition. It is found that the charge injection rate is a thermally activated process, with the activation energy to be around 0.24 eV. The activation energy of proton diffusivity, on the other hand, shows two distinct regions that correspond well with the experimental results. We can thus identify two environmental regimes for proton transport in NC in the measured environmental conditions, as shown in Figure 4-8:

a) $T \lessapprox 100$ ℃: proton generation and conduction is enabled through the surface physisorbed water layer; in dry conditions, or wet conditions but at temperatures above a threshold value of ≈30-60 °C, the physisorbed layer is thinner and therefore, the overall conduction is limited by the proton generation and transport rates.

b) 100 ℃ $\lessapprox T \lessapprox 135$ ℃: more protons are generated due to the increased electrochemical reactivity, and protons are conducted through the chemisorbed water, with possible catalytic support from oxygen vacancies.

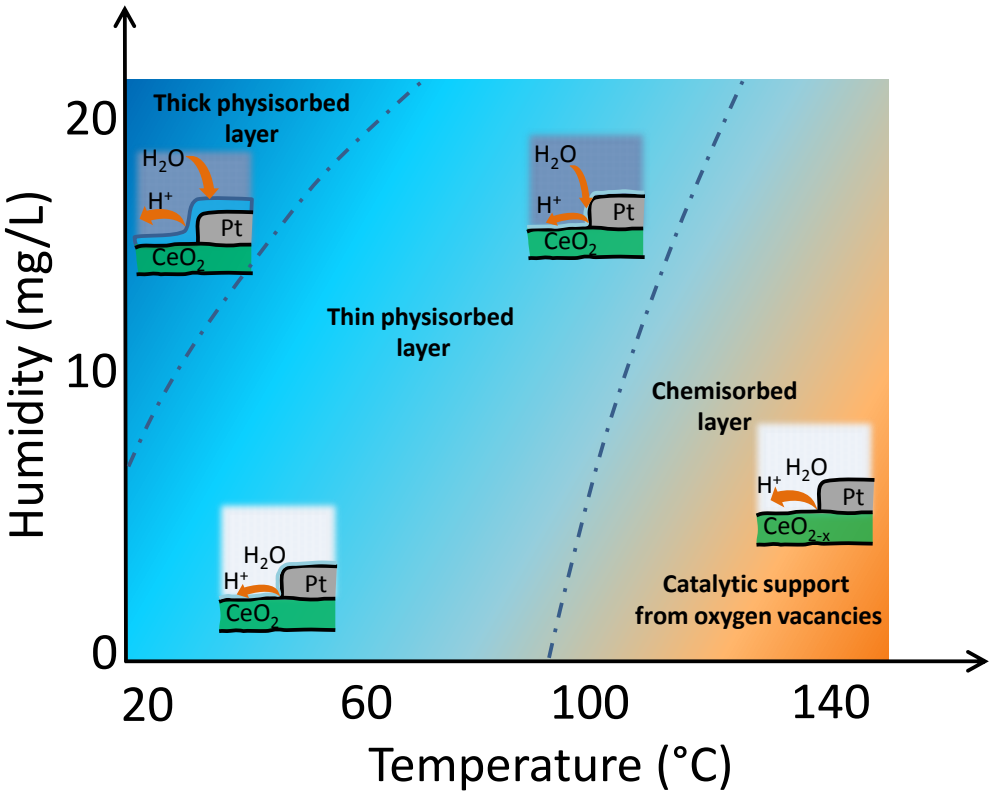

Figure 4-8 – Sketch of the environmental regimes for proton transport in NC in the measured environmental conditions.

CHAPTER 5. EFFECT OF MICROSTRUCTURE ON IONIC DYNAMICS OF NC

5.1 Introduction

Nanostructured ceria (NC), a mixed ionic-electronic conductor, has been widely studied as electrolyte in solid oxide fuel cells, catalytic devices, gas sensors, etc.[117, 186-188] Being a polar oxide, NC can strongly interact with the environment, e.g., with water vapor, which may significantly affect the materials properties during device operation.[105-107] In the previous two chapters, it is concluded that water can be physi- or chemi-sorbed on the NC surface. Under external electric field, water split into protons and/or hydroxyl groups (in addition to oxygen and hydrogen gas) that transport along the material. It is believed that the mechanisms of the water splitting and transport process are controlled by the nanoscale details of the NC structure.[29, 37] However, the direct correlation of the NC's microstructure with conduction properties is still under debate. For example, it is still debatable whether the proton conductivity occurs along the grain boundaries, residual pores and cracks, or along specific facets of the nano-crystals.[35-40]

In this chapter, energy discovery platforms were utilized to uncover the correlation between microstructure and the ionic conduction properties. Energy discovery platforms enable multiple characterization techniques on a single sample through a simple set-up, which can eliminate the data fluctuation originated from different samples used for different characterization methods: using same preparation method, two batches of samples are not necessarily identical in their microstructure, composition, etc. Here, time-resolved

Kelvin probe force microscopy (tr-KFPM) and electrochemical impedance spectroscopy (EIS) were employed to study the conductivity of NC under controlled environmental (temperature and humidity) conditions. EIS, with a well-established measurement and analysis procedure, is one of the most widely used techniques in electrochemical studies. However, it is often of a more limited scope at low temperatures, especially for thin films' characterization on the nanoscale, due to the relatively weak ionic conductivity in these conditions.[37] On the other hand, tr-KPFM detects the temporal- and spatial-resolved surface potential variation on the nanoscale, and can detect minute potential changes due to charge transport along the surface, when the flowing currents are below the detection limit of modern current amplifiers.[189] In recent years, tr-KPFM has been successfully used in studying surface transport phenomena in functional oxides, and it is believed to be an important supplementary technique for EIS due to its high resolution and sensitivity.[156, 158]

To understand the relationship between the NC microstructure and its electrochemical reactivity in different environmental conditions, thin films with different surface roughness, grain size and the crystallographic orientation were prepared through pulsed laser deposition, chemical solution deposition and sputter deposition. The preparation methods for different samples are shown in CHAPTER 2. The fundamental parameters for electrochemical reactions and transport phenomena were obtained through tr-KPFM and EIS measurement at controlled temperature and humidity conditions, and correlated to the microstructure. It was found that all the considered microstructure impact the conductivity in NC films, but their effects were dominant at different environmental conditions due to activation of different electrochemical processes.

5.2 Microstructure

The surface tomography and cross sectional images of all thin films were characterized by scanning electron microscopy (SEM), and are shown in Figure 5-1. They have similar thickness ranging from approximately 80 nm to 100 nm, and show good adhesion to the substrate, regardless of the preparation method. The microstructure of the films, however, is largely dependent on the preparation method and growth conditions. The films grown by PLD at 500 °C and 13.3 Pa (0.1 Torr) oxygen pressure (PLD500, Figure 5-1a and f) have an extremely rough surface, with grain size ranging from 20 to 50 nm. The films deposited by PLD at 700 °C and 13.3 Pa (0.1 Torr) O_2 (PLD700, Figure 5-1b and g) have lower surface roughness, and exhibit a smaller grain size. The PLD films deposited in a vacuum at 700 °C (PLD700HV, Figure 5-1c and h) have columnar grains, but a smother surface, albeit with cracks and pores connecting to the surface. The films prepared by CSD (Figure 5-1d and i) and SD (Figure 5-1e and j) have smaller grains, with an average grain size of about 10 nm. The surface tomography of each film was characterized by atom force microscopy (AFM), as shown in Figure 5-2. The surface roughness (R_g) from these images are calculated and summarized in Table 5-1. The PLD500 films have the highest surface roughness, ≈9.8 nm. The PLD700 and CSD films have lower surface roughness, ≈2.6 nm and 1.9 nm. The PLD700HV and SD films have the lowest surface roughness, ≈1.0 nm and 0.8 nm, respectively.

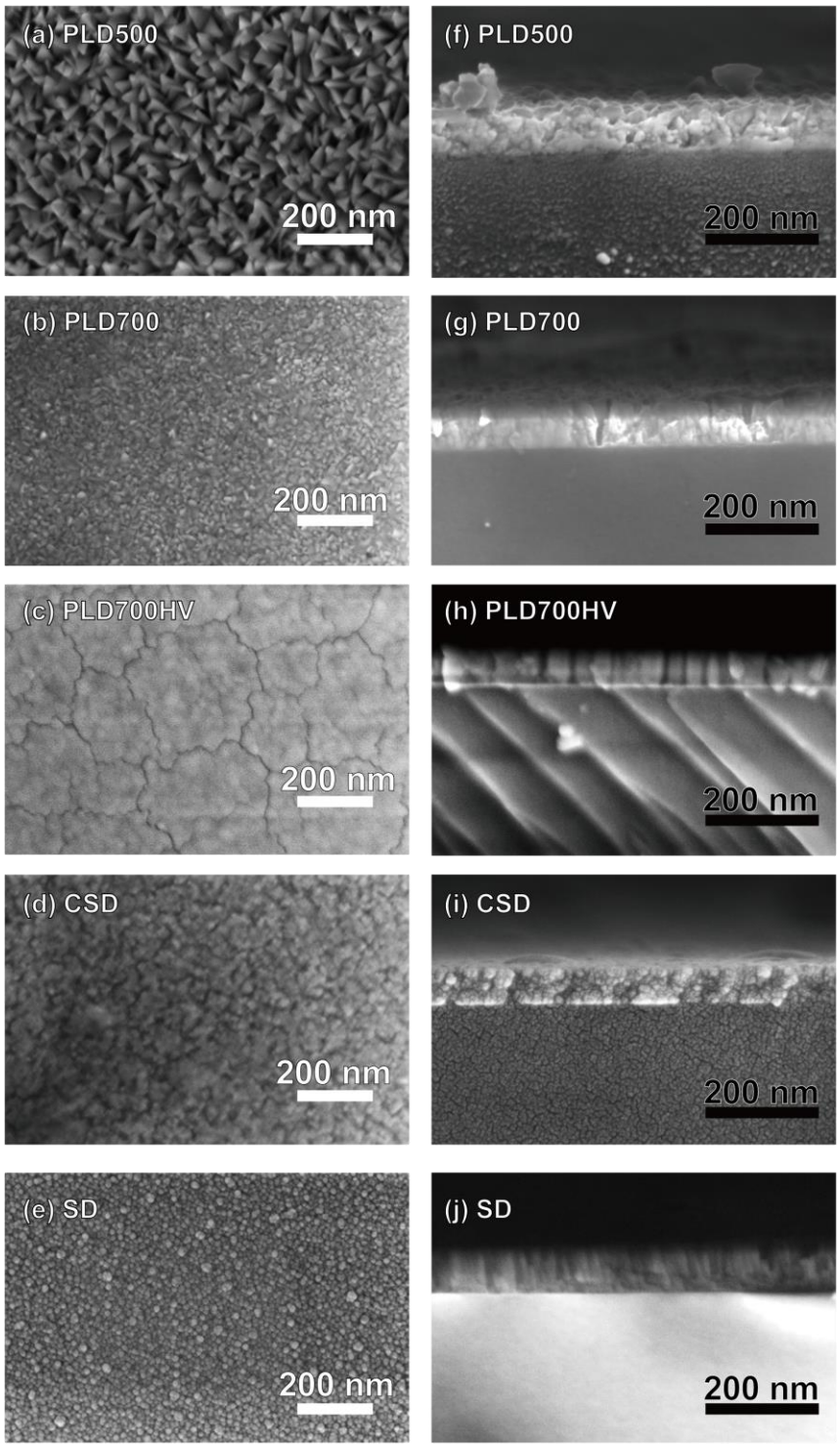

Figure 5-1 – Representative surface (a-e) and corss sectional (f-j) SEM images for PLD 500 (a, f), PLD 700 (b, g), PLD 700HV (c, h), CSD (d, i) and PLD (e, j) films.

Table 5-1 – Summary of surface roughness, grain size and Lotgering factor for {111} orientation for each of the films.

	PLD500	PLD700	PLD700HV	CSD	SD
Surface roughness R_g(nm)	9.8	2.6	1.0	1.9	0.8
Grain size (nm)	24 ± 2	41 ± 2	37 ± 3	14 ± 1	9 ± 1
Lotgering factor for {111}	0.06	-0.27	0.92	0.45	0.72

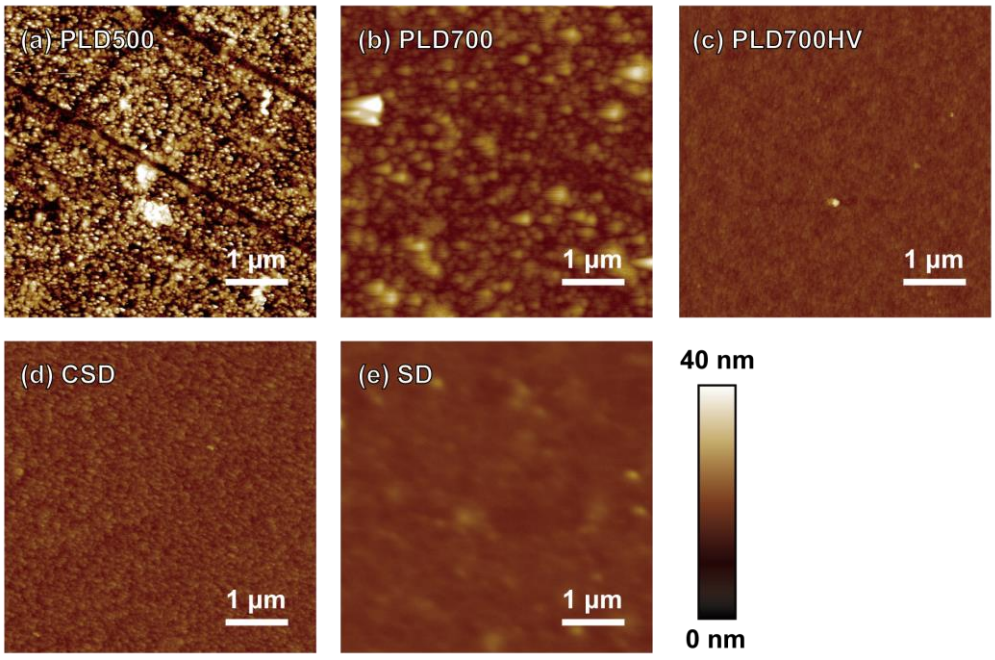

Figure 5-2 – Representative AFM images of nanostructured ceria thin films deposited by different deposition methods.

Figure 5-3 illustrates representative X-ray diffraction (XRD) patterns for thin films processed through different deposition methods. The patterns are compared with the Joint

Committee on Powder Diffraction Standards data of 34-0394, confirming the presence of polycrystalline ceria. The averaged grain size for each film is estimated from the Scherrer equation, $D = \frac{k\lambda}{\beta cos\theta}$ – where β is the full-width at half maximum (FWHM), k=0.9 is constant, λ is the wavelength of the X-ray radiation and θ is the Bragg angle – as reported in Table 5-1. The films deposited by PLD show shaper peaks, and the calculated grain sizes are approximately 24 nm ± 2 nm, 41 nm ± 2 nm and 37 nm ± 6 nm for PLD500, PLD700 and PLD700HV films, respectively. The films prepared by CSD and SD have much wider peaks, and the corresponding grain sizes are estimated at 14 nm ± 1 nm and 9 nm ± 1 nm, respectively. The calculated grain sizes have error bars that reflect one standard deviation from multiple XRD measurements, and are consistent with the SEM observation. To quantify the preferred crystallographic orientation of the samples, the Lotgering factors for {111} planes, $f_{\{111\}}$, were calculated based on the equation 47.[147, 148]

$$f = \frac{P - P^0}{1 - P^0}, where\ P = \frac{I_{\{111\}}}{\sum I_{\{hkl\}}} \tag{47}$$

where $I_{\{111\}}$ is the intensity (integrated peak intensity) of the {111} NC peak, $\sum I_{\{hkl\}}$ is the sums of the intensities of all of the NC peaks. P is for NC films being measured in this study, and P^0 is for the standard powder profile as reported in the PDF file. A Lotgering factor of 0 means that the crystals are randomly oriented, same as the standard powder. If Lotgering factor is higher than 0, the crystals are preferred along a certain orientation. As shown in Table 5-1, PLD700HV, SD, CSD and PLD500 samples has {111} preferred orientation, with $f_{\{111\}}$ being 0.92, 0.72, 0.45, and 0.06, respectively. PLD700 sample has

{110} preferred orientation, with $f_{\{110\}}$ being 0.21. However, for better understanding of the effect of {111} orientation, the $f_{\{111\}}$ is still calculated, which is -0.27.

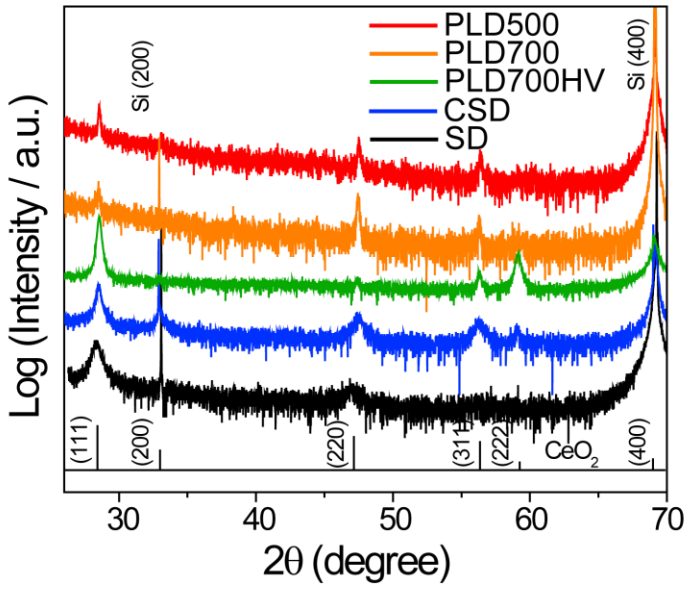

Figure 5-3 – XRD patterns for NC thin films prepared by different deposition methods.

5.3 Electrochemical Properties

The surface potential mappings of all the NC films at 25 °C and high humidity, and at 125 °C and in absence of humidity are shown in Figure 5-4. The former condition corresponds to conduction through the physisorbed water layer, while the latter require conduction facilitated by the chemisorbed water on the NC surface.[30, 38] At 25 °C and wet condition, PLD500 and PLD700 films (Figure 5-4a and b) exhibit strong changes in the surface potential over time throughout the whole NC surface. A large surface potential variation during polarization suggests that a considerable number of protons are injected at the biased electrode, and are transported towards the grounded electrode under the electric

field. Note, that the surface potential mapping at 60% rather that 90% is used for PLD500 film, because when RH is above 70%, the sample becomes so conductive that its resistivity is even smaller than the protective resistor (50 MΩ). Thus, the potential gradient over the sample is almost zero, and the tr-KPFM data is not comparable with other samples. In comparison, for CSD films (Figure 5-4d), the polarization and relaxation behavior is substantially weaker, and mostly concentrated in proximity to the biased electrode area. At the grounded electrode, the surface potential is mostly invariant over time, indicating that charge concentration does not significantly vary in this region. For PLD700HV and SD films (Figure 5-4c and e), the surface potential variation only exists in immediate proximity to the biased electrode, and is invariant in the rest of the film.

At 125 °C and dry condition, the CSD and SD thin films (Figure 5-4i and j) show the strongest surface potential variation during polarization and relaxation, indicating a high proton injection rate. PLD500 and PLD700 films (Figure 5-4f and g) have weaker response, and the potential variation is observed close to the biased electrode. PLD700HV film (Figure 5-4h) also have a relatively small potential variation, however, it spans over the whole surface, indicating a faster proton transport across the film.

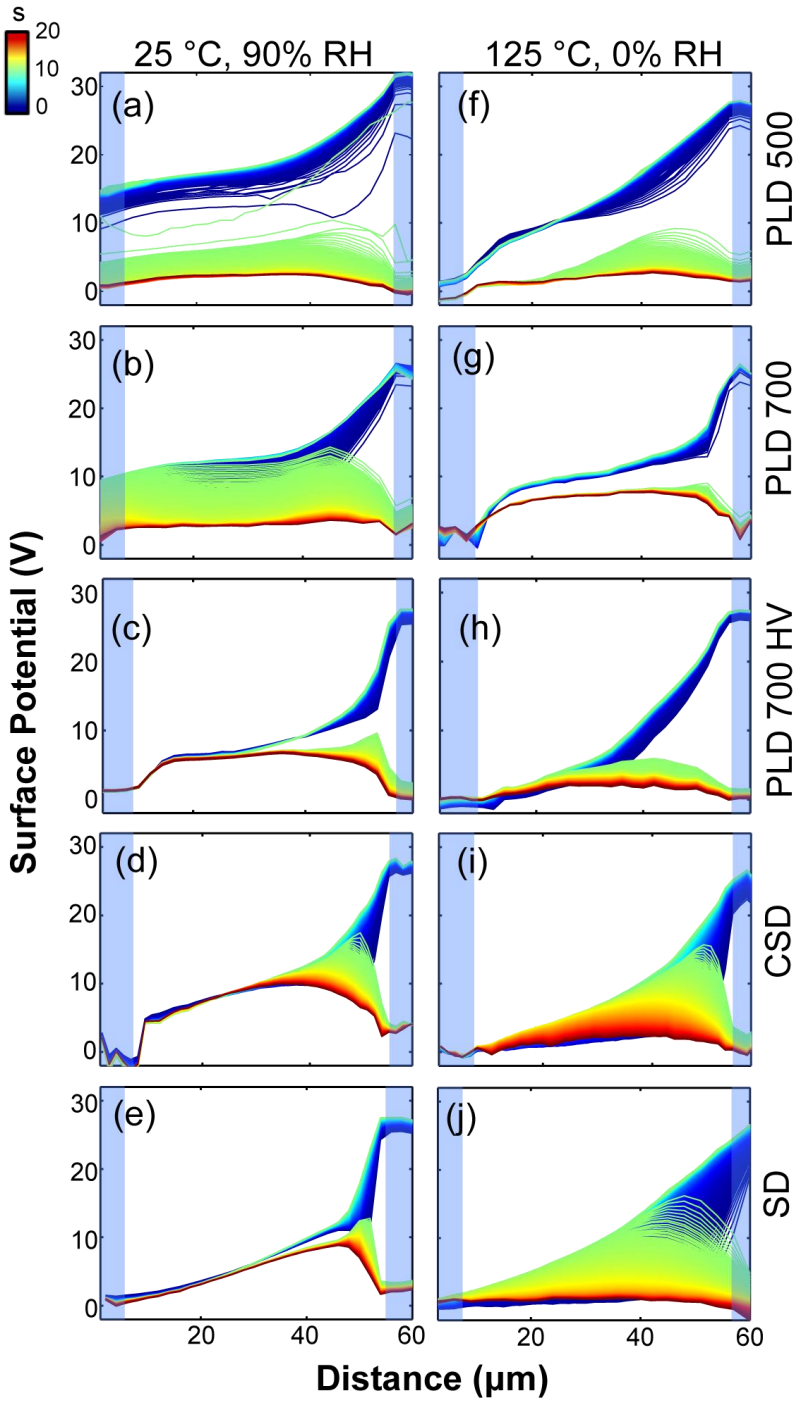

Figure 5-4 – Surface potential mapping as a function of time and distance for PLD500 films (a, f), PLD700 films (b, g), PLD700HV films (c, h), CSD films (d, i) and SD films (e, j) as measured at 25 °C and wet conditions (a-e) and 125 °C, 0% RH (f-j). The blue shaded areas correspond to the position of electrodes.

The DC current was also measured while obtaining each of the surface potential mappings, and is summarized in Table 5-2. At 25 °C and 90% RH, the interelectrode current is ≈170 nA and ≈2 nA for PLD700 film and CSD films, respectively, and is not detectable for PLD700HV and SD films. Because the resistivity of PLD500 films is much smaller than the protective resistor, the DC current through the sample cannot be accurately determined by the current settings. At 125 °C and dry condition, current is not detectable for any of the films and therefore not shown in the table.

As stated in the previous chapters, the observed surface potential variation over time is a result of two processes, i.e. proton generation at the biased electrode (Equation 35) and the subsequent proton transport toward grounded electrode under the electric field and chemical gradients. These physical processes can be expressed by Equation 48 and 49:

$$\frac{\partial n}{\partial t} = \nabla \cdot (-D\nabla n + \mu n \nabla \Phi) + (S - k_r n^2) \tag{48}$$

$$\nabla^2 \Phi = -\Sigma nF/\varepsilon_0 \varepsilon_r \tag{49}$$

where t is time, n is proton concentration, Φ is surface potential, D is diffusivity, μ is mobility, S is proton injection rate, and k_r is the reaction constant for proton dissipation. Compared with Equation 42 and 43, the physical model has been further simplified: according to the simulation performed in the previous chapter, the proton concentration in proximity to the biased electrode is on the order of 10^{-6} mol/L (Figure 4-2), which is over 100 times higher than the concentration of hydroxyl groups, according to Equation 36. Therefore, the effect of hydroxyl groups is neglected, and protons are assumed to be the

only charge carriers on NC. The last term in Equation 48 is also changed to $k_r n^2$ to better reflect the mechanisms of water splitting reactions (Equation 35). The rates of the forward and reverse reactions of Equation 35 are given by S and $k_r n^2$, respectively, where $S=k_f \cdot[H_2O]$ ($[H_2O]$ is water concentration on NC surface and k_f is the reaction constant for proton generation). We also assume that μ is linearly dependent on D according to the Nernst-Einstein relationship, and k_r is a constant for different samples at a specific temperature.

Table 5-2 – Summary of DC current, proton injection rate (S), proton diffusivity (D) and resistance (R_p) for NC films prepared via different methods.

		PLD500	PLD700	PLD700HV	CSD	SD
25 °C Wet	DC current @ 30 V (nA)	>600	170	$<1\cdot10^{-3}$	2.0	$<1\cdot10^{-3}$
	Proton injection rate (S) ($mmol/m^3s$)	>80	80 ± 20	10.0 ± 3.0	40 ± 6	5.0 ± 0.8
	Proton diffusivity (D) ($\mu m^2/s$)	>1000	1000 ± 250	5.0 ± 0.8	30 ± 8	2.0 ± 0.4
	Resistance R_F (Ω)	$5.0\cdot10^4$	$1.6\cdot10^8$	$>1.0\cdot10^{12}$	$1.9\cdot10^{10}$	$>1.0\cdot10^{12}$
125 °C Dry	Proton injection rate (S) ($mmol/m^3s$)	10 ± 1.0	3.0 ± 0.2	7.0 ± 1.5	35 ± 10	45 ± 10
	Proton diffusivity (D) ($\mu m^2/s$)	30 ± 5	10.0 ± 1.0	200 ± 30	60 ± 15	100 ± 20

To quantify the electrochemical behavior of each sample at different environmental conditions, finite element method was performed, similar to CHAPTER 4. The optimized parameters, S and D, were solved and summarized in Table 5-2. The S and D values of PLD500 films in 25 °C and 90% RH are too high to be accurately simulated, so they are

not available in the table. The detailed method for optimization of parameters and determination of fitting errors using the correlation coefficient is specified as follows:

1. For experimental data M of a certain sample, start with an arbitrary set of initial values, S_0, D_0, and k_{r_0}, solve FEM and obtain the simulated surface potential matrix, $N_0(t, d)$, and the correlation coefficient C_{M,N_0}.
2. Change D until the correlation coefficient is maximized.
3. With a fixed D, change S until the correlation coefficient is maximized.
4. With fixed D and S, find optimized k_r that gives largest $C_{M,N}$.
5. Reiterate the above three steps until the parameters stabilize.
6. Find the universally optimized k_r that gives the highest sum of correlation coefficient for all samples at a certain temperature.
7. Use this k_r and redo step 2 and 3 to re-optimize S and D values.

An example of the experimental and simulated surface potential changes (as compared to the initial stage of polarization or relaxation) is presented in Figure 5-5a and b, where the optimized $C_{M,N} = 0.93$. The optimized $C_{M,N}$ for each environmental condition varies, and is typically ranging from 0.92 to 0.95. To determine the errors bars of each fitting, a threshold of 0.90 of $C_{M,N}$ was set. By setting the optimized parameters in the simulation model, each time changing one parameter (S or D in this case), the upper and lower bound of each parameter can be determined when $C_{M,N}$ decreases below 0.90. Figure 5-5c-f shows the upper bound of S, lower bound of S, upper bound of D and lower bound of D, respectively. At these boundary values, the deviation of the potential mappings from the experimental data can be clearly seen: S mainly affects the "peak height", and D

mainly affects the "full-width at half maximum (FWHM)". Since the shape of the potential change mapping in Figure 5-5a is within the mappings in Figure 5-5c-f, the actual parameters are also considered between the upper and lower boundaries of *S* and *D*. This method was used to determine all the fitting errors in this study.

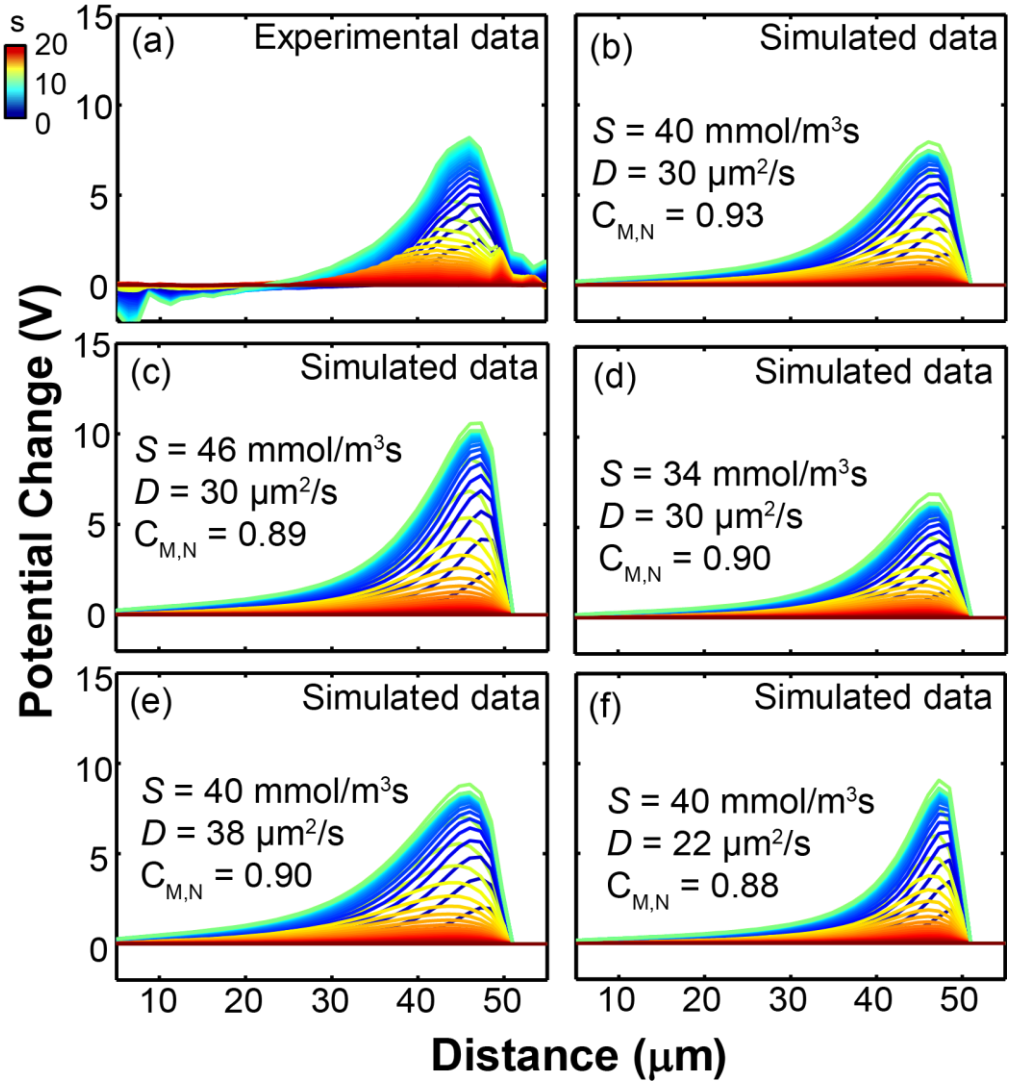

Figure 5-5 – (a) Experimental data of surface potential change as a function of distance and time for CSD thin films measured at 25 °C and 90% RH. (b) The corresponding simulated data that has the optimized parameter. (c-f) The simulated data that shows the upper and lower bound of parameters *S* and *D*. The simulation parameters and $C_{M,N}$ are included in each figure.

To further quantify the proton conduction behavior, electrochemical impedance spectroscopy is performed at a variety of RH values and 25 °C, as summarized in Figure 5-6. For all cases, the real part of impedance decreases with increasing sweeping frequency, so the direction of frequency sweep on the Cole-Cole plots are not marked on each plot. PLD500 films (Figure 5-6a), when RH is less than 50%, the Cole-Cole plot shows a semicircular shape, indicating that the device can be described by the Randles equivalent circuit as shown in Figure 5-6d.[190, 191] In this circuit, R_S correspond to a series resistance, such as the contact resistance between Pt and film; R_F and C_F are the resistance and capacitance of the film. At higher RH, a linear tail appears at lower frequencies accompanied by a significant decrease of the semicircular part. The Warburg impedance element, Z_w is added in series with R_F to the equivalent circuit, as shown in Figure 5-6e, which represents the involvement of semi-infinite diffusion of protons at the NC-electrode interface. The linear tail is not seen in PLD700 and CSD films (Figure 5-6b and c), possibly due to the limited water layer on the NC surface: the equivalent circuit is represented by Figure 5-6d. The impedance spectra for PLD700HV and SD films are not shown in this study, because their impedance is too high to be measured (note, again, that despite high impedance, tr-KPFM allows probing their transport properties). The EIS plots are fitted to the proposed equivalent circuits and the resistivity R_F are plotted as a function of RH, as shown in Figure 5f. At the same RH, PLD500 films have the lowest resistivity and CSD films have the highest resistivity. For all films, R_F decreases with increasing humidity, which is consistent with proton conduction within the physisorbed layer. The R_F value at 25 °C and RH of 90% is also summarized in Table 2. The R_F is $5.0 \cdot 10^4$ Ω, $1.6 \cdot 10^8$ Ω and $1.9 \cdot 10^{10}$ Ω, respectively. The high sensitivity to humidity makes these films good

candidates for H_2O sensors. And by controlling the microstructure through different deposition methods and parameters, the resistivity range can also be controlled as needed. It is worth noting that EIS measurements at 125 °C and in absence of humidity showed almost purely capacitive signal originated from the substrate instead of proton transport on NC films, and no DC current between electrodes was detectable.

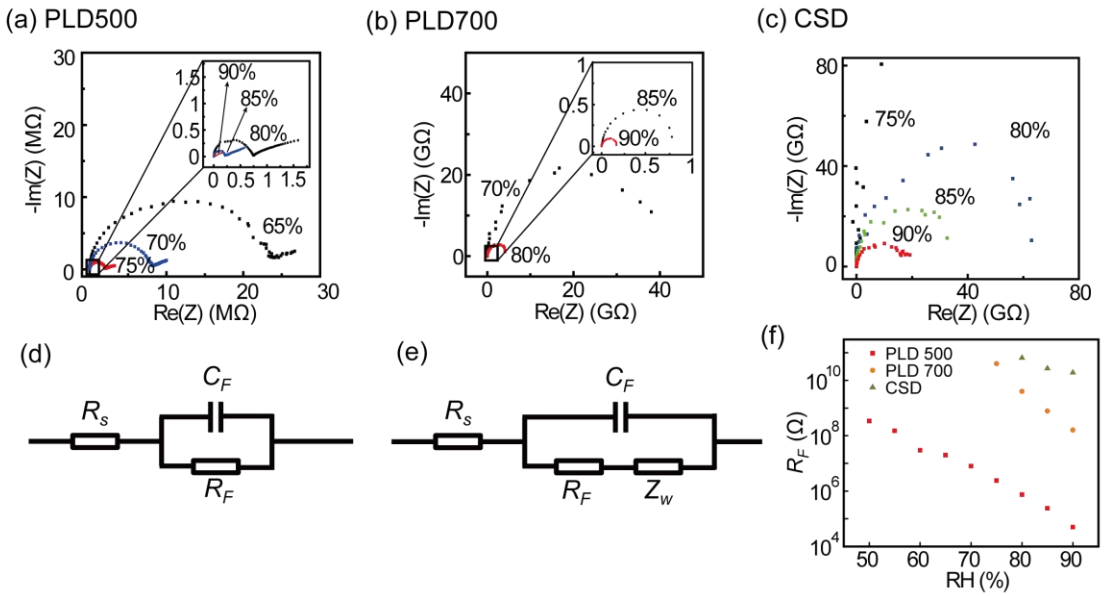

Figure 5-6 – Impedance spectra of (a) PLD500, (b) PLD700 and (c) CSD films at various humidity at 25 °C; (d-e) equivalent circuits of NC thin films; (f) Resistance (R_p) as a function of humidity for different NC thin films.

5.4 Effect of Surface Roughness and Grain Boundaries

The correlation between the fitting parameters (S and D) and microstructure, including surface roughness, grain size and $f_{\{111\}}$, is studied according to the data provided in Table 5-1 and Table 5-2, as plotted in Figure 5-7. For the case of comparison, all graphs are plotted using the same scale for all vertical axis. It is clearly seen that at 25 °C and 90% RH (Figure 5-7a-c), the change of S and D for different samples is substantially larger than

at 125 °C and 0% RH (Figure 5-7d-f), which indicates a crucial role of the relatively thick physisorbed water layer in the former conditions, as elaborated in the following discussion.

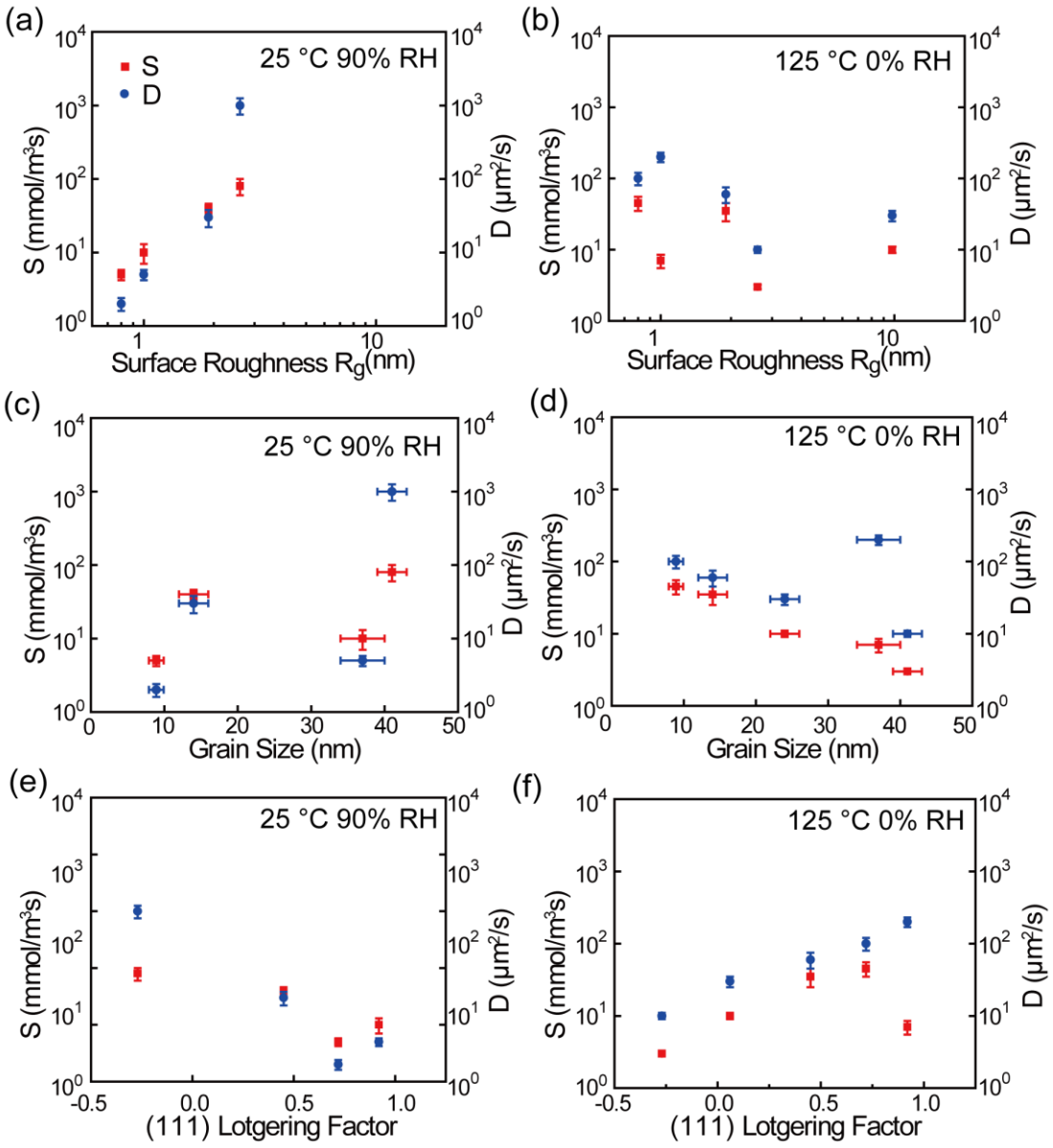

Figure 5-7 – Fitting parameters (*S* and *D*) as a function of surface roughness (a, b), grain size (c, d) and {111} Lotgering factor (e, f) at 25 °C and 90% RH (a, c, e) and 125 °C and 0% RH (b, d, f).

5.4.1 Effects of Surface Tomography

The correlation between the surface roughness and proton injection rate, *S*, and proton diffusivity, *D*, for each of the samples are plotted in both environmental conditions, as shown in Figure 5-7a and b. At 25 °C and high humidity condition, both parameters are positively correlated with the surface roughness (Figure 5-7a). However, at 125 °C and dry condition, these parameters have no significant correlation with the surface roughness (Figure 5-7b).

The positive correlation between surface roughness and *S* and *D* at room temperature is mostly likely a result of the water layer formed on the NC surface. A rough surface provides more porous and capillary-filled regions, resulting in a larger amount of condensed water in contact with the sample. Under an applied electric field, water molecules are decomposed (Equation 35), generating protons that transport through this water layer. As previously stated, the proton generation rate *S* is equal to $k_f \cdot [H_2O]$. While k_f is considered constant and relatively small at low temperature, $[H_2O]$ is largely dependent on the surface tomography of the sample. More water is overall adsorbed on the surface – and specifically of interest, at the Pt-NC interfaces – in the samples with higher surface roughness (PLD500, PLD700 and CSD). Therefore, the electric field-induced water splitting generates more protons in the samples, resulting in a relatively high *S* (Table 5-2). For PLD700HV and SD films, however, due to the low surface roughness and therefore limited amount of adsorbed water, *S* is much smaller, resulting in much smaller changes in the surface potential.

Proton diffusivity, *D*, follows overall the same trends in microstructural dependence as *S*, since *D* is expected to increase within a larger volume of adsorbed water layer on NC surface. When liquid water is formed on the surface, protons can be

transported through multiple pathways including water and water-NC interface, resulting in a larger *D* than that of samples with smaller amount of surface water, and thus limited proton pathways. For samples with lower surface roughness, since the condensed water is much thinner, the conduction pathways for protons are also limited. Therefore, *D* is also considered a qualitative measure of the thickness of water on the surface.[108] The obtained *D* value is consistent with DC current and resistance R_F: with increasing *D*, the inter-electrode current also increases, and the resistance between electrodes decreases, as shown in Table 5-2. At higher T, water is mostly evaporated from the surface, so the surface diffusion of protons is less important. That is why no correlation between surface roughness and *D* is observed. However, other conduction pathways may exist in these conditions, as discussed in the following section.

5.4.2 Effects of Crystal Size and Orientation

To further study the effects of crystallinity on the ionic dynamics in NC, the fitting parameters, *S* and *D*, are also plotted as a function of grain size and $f_{\{111\}}$ for both environmental conditions studied, as shown in Figure 5-7c-f. At 25 °C and 90% RH, no obvious correlation between crystallinity and fitting parameters are observed (Figure 5-7c and e), since *S* and *D* are mostly determined by the physisorbed surface water formed on the NC, providing the primary conduction path. However, at elevated temperatures, the proton injection rate *S* decreases with increasing grain size (Figure 5-7d): the water layer on NC surface and connected pores have mostly evaporated, leaving only chemisorbed water that dominates the electrochemical reactivity.[185] Such layer does not necessarily exist only on the surface, but can be present also at the grain boundaries within NC.[36, 38] Here, the total amount of chemisorbed water is proportional to the area of grain boundaries. So

$S=k\cdot[H_2O]=k'\cdot A$, where A is the grain boundary area at the reaction site (close to the Pt/NC interface), and is inversely proportional to the grain size, as observed experimentally.

In contrast, the proton diffusivity does not have a clear correlation with grain size at 125 °C and 0% RH, as is shown in Figure 5-7d. The "outlier", PLD700HV sample, has the highest D. Admittedly, the remaining four samples appear to exhibit a negative correlation between D and grain size; however, considering the "outlier" and the fact that D does not depend on the area of grain boundaries according to the definition of diffusivity, D might have a more direct correlation with other factors instead of grain size. The exceptionally high diffusivity observed in PLD700HV sample might be due to an addition of water diffusion pathways through large and deep cracks in this sample, as observed in Figure 5-1c. Furthermore, most of the protons are expected to exhibit hopping transport in the first water molecules layer that is chemisorbed on the NC surface lattice, according to the Grotthuss mechanism (Equation 41).[7, 30, 179, 185] The overall diffusivity can also be affected by the interaction between water and the NC surface termination. Indeed, according to Figure 5-7f, a positive correlation between D and $f_{\{111\}}$ is observed, suggesting the dependence of surface crystal orientation on proton diffusion in NC.

The ceria {111} surface is known to be the most stable surface among the low index surfaces of ceria, and strong water adsorption to ceria {111} plane has been observed experimentally.[192, 193] Such adsorption can be in the form of molecular, dissociative or a mixture of both,[105-107] but the properties of each crystallographic orientation such as water coverage and defect concentration is unknown. Due to this complexity, direct comparison of the water-ceria interaction of different surface orientation has been limited and contradictory.[194] However, two possible reasons for the positive correlation of $f_{\{111\}}$ and D

can be identified: first, water adsorption on ceria surface is energetically favorable, and water is bonded more strongly to {100} and {110} than to {111} oriented surface, due to lower adsorption energies for water association.[106] It is true that weaker water adsorption energy on {111} surface may result in a poor water layer continuity and thus decrease the value of *D*; however, since water adsorption is energetically favorable on all surfaces,[106] we assume that chemisorbed water is well dispersed onto ceria, and any variation in *D* value due to water discontinuity is a minor factor. On the other hand, protons can move more freely along the surfaces with lower adsorption energy, i.e. {111}, resulting in a higher *D* than other crystallographic planes. Second, due to the close packing on {111} surface in the fluorite-structured ceria, the distance between a proton (from adsorbed water, either associative or dissociative) and its nearest oxygen atom is smaller than in other crystallographic planes.[106] According to Equation 41, proton transport is enabled through Grotthuss mechanism, and a smaller proton-oxygen distance is expected to result in a lower proton hopping energy barrier, thus leading to a higher *D* value for ceria {111} surface.

As a result, within the exposed surfaces, the {111} planes might allow for higher proton diffusivity, while addition of cracks and open pores resulting in increased pathways for water and proton diffusion could also have similar effects. However, further investigation is needed to systematically understand the correlation between proton diffusivity and specific crystallographic surfaces.

5.5 Conclusions

In this chapter, five NC thin films with different microstructure were prepared by PLD, CSD and SD, and the effects of their microstructure on electrochemical reactivity

and proton conductivity at temperatures below 200 °C are studied. The PLD films deposited at oxygen atmosphere have the highest surface roughness and large grain size. The PLD films deposited at high vacuum, however, have smooth surface and large grain size, and are highly {111} oriented. The thin films prepared by CSD and SD have relatively low surface roughness, and the grain sizes are much smaller, with a {111} preferred orientation. The parameters for proton generation and transport were obtained from the surface potential mappings of tr-KPFM and EIS. It is found that the surface roughness is positively correlated with the proton generation and conductivity at 25 °C and 90% RH, most probably due to the proton transport through water layer condensed on the NC surface. In contrast, at elevated temperature (125 °C) and dry conditions, when the surface physisorbed water evaporates, the ionic dynamics are mainly dependent on the grain size and crystallographic orientation. The proton generation rate is negatively proportional to the gran size, while the proton transport though chemisorbed water is mainly affected by the surface plane orientation and the cracks and open pores connecting to the surface. The proton diffusivity is positively correlated with the Lotgering factor of {111} plane, most possibly due to the ease of proton transport along {111} oriented NC surfaces.

CHAPTER 6. IONIC DYNAMICS STUDY OF GRAIN-BOUNDARY-FREE Y-BZO

6.1 Introduction

Optimizing proton conduction in solids remains the most promising solution for achieving intermediate temperature (≈500-700 °C) SOFC devices, electrochemical gas sensors, and enabling selective membranes for H_2 separation.[6, 195-197] Proton conducting perovskites are a promising class of materials for these applications, due to relatively low expected activation energy for proton conduction.[7] As introduced in the first chapter, the ionic transport is quantified by ionic conductivity (σ) which is written as $\sigma = nze\mu$, where 'n' is the density of free carriers with charge 'ze' and mobility $\mu = \mu_0 exp(-\frac{E_a}{kT})$, where E_a is the activation barrier for proton transport.

Among different proton conducting perovskites, yttrium doped barium zirconate (Y-BZO) shows the highest conductivity of all known materials, with an optimized dopant concentration at 20%.[198] In Y-BZO, extended defects such as grain boundaries and dislocations further impede proton transport and increase the activation energy, and as such polycrystalline samples show an activation energy higher than 0.7 eV.[33, 119, 140, 199-201] These defects have typically generated a wide variability in their measured conductivity values,[33, 199] which have hindered a fundamental mechanistic understanding of how (acceptor) doping levels correlate with the activation energy of protons to produce an optimal doping level for fast proton transport.

Beyond these microstructural effects, it is widely accepted that protons bind more strongly to the acceptor dopant, due to its intrinsic negative charge, and this binding can adversely affect proton conductivity.[202] Indeed, over a wide range of possible acceptor dopants, the Y-dopant was shown to have the lowest activation energy (i.e. highest mobility) for protons in BZO, as other dopants bind protons too strongly to allow fast ionic conduction.[203] Very early works have indicated that this binding could be due to the presence of localized bound polarons[204-206] due to local lattice relaxations to screen the charged defect, but they do not give any specific information on chemical interactions, the nature of the polaron and how it couples to the conducting protons, as pointed out by K. D. Kreuer.[16] The role of local relaxations have also been found in undoped BZO, confounding this matter.[207] Calorimetry measurements on powder samples obtain negative enthalpy of mixing even up to 50% of Y in BZO, but it starts to level off beyond 30%, suggesting that some type of defects cluster at these concentrations[208]. But the connection is not clear between the spatial distribution of dopants as a function of doping level, the proton binding energy, and the mobility of the protons through the material.

In this chapter, the origin of proton conduction in the Y-BZO was explored in a systematically range of dopant concentrations: 0, 5, 10, 15 and 20% (0, 5, 10, 15 and 20Y-BZO). To ensure the minimal extended defects, PLD was used to epitaxially grow Y-BZO thin films on (100) oriented MgO substrates as previously demonstrated.[33] The results from grain-boundary-free stoichiometric thin-films and dense polycrystalline films were also compared. The structural characterization via STEM and proton transport characterization dynamics via tr-KPFM were combined to illustrate the correlation between the activation energy and lattice distortion.

6.2 Structural Characterization

The crystal structure of Y-BZO films was characterized by XRD. Figure 6-1 presents the XRD patterns for both epitaxial and polycrystalline Y-BZO films with different dopant concentrations.

All of the patterns show peaks corresponding to the BZO perovskite structure (JCPDS 00-006-0399). In epitaxial thin films (Figure 6-1a-e), only peaks corresponding to (100) orientation was observed, indicating that the deposited films are epitaxial along (100) direction. No peak relative to a second phase was observed. For polycrystalline films (Figure 6-1f), multiple peaks were observed for each dopant concentration, indicating different crystal orientation of the grains.

The "in-plane" crystalline structure of the epitaxial Y-BZO thin films were investigated by φ-scan via XRD. Figure 6-2 presents a representative φ -scan measurements towards the (111) asymmetric reflection on epitaxial 20Y-BZO sample, revealing the biaxially textured structure.

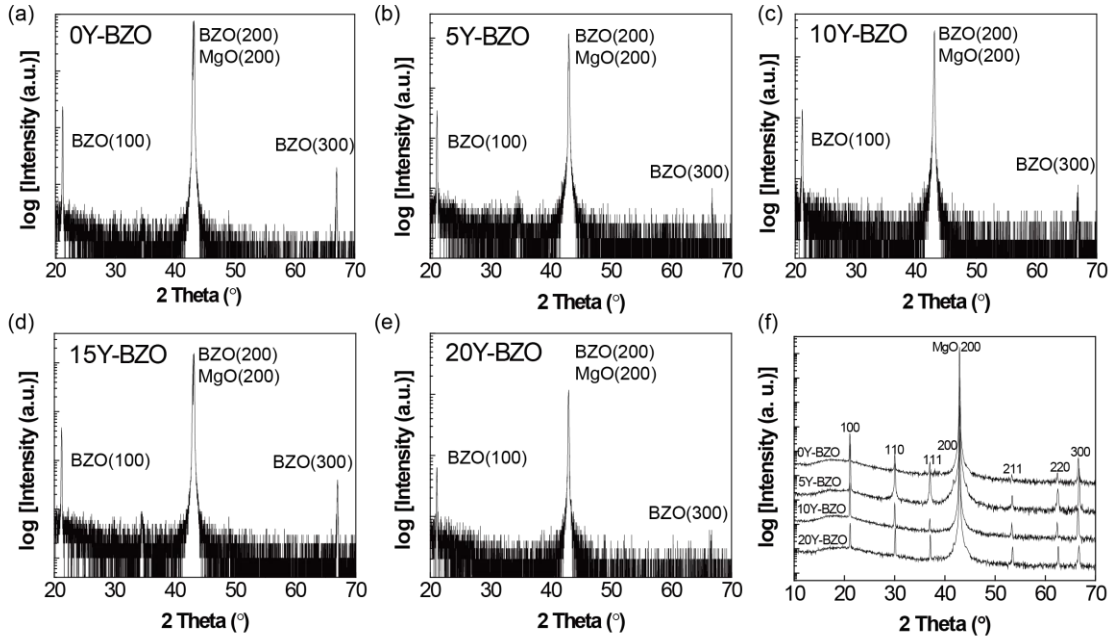

Figure 6-1 – XRD patterns for epitaxial (a-e) and polycrystalline (f) Y-BZO samples with different dopant concentrations.

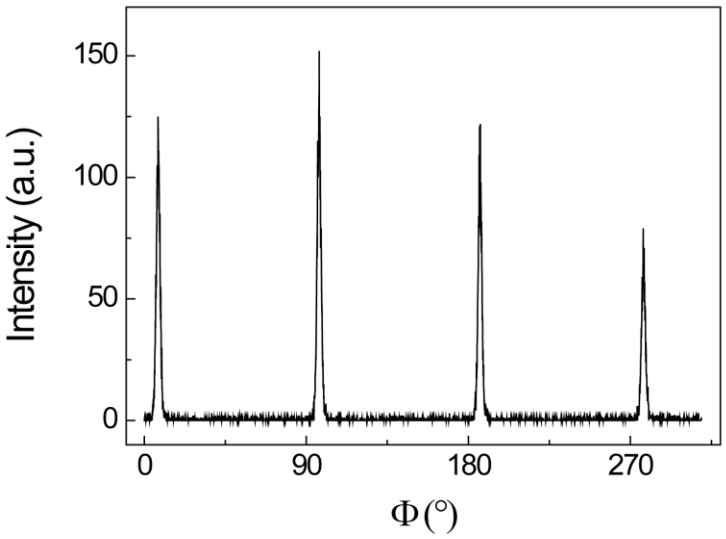

Figure 6-2 – Representative φ scan of the epitaxial 20Y-BZO thin films, showing a textured structure.

The surface tomography of Y-BZO thin films were characterized by AFM. They all show a rather smooth surface, with surface roughness (R_g) being less than 1 nm. As an example, the AFM surface tomography of epitaxial 20Y-BZO is shown in Figure 6-3. The surface roughness is calculated to be 0.3 nm.

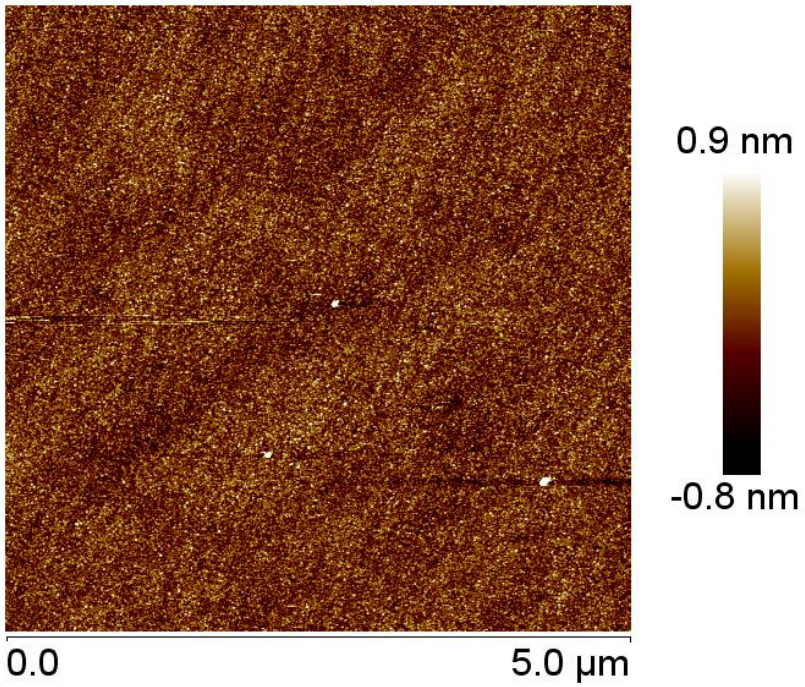

Figure 6-3 – Representative AFM tomography of epitaxial 20Y-BZO.

The atomic resolution images of Y-BZO epitaxial thin films at different dopant concentrations were obtained through STEM, as shown in Figure 6-4. It is confirmed that these films are highly (100) oriented without any secondary phases. The lattice constant was calculated to be about 4.2 Å, consistent with the data from literature (a=4.209 Å).

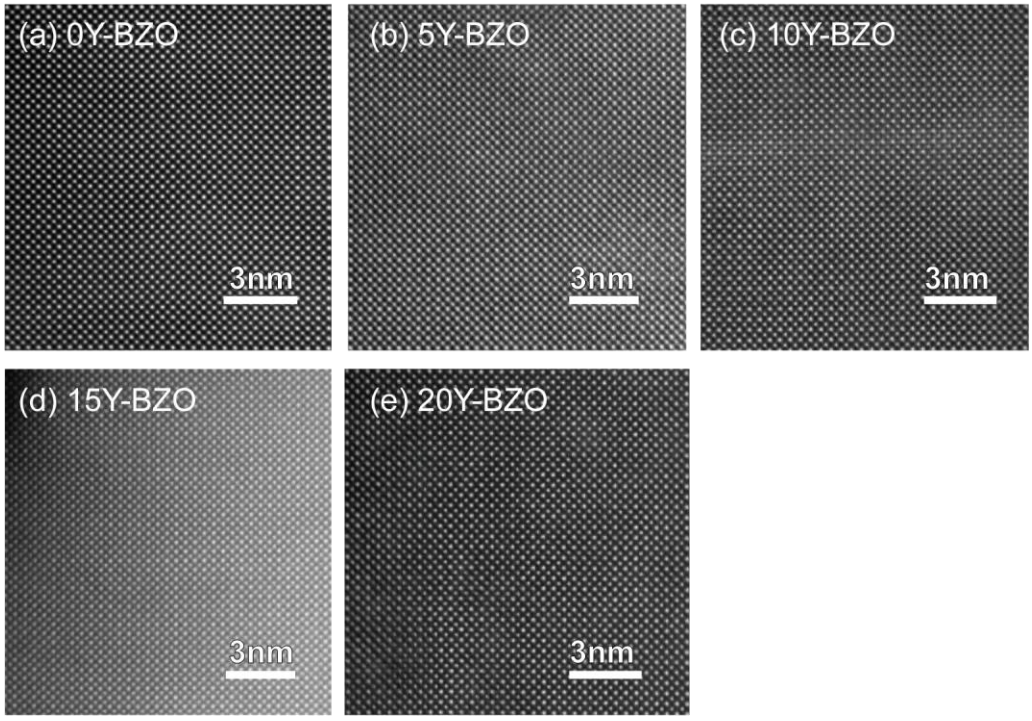

Figure 6-4 – Representative STEM images for epitaxial 0, 5, 10, 15 and 20Y-BZO samples.

6.3 Transport Phenomena

6.3.1 Conducting Species and Pathways

Tr-KPFM was utilized for transport mechanism studies on Y-BZO samples. To identify the conducting species on the Y-BZO thin films, the effect of humidity on surface potential profiles was first investigated. 5Y-BZO polycrystalline sample was measured at 140 °C in both 0% RH and 90% RH conditions, as shown in Figure 6-5. In Figure 6-5a, the sample is measured within 1 hour of exposing the sample to dry air, where the surface potential profile does not differ a lot from the one measured at 90% RH (Figure 6-5b). However, the polarization and relaxation gradually becomes weaker and finally disappears after 2 days' baking at 140 °C in dry atmosphere (Figure 6-5c). When the sample is

measured again in high humidity atmosphere, the polarization and relaxation is not recovered until several days later. This phenomenon suggests a crucial role of atmospheric water on the electrochemical reaction in Y-BZO sample. During polarization (dark blue to light blue curve), water molecules from the ambient are expected to dissociate at the triple phase boundaries (TPBs), generating protons, electrons and oxygen molecules under the electric filed (Equation 35). Protons are then accumulated in the film, and are the most probably charge carriers that cause the potential variation. The excess protons migrate toward the grounded electrode under the electric field, resulting in the increase of potential in proximity to the biased electrode. During the bias-off stage (green to red curve), the accumulated protons gradually dissipate and migrate toward the two electrodes, as evidenced by the potential profile leveling down.

The observed surface potential trend in Y-BZO are somewhat similar to that in NC: they show an increase in surface potential during polarization in proximity to the bias electrode, and a drop in surface potential during relaxation. However, the Y-BZO sample responds to the humidity much more slowly. The reason for this may come from the fact that in Y-BZO, protons are mostly conducted through the bulk lattice instead of along the surface water, which exhibits higher activation energy (>0.5 eV).[7] The protons are in the interstitials of the lattices, and have strong interaction with the cations. Therefore, it is more difficult for the protons to be evaporated from the lattice, due to a rather strong bonding between protons and the adjacent oxygen lattice. And this explains the lower sensitivity towards humidity in Y-BZO samples. In order for protons to be substantially driven out of the lattice, high operating temperature and/or long time is needed.

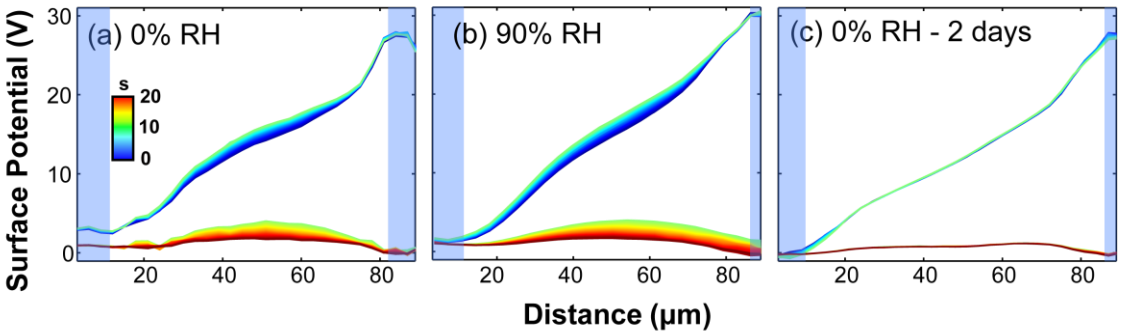

Figure 6-5 – Surface potential profiles as a function of distance and time on 5Y-BZO polycrystalline samples measured at 140 °C and (a) 0% RH; (b) 90% RH; (c) 0% RH baking for 2 days. The blue shaded areas correspond to the position of electrodes.

To further demonstrate the assumption that protons in Y-BZO are mostly in the lattice instead of on the surface, tr-KPFM measurement is also done on the same sample at 25 °C and 90% RH, as shown in Figure 6-6. If thick physisorbed water layer is condensed on the surface of Y-BZO, protons are expected to freely move, causing severe surface potential change, as indicated in CHAPTER 5. However, the observed surface potential does not change over time. Therefore, the surface proton conduction pathways in Y-BZO are likely to be limited.

To sum up, the ionic dynamics observed on Y-BZO samples are most probably result from proton transport, and the protons are assumed to conduct along the crystal bulk as interstitials. To ensure a proper amount of protons present in the lattice, it is necessary to maintain water source from the ambient, therefore the rest of the tr-KPFM measurements in this study were done at wet conditions (>90% RH as measured at 25 °C). To understand the proton conduction mechanisms in Y-BZO, tr-KPFM measurements are further performed at higher temperatures, where surface potential variation is stronger.

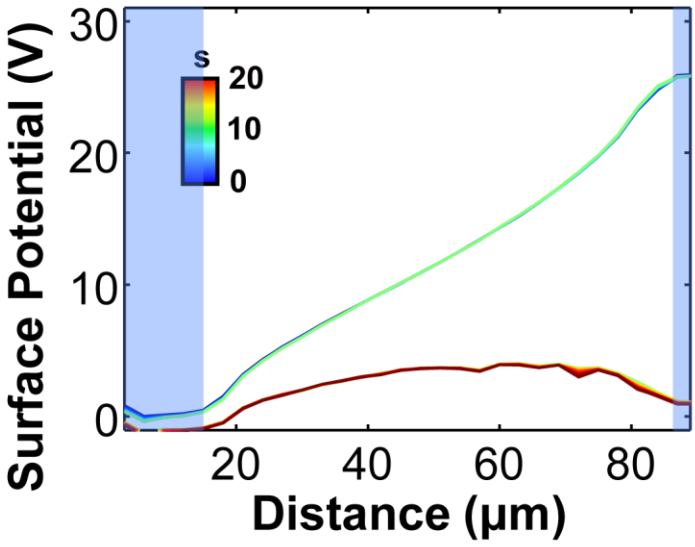

Figure 6-6 – Surface potential profiles as a function of distance and time for polycrystalline 5Y-BZO measured at 25 °C and 90% RH. The blue shaded areas correspond to the position of electrodes.

6.3.2 Transport Mechanisms Study

Figure 6-7 shows the representative surface potential mapping on polycrystalline 5Y-BZO and 20Y-BZO films at various temperatures as a function of distance and time. The potential variation over time becomes appreciable at above 100 °C, suggesting that proton generation reaction and proton migration begin to take place at this temperature range. At such temperatures, during polarization, the potential profiles gradually level up due to the accumulation of protons in the lattice. Water is continuously injected into the lattice, generating protons that accumulate in the interstitials of the lattice, resulting in an increase of surface potential. Any other possible contribution to the surface potential value such as the defects created by Y doping are considered static, and therefore does not contribute to the potential variation. During the relaxation stage, the accumulated protons gradually dissipate and result in a decrease of surface potential.

The higher temperature increases electrochemical reactivity of water splitting reaction, therefore more protons are generated and accumulated in the material, resulting in higher potential variation. With higher yttrium concentration, more oxygen vacancies are formed, according to Equation 17. Water from the gas phase dissociates into a hydroxide ion and a proton. The hydroxide ion fills an oxygen vacancy and the proton forms a covalent bond with lattice oxygen, as shown in Equation 18. Therefore, higher dopant concentration results in an increase in proton concentration in the lattice, and thus a stronger potential variation.

The inter-electrode current was measured by an ampere meter while obtaining surface potential mappings. For all samples and measurement conditions, the measured inter-electrode current is lower than the sensitivity of the instrument (<3 pA), suggesting a very limited conductivity at temperature below 200 ºC ($R>10^{13}$ ohm). The inter-electrode current for 20Y-BZO is plotted in Figure 6-8, representative for all dopant concentrations studied. This demonstrates that tr-KPFM is able to detect ionic transport even below the limitation of normal impedance measurement.

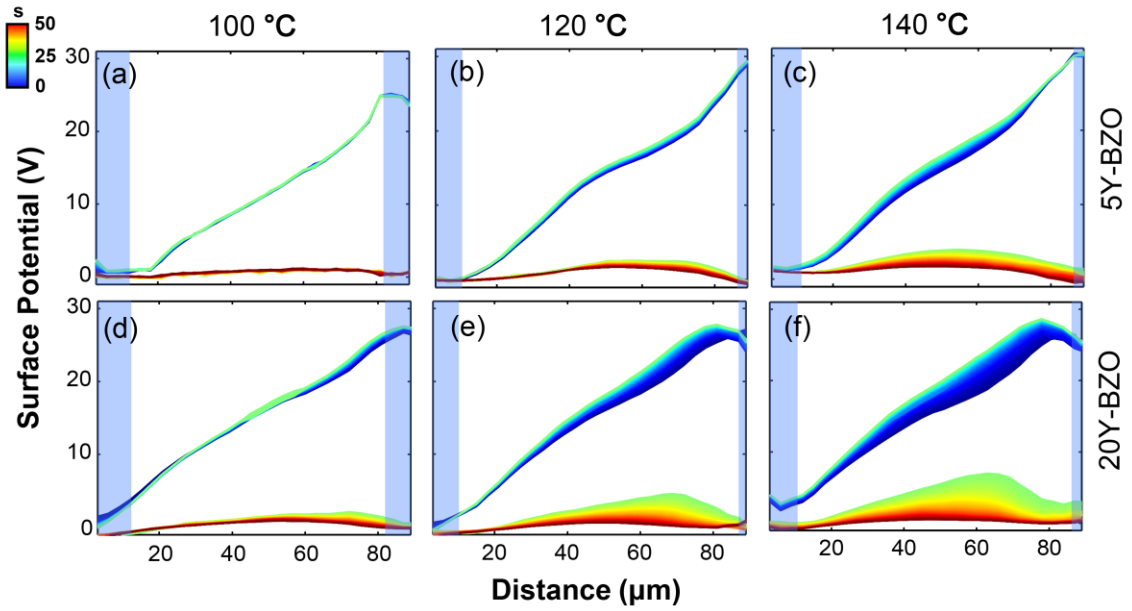

Figure 6-7 – Surface potential profiles as a function of distance and time for polycrystalline 5%Y-BZO (a-c) and 20% Y-BZO (d-f) at varying temperatures: (a) (d) 100 °C, (b) (e) 120 °C and (c) (f) 140 °C. The blue shaded areas correspond to the position of electrodes.

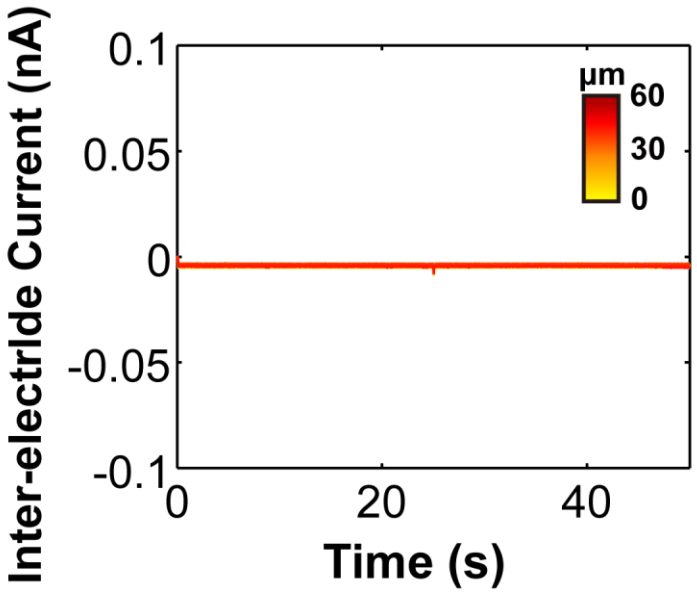

Figure 6-8 – Inter-electrode current evolution over time as a function of distance measured on 20Y-BZO sample, representative for all dopant concentration samples.

The same tr-KPFM measurements were also performed on epitaxial Y-BZO thin films, and the representative surface potential mappings on epitaxial 5Y-BZO and 20Y-BZO samples as a function of distance and time are presented in Figure 6-9. The surface potential behaves similarly to the polycrystalline sample; however, they show a much faster potential variation, and this phenomenon is consistent with the blocking effect by the grain boundaries in polycrystalline Y-BZO. In epitaxial films, protons are transported more freely, and therefore the surface potential changes faster than the sample with grain boundaries.

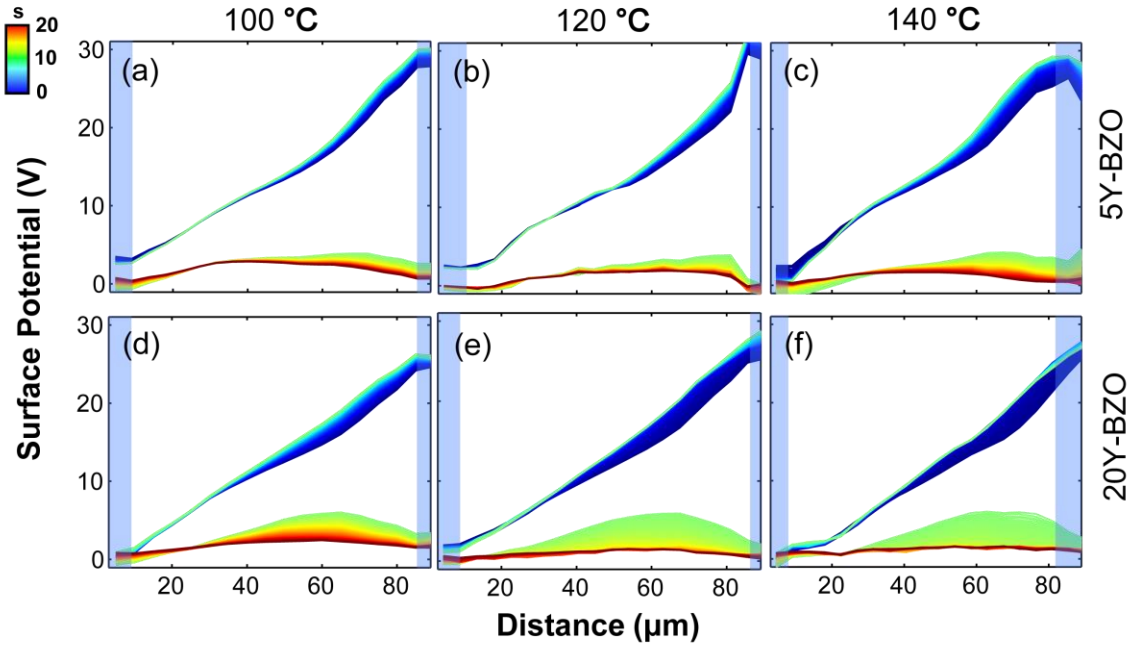

Figure 6-9 – Surface potential profiles as a function of distance and time for epitaxial 5%Y-BZO (a-c) and 20% Y-BZO (d-f) at varying temperatures: (a) (d) 100 °C, (b) (e) 120 °C and (c) (f) 140 °C. The blue shaded areas correspond to the position of electrodes.

The surface potential behavior of these samples was further quantified by exponential fitting, same as the analysis done for NC samples (Equation 34). The time

constants were obtained for each surface potential mapping, and the Arrhenius plots of the time constant as a function of Y concentration and microstructure (epitaxial films as well as polycrystalline films) are plotted in Figure 6-10a. The activation energy for proton transport of each sample is then calculated from the slope of the Arrhenius plot, as plotted in Figure 6-10b. At the same dopant level, the activation energy for polycrystalline Y-BZO is higher than that of the epitaxial Y-BZO. This is consistent with many of the previous studies, where the proton transport through grain boundaries shows much higher activation energy. Measurements on the epitaxial Y-BZO films show an activation energy of 0.64 eV at 20% Y-doping, which is in good agreement with the activation energy of 0.63 eV measured in prior impedance measurements on a similarly grown sample.[33] These results suggest that tr-KFPM measurements can be used as a benchmark to determine the evolution of the activation energy. Activation energy decreases monotonically with decreasing Y doping for both polycrystalline and epitaxial films. The lowest activation energy is observed for the epitaxial films with 5% Y-doping, 0.45 eV. The monotonic change of activation energy in epitaxial sample points to an intrinsic effect on the activation energy solely due to dopant distribution in the host BZO material.

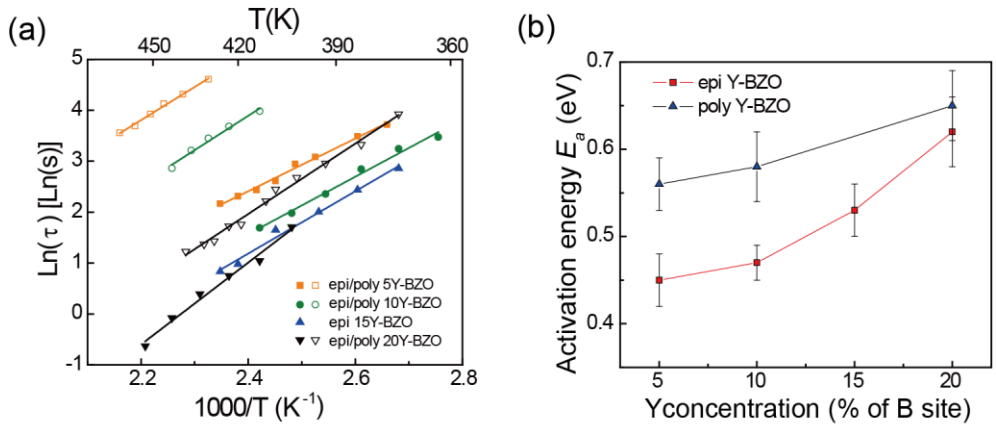

Figure 6-10 – (a) Arrhenius plot of the time constant as a function of Y concentration and microstructure (epitaxial films vs. polycrystalline films); (b) Activation energy as a function of Y concentration for polycrystalline (blue) and epitaxial (red) thin film samples.

6.4 Dopant Distribution Analysis

The presence of acceptor dopants has been reported to trap protons and cause a higher activation energy for proton conduction. However, this alone cannot explain the monotonic increase in activation energy with increasing dopant concentration. Clustering of yttrium atoms has been speculated to lead to an increase in the activation energy.[208] Hence, atom probe tomography (APT) measurements were performed on two dopant concentration, i.e. 5Y-BZO and 20Y-BZO samples for cluster analysis, as shown in Figure 6-11.[209] The APT sample preparation and measurement were performed in ORNL by Dr. Wei Guo.

The spatial distribution of Y atoms in 3D volumes for both samples (Figure 6-11 a and c) shows a rather homogeneous distribution of dopant. To statistically extract the distribution of dopants in Y-BZO and probe the existence of dopant clusters, the distribution analysis of Y-Y distance was performed on each experimental 3D APT data.

For each dopant atoms in APT, its n^{th} nearest neighbor distance (nNND) is recorded. The distribution of such distances are plotted for n = 1, 5 and 10, as shown in Figure 6-11 b and d.[210, 211] Meanwhile, the distribution from a purely randomly distributed dopant sample is also plotted in the same figure. It is found that all the normalized frequency of NND distribution fits perfectly with that of random distribution, suggesting that even at 20% doping, Y atoms are fully miscible and are homogeneously distributed across the sample.

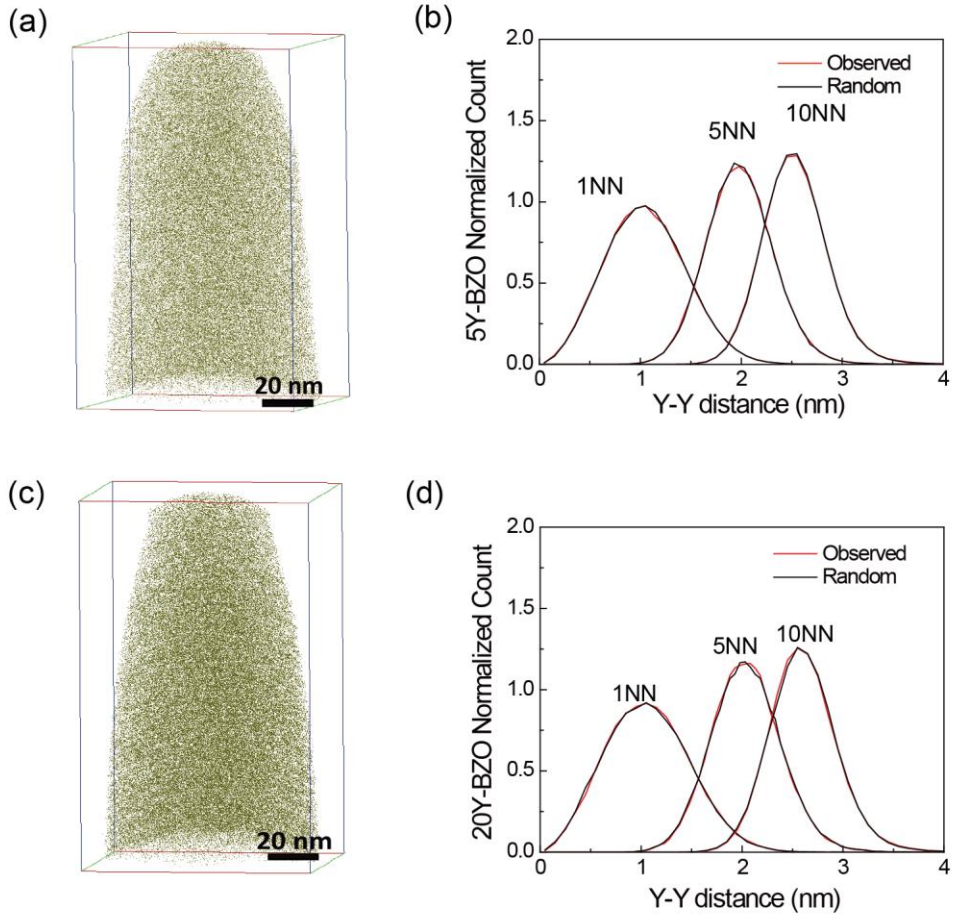

Figure 6-11 – APT characterization and analysis on 5Y-BZO (a, b) and 20Y-BZO (c, d) samples. (a, c) A reconstructed APT volume showing the homogeneous distribution of yttrium atoms (yellowish green); (b, d) Observed (red) and randomized (black) distribution of 1^{st}, 5^{th} and 10^{th} nearest neighbor Y-Y distance. Graph and data courtesy of Dr. Wei Guo, Oak Ridge National Laboratory.

This result suggests that any Y cluster, if exists, is smaller than ~2 nm and is beyond the detection resolution of APT. Therefore, Y clusters are homogeneously distributed in the lattice at nanometer scale. However, even for the random distribution of Y dopants suggested by APT measurements, the Y-Y cluster number should be statistically higher in higher dopant concentration. Therefore, the atomic distribution of each atom was simulated for each dopant concentration (simulation courtesy of Dr. Janakiraman Balachandran, Oak Ridge National Laboratory). Figure 6-12 shows the normalized distribution of the closest Y-Y distance for each Y atom as a function of dopant concentration. The distance of 4.20, 5.94, 7.27, 8.40 and 9.39 Å correspond to 1NN, 2NN, 3NN, 4NN and 5NN distances. With increasing dopant concentration, it is more likely to find a second Y atom around a dopant, at one of its 6 nearest lattice site. Indeed, in Figure 6-12, the first set of bars representing 1NN Y-Y cluster, which is a measure of the strength of Y-Y association, increases significantly with dopant concentration.

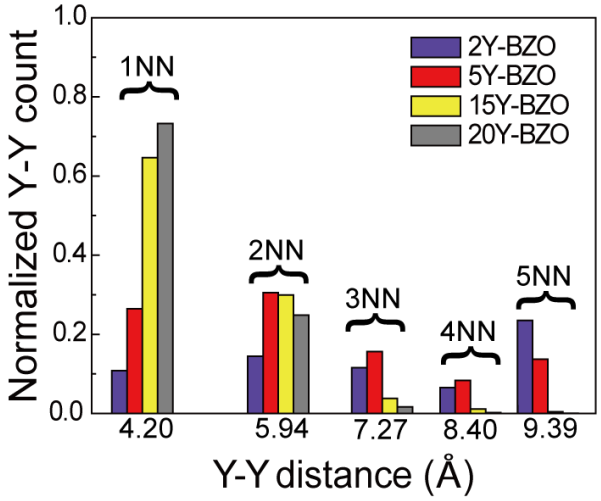

Figure 6-12 – Normalized distribution of the closest Y distance around every Y atom as a function of dopant concentration for a randomly doped system. Data courtesy of Dr. Janakiraman Balachandran, Oak Ridge National Laboratory.

To understand how an increase in such Y-Y dopant association can lead to an increase in the activation energy for proton conduction, detailed local atomic information is necessary to be related to interstitial proton migration energy from theory. Density functional theory (DFT) calculations were performed to uncover the influence of dopant cluster on the proton trapping (The DFT work was done by Dr. Janakiraman Balachandran, Oak Ridge National Laboratory). Specifically, the dopant-interstitial ($M'_{Zr} - H_i^{\cdot}$) interaction energies were calculated on four different dopant models with varying Y-Y cluster distance, as shown in Figure 6-13a. As the Y-Y distance increases from 1NN (4.20Å) to infinite long distance (i.e. a model with single Y), the dopant-proton interaction becomes less energetically favorable. This indicates that compared with a single yttrium, protons are trapped more strongly at Y-Y cluster site, which corresponds to the positively charged proton interstitial being in between two Y dopants.

The observed stronger proton trapping effect in Y-Y clusters is most possibly due to local atomic distortions. Such distortion occurs predominantly due to the polarizable oxygen sub-lattice that tries to screen the point charge from the defect. Its strength directly correlates with the strength of the defect interaction energy, where the maximal oxygen atom displacement is plotted as a proxy to the strength of the oxygen sub-lattice distortion. As shown in Figure 6-13b, the oxygen displacement, ΔR_O, is the distance between the actual oxygen position of distorted lattice and the ideal position of non-distorted lattice. The oxygen displacement is calculated on each 1NN oxygen ions of the yttrium or yttrium clusters, where the maximum oxygen displacement is obtained. It was found that with increasing Y-Y distance, the maximum oxygen displacement also decreases, indicating a smaller lattice distortion. The oxygen sub-lattice distortion is an electrostrictive effect and

points to the formation of a localized defect-polaron i.e. a small proton-polaron[204, 212, 213] at a proton interstitial site or a small electron-polaron[214] at an oxygen vacancy site, close to the dopant-site. A more favorable defect–dopant interaction energy implies that protons would show a more sluggish diffusion i.e. slower mobility. This suggests that increasing number of Y-Y neighbors can lead to an increased trapping of defects, due to the increased local distortion, thereby leading to an increase in the activation energy.

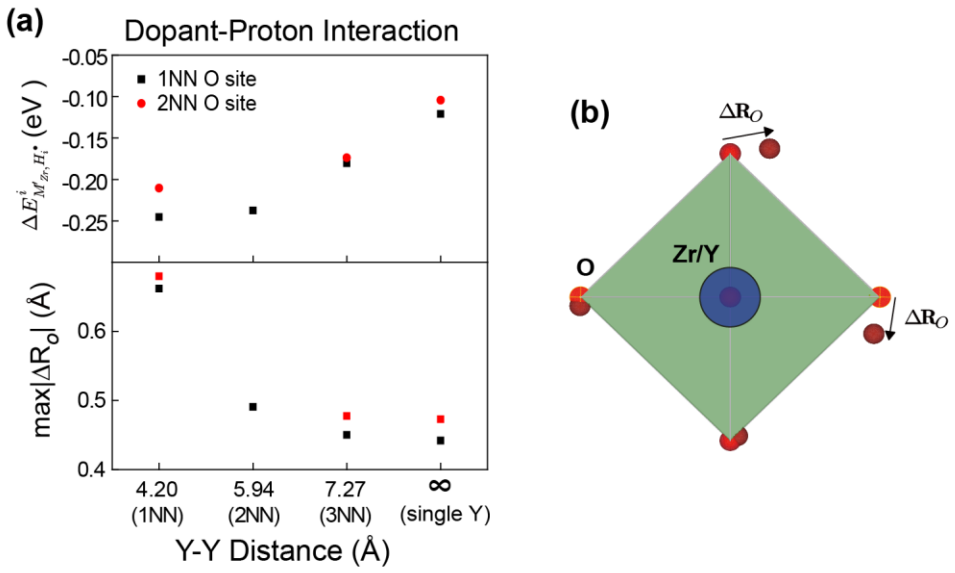

Figure 6-13 – (a) The interstitial-dopant interaction energy and the corresponding maximum oxygen displacement for models with different Y-Y cluster distance. (b) A schematic showing the oxygen displacement. Data courtesy of Dr. Janakiraman Balachandran, Oak Ridge National Laboratory.

6.5 Distortion Analysis

The above DFT calculation has suggested a positive relationship between the dopant-defect association with lattice distortion. Furthermore, experimental evidence is provided about the distortion in the lattice. Two types of local distortions were calculated on the local B-site coordination polyhedral directly from STEM images, i.e. B-site bond

angle deviation from cubic structure and B-site displacement, as shown in Figure 6-15a. Bond angle deviation, α, is calculated by the difference between each B-site bond angle with respect to the nearest B-site atoms and 90 degrees, showing how the lattice deviates from the cubic structure. Displacement, *d*, is defined as the distance between the observed B-site atoms and the unit cell center averaged from its four nearest A-site atoms.

The degree of the B-site bond angle deviation and displacement is displayed as a color map shown in Figure 6-14 to give a sense of how these local distortions are distributed in small volume sampled in a typical STEM images of 0, 5, 10, 15 and 20Y-BZO epitaxial films. The lattice distortions are rather random, supporting the previous conclusions of random dopant distribution in our thin films from APT. In addition, the distortion distribution was analyzed statistically. The histogram of normalized frequency of these two distortions as a function of dopant concentration are plotted in Figure 6-15b and c, with the fitted normal distribution curves for better comparison.[215] The peak from a histogram plot of the bond-angle deviation is the lowest for the 0Y-BZO sample (i.e. pure BZO) and is non-zero mainly due to inevitable scan distortions from STEM imaging. Compared to this value, both the peak and the standard deviation of the distortion distribution shift to higher values as the dopant concentration increases, implying an increase of lattice distortion with possible octahedral tilting, as shown in Figure 6-15b. Similar trend is also observed in displacement distribution (Figure 6-15c). From the STEM distortion analysis, it is demonstrated that with increasing dopant concentration, Y-BZO exhibits larger distortion in the lattice, which is most possibly due to the increase number of Y clusters.

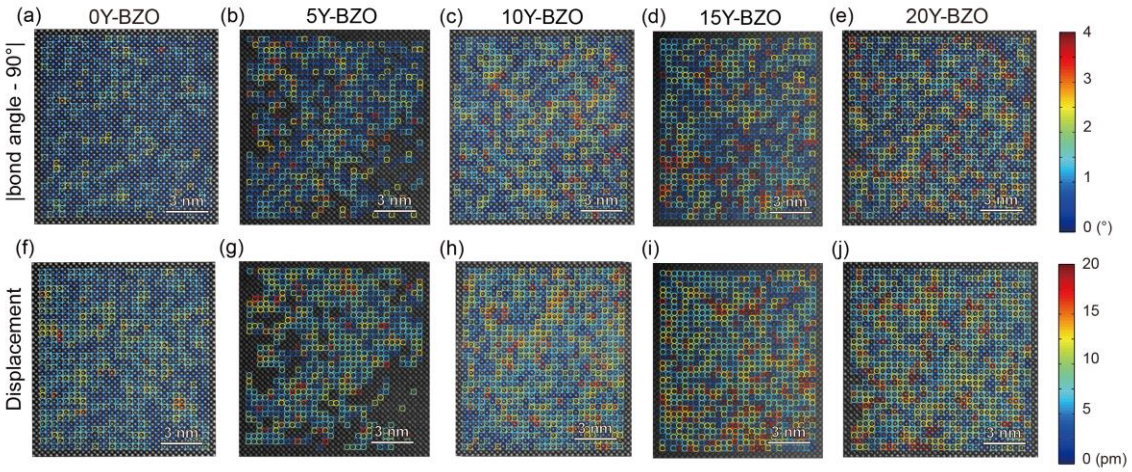

Figure 6-14 – Atomic resolution STEM imaging and quantitative data analysis to identify the bond angle deviation mapping (a-e) and displacement mapping (f-j) for Y-BZO sample with different dopant concentration.

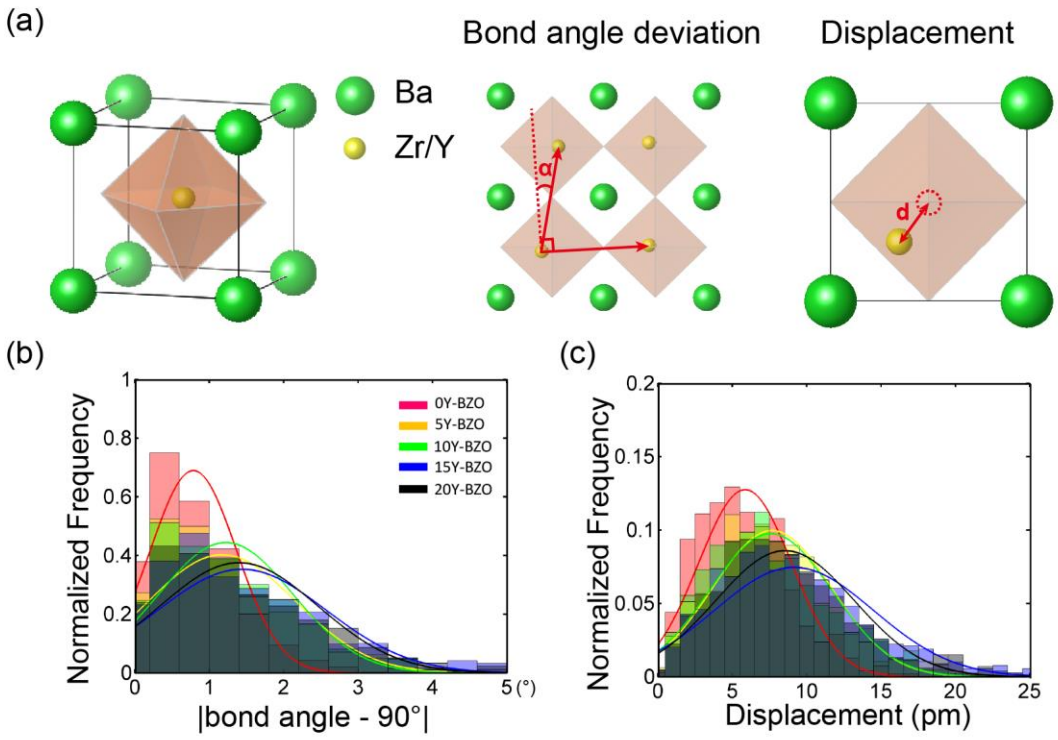

Figure 6-15 – (a) The representative perovskite structure of Y-BZO and the schematic showing how B-site bond angle deviation and B-site displacement are calculated; (b) Bond angle deviation distribution and the corresponding normal distribution fitting as a function of dopant concentration; (c) Displacement distribution and the corresponding normal distribution fitting as a function of dopant concentration.

6.6 Conclusions

To summarize, in this chapter, thin films of stoichiometric Y-BZO with dopant concentration ranging from 0% to 20% were prepared by PLD. Both single crystal and polycrystalline films were deposited by controlling the substrate temperature. The structure of the obtained samples was characterized by XRD and STEM. The conduction properties of Y-BZO were characterized by tr-KPFM, where the activation energy was calculated from the time constant of surface potential variation. It is found that the major charge carrier in Y-BZO is proton, and the activation energy of proton transport is higher in polycrystalline samples than that of single crystal samples, which is consistent with the blocking effect of the grain boundaries. In addition, the activation energy monotonically increases with increasing dopant concentration. To understand this phenomenon, dopant distribution was performed by APT; however, no dopant cluster was observed, demonstrating a fully miscible dopant in the lattice within the studied dopant range at nanometer level. Whereas at the sub-nanometer scale, the Y-Y cluster number is statistically higher in higher dopant concentration. According to DFT calculation, such clusters have stronger trapping effect towards protons than single dopant in the lattice. Meanwhile, the Y-Y clusters in the lattice are easy to condense a local lattice distortion and trap defects such as proton interstitials, thereby leading to a monotonic decrease of proton mobility. The lattice distortion in the lattice was further confirmed in atomic resolution images obtained via STEM.

CHAPTER 7. EFFECT OF NON-STOICHIOMETRY ON PROTON CONDUCTION IN Y-BZO

7.1 Introduction

Y-BZO has been widely studied for decades due to its high proton conductivity at intermediate temperatures, which has potential applications in fuel cell electrolytes. In Y-BZO, the introduction of yttrium induces oxygen vacancies, which will adsorb water in the environment, generating protonic defects on the surface. Such defects can diffuse into the bulk with counter diffusion of oxygen vacancies at intermediate temperatures. Long-distance proton transport is then enabled through Grotthuss mechanism, which includes proton rotating and jumping from one lattice oxygen ion to the adjacent one.[7]

While the previous chapter has focused on the proton transport mechanisms in stoichiometric Y-BZO, during synthesis, device fabrication and service, structural and chemical inhomogeneities can develop thereby modifying the local structure and possibly affecting transport properties of the material.[33, 119, 216-219] As an example, due to the highly refractory nature of bulk Y-BZO, high temperature sintering (T_{sint}>1600 °C) is often needed for its densification and grain growth.[220] Such high temperature leads to Ba loss, which causes lattice distortion, the formation of stacking faults, or even the emergence of lower conductivity phases (Y_2O_3), resulting in decreased total proton conductivity.[33, 217, 221, 222] While the decrease in proton conduction has been explained by the formation of non-proton conducting phases and by the decreasing proton concentration due to dopant element taking over A-sites, the fundamental understanding of how barium loss affects the

local lattice structure and proton transport mechanisms is still not clear. This challenge mostly comes from the presence of extended defects such as grain boundaries, which is detrimental to the proton conductivity in the lattice and create difficulties in direct correlation between the local atomic structure and the proton transport.

Inspired by the previous chapter, the PLD-grown epitaxial Y-BZO thin films is ideal for this study due to the limited grain boundaries and dislocations. In this chapter, the effect of non-stoichiometry, or more specifically, Ba-deficiency on proton conduction in Y-BZO is studied. To create a slight Ba deficiency, 20Y-BZO thin film samples were annealed in a furnace at 1050 °C for 24 h. A comprehensive study was performed to characterize the local structure and its influence on proton-transport properties of the thin-film samples using a set of complementary techniques, including APT, STEM-EELS and tr-KPFM.

7.2 Structural and Transport Properties

The crystal structure of the PLD deposited Y-BZO films before and after annealing was characterized by X-ray diffraction (XRD), as shown in Figure 7-1. The XRD patterns of both samples are in agreement with the perovskite-type structure of $BaZrO_3$ (JCPDS 00-006-0399), and only peaks corresponding to (100) orientation were observed, indicating that the deposited films are epitaxial along the (100) direction. In addition, no peak relative to a secondary phase was observed. The rocking curves of the (100) reflection was measured, as shown in the insets of each figure, with the full-width at half-maximum (FWHM) being 0.12° for non-annealed films and 0.13° for annealed films. The similar value of FWHM indicates that the crystal orientation is not greatly affected by annealing.

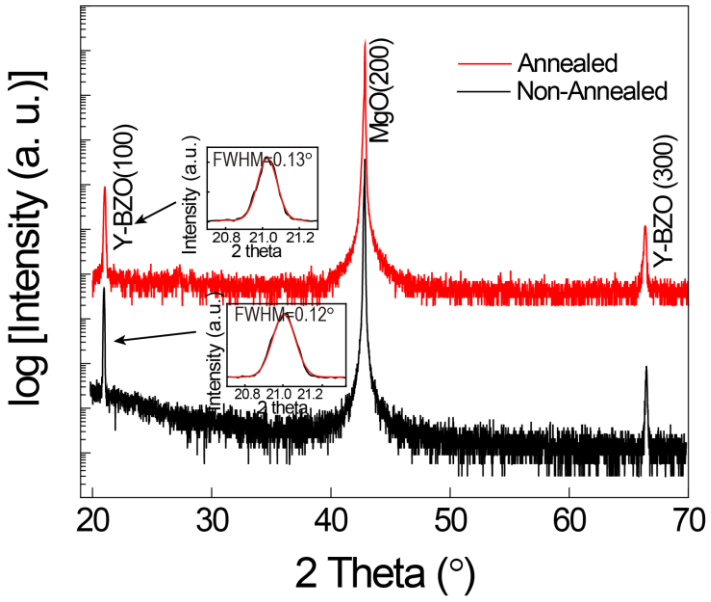

Figure 7-1 – XRD patterns of non-annealed and annealed 20Y-BZO films. The insets show the rocking curves of (100) peak.

Representative HAADF-STEM images from the non-annealed and annealed Y-BZO thin films are shown in Figure 7-2. For the non-annealed samples (Figure 7-2a, b), the STEM images confirm that the film is well oriented along (100) and without any detectable defects or secondary phases. Whereas after annealing (Figure 7-2c, d), the existence of planar defects and dark spheres can clearly be seen. The atomic resolution image (Figure 7-2d) shows that the darker region has slightly different orientation than the rest of the lattices, which indicate localized compositional and lattice distortion variations. However, no trace of secondary phase was observed. The sample has two parts: "major region" as for most of the area and "darker contrast region" as for the dark sphere or planar defect region.

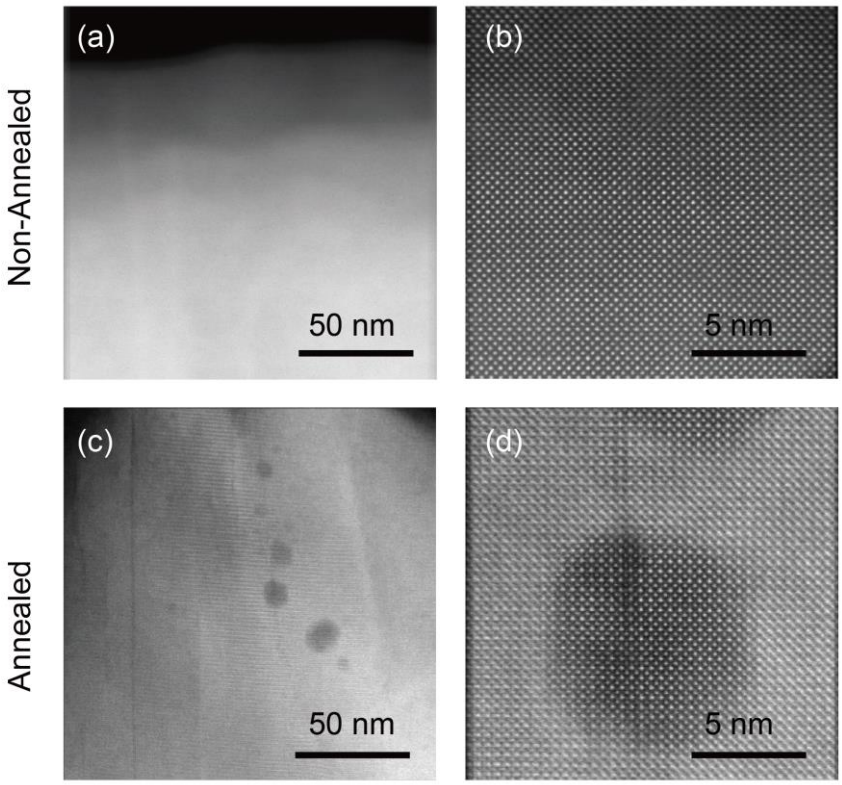

Figure 7-2 – High-angle annular dark field STEM images of the (a, b) non-annealed and (c, d) annealed 20Y-BZO films.

The high temperature annealing may cause a change of lattice distortion. Similar to the previous chapter, two types of local distortions were calculated on the local B-site coordination polyhedral directly from the STEM images. The schematic of how these distortions were calculated are shown in Figure 7-3a. The bond angle deviation, labeled as α, is the difference between the actual B-site bond angle with regard to the nearest B-site neighbors and 90° (cubic). The displacement, labeled as *d*, is a measure of the distance between the actual B-site atom location and the geometrical center of its four nearest A-site atoms. These two distortions are indicators of how the local lattice structure are deviated from the non-distorted structure.

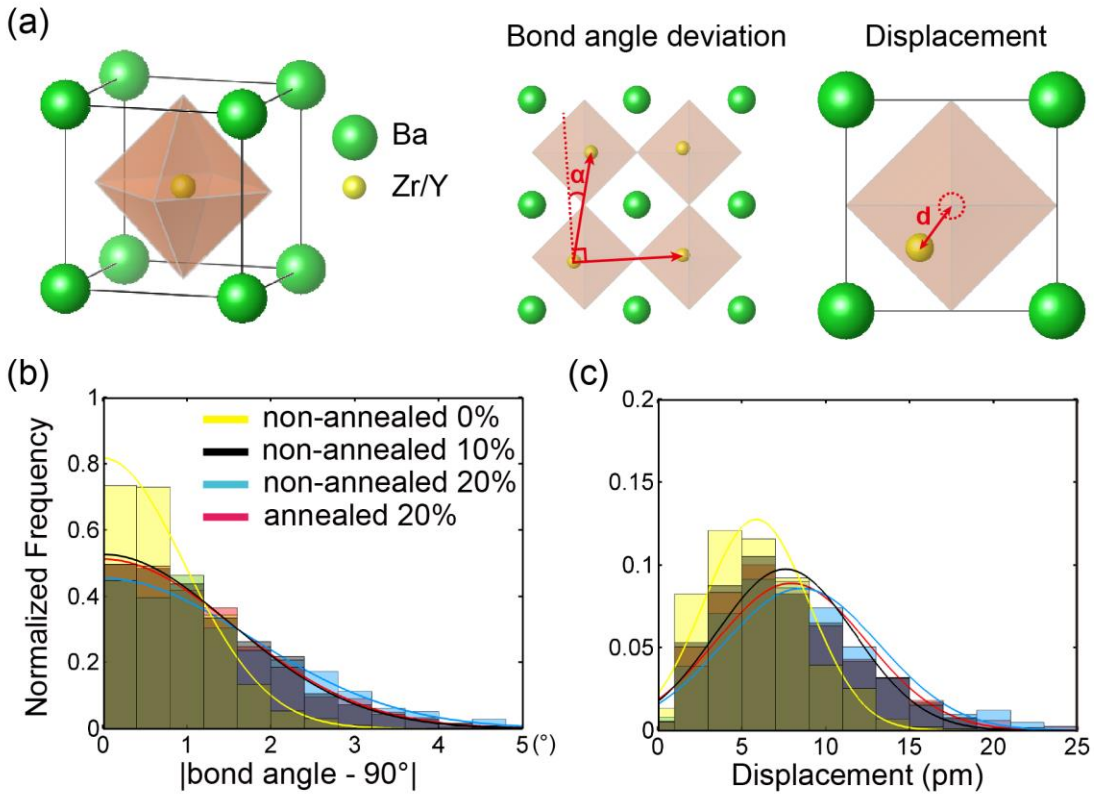

Figure 7-3 – (a) The representative perovskite structure of Y-BZO and the schematic showing how B-site bond angle deviation and B-site displacement are measured. (b, c) Normalized frequency and fitting of B-site bond angle deviation and displacement of annealed Y-BZO sample compared with non-annealed 0, 10 and 20Y-BZO.

While a single measured lattice distortion is not very meaningful by itself, a frequency-distribution obtained from hundreds of such distortions in an STEM image gives a statistical measure of the distortion, the distribution in which are meaningful and comparable. For the annealed sample, the darker contrast region is small and not continuous, and the corresponding lattice distortion analysis has relatively large error. Therefore, only the major region analysis was performed. The half-normal distribution and normal distribution were performed in addition to the histogram of normalized frequency of the two distortions, where the trend can be seen more clearly. Compared with non-annealed 20Y-BZO, the major phase of annealed sample shows a smaller bond angle

deviation, as well as a smaller displacement, indicative of a smaller distortion after annealing. The distortion value of non-annealed 0Y-BZO and 10Y-BZO is also shown in the figure as a reference. The distortion in annealed 20Y-BZO is comparable with that of non-annealed 10Y-BZO sample. As will be detailed in the following part, the decrease of distortion in the annealed sample may affect the proton conductivity in the lattice, as lattice distortion plays a crucial role in proton trapping and thus determines the activation energy for proton transport.

The observed lattice distortion change after annealing indicates a possible chemical composition variation in the annealed 20Y-BZO. Therefore, EELS analysis was performed on both major and darker contrast region of the annealed sample, as shown in Figure 7-4. The Ba concentration mapping at the planar defect region (Figure 7-4a) was less intense, suggesting a lower Ba concentration at this region. Line scan intensity profile measurements were also performed on the darker contrast regions, and a decreased intensity of Ba $M_{4,5}$-edge is observed, indicative of barium deficiency (Figure 7-4b).

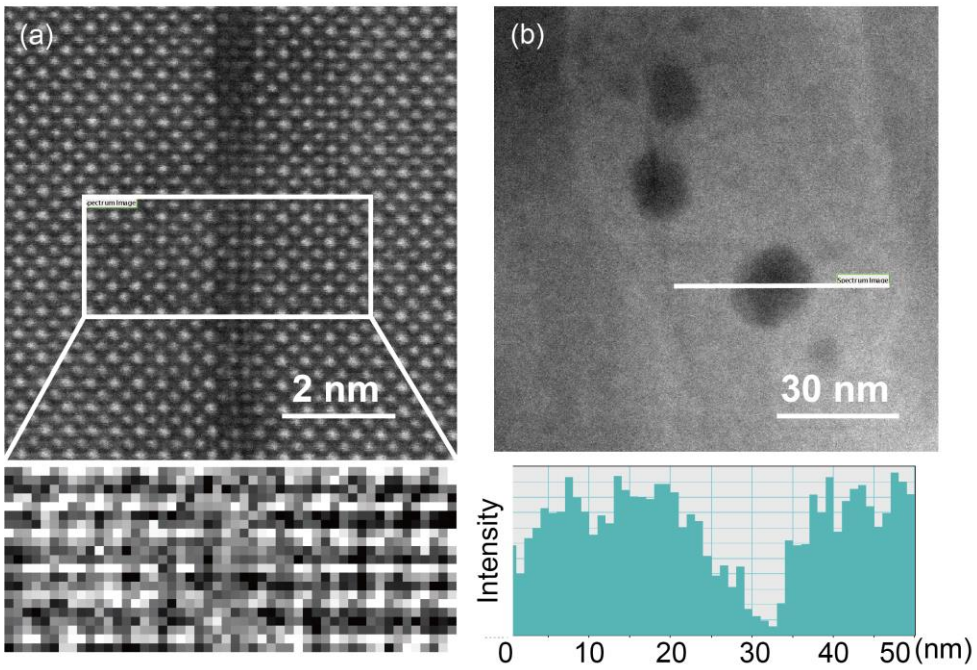

Figure 7-4 – (a) Atomic resolution STEM image of the planar defect and corresponding EELS spectrum image map from the Ba $M_{4,5}$-edge; (b) STEM image of dark sphere region and the Ba intensity mapping corresponding to the white scanning line.

APT measurements were performed to quantify the amount of barium deficiency in the annealed samples. APT sample preparation and measurements were conducted in ORNL by Dr. Wei Guo. As shown in Figure 6-11c, the non-annealed samples have a rather homogeneous distribution of yttrium. However, the annealed sample shows an yttrium cluster region that is similar in size as the dark spheroidal features observed via STEM, as shown in Figure 7-5a. The same area shows a Barium deficiency, as indicated in Figure 7-5b.

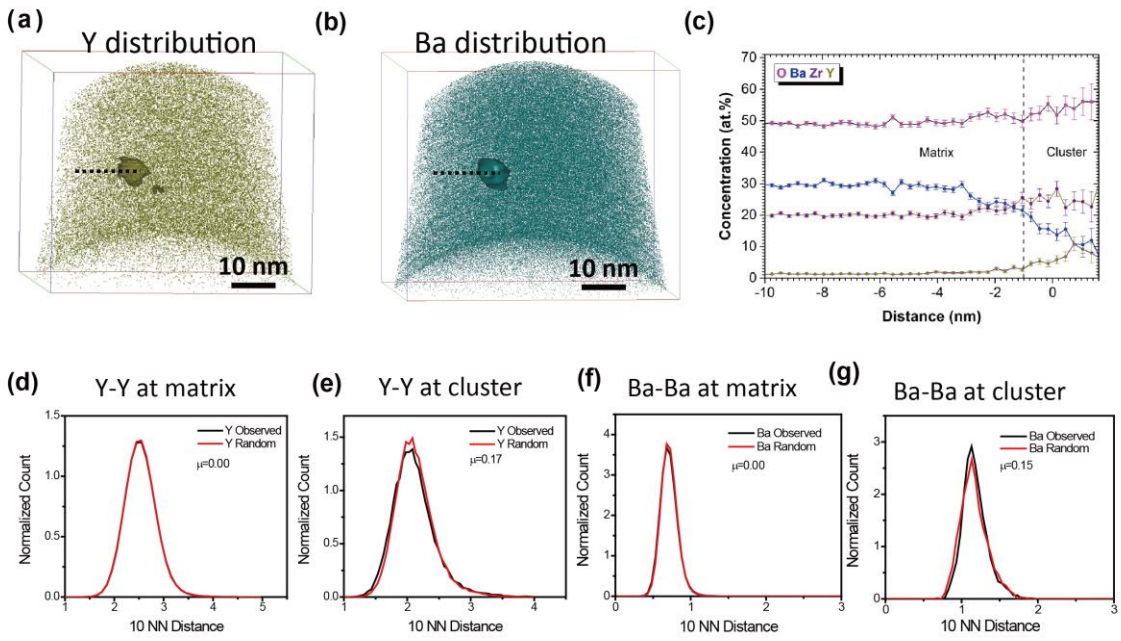

Figure 7-5 – APT analysis of annealed Y-BZO sample: (a) a reconstructed volume showing the distribution of yttrium atoms with two clusters envisioned by 5 at.% isoconcentration surfaces; (b) a reconstructed volume showing the distribution of barium atoms with a cluster envisioned by 20 at.% isoconcentration surfaces; (c) the concentration of Ba, Zr and Y atoms in matrix and cluster area, as shown dotted line in (a); (d) and (e) the distribution of normalized count for 10th nearest neighbor (10NN) of Y-Y distance at matrix and cluster region; (f) and (g) the distribution of normalized count for 10th nearest neighbor (10NN) of Ba-Ba distance at matrix and cluster region. All data and graphics courtesy of Dr. Wei Guo, Oak Ridge National Laboratory.

A closer look at the concentration of each element suggests that in the dopant cluster area, or the darker contrast region, the barium concentration significantly reduces, whereas the concentration of yttrium and zirconium increases, as shown in Figure 7-5c. Further nearest neighbor analysis was done on the spatially resolved atom mapping, and the distribution of normalized count for 10th nearest neighbor (10NN) of Y-Y and Zr-Zr distance at the matrix and cluster regions are summarized in Figure 7-5 d-g. The Y-Y cluster distribution at matrix is almost the same as the random distribution from statistical simulation, with μ=0.0, indicating that Y is homogeneously distributed in the matrix.

However, at cluster region, the distribution of Y cluster is slightly off the random distribution, with μ=0.17. The observed distribution of Y-Y distance of 10NN is slightly to the left of the random distribution, as shown in Figure 7-5e. This further demonstrates that yttrium clusters at this area. The similar calculation was performed on the Ba-Ba distance distribution, where μ=0.15. On the contrary, the observed distribution of Y-Y distance of 10NN is slightly to the right of the random distribution, suggesting a barium deficiency of the same area.

Tr-KPFM was used for the surface potential mapping for both thin film samples as a function of temperature, where the time constant of potential variation were obtained for each measurement. As shown in Figure 7-6, the annealed sample shows much smaller activation energy for proton transport (≈0.55 ± 0.01 eV), compared to that of the non-annealed sample (≈0.65 ± 0.01 eV). Within the measured temperature range (300 K < T < 450 K), the time constant for the annealed sample is always lower than that of non-annealed sample, indicating a superior proton conductivity for the annealed samples.

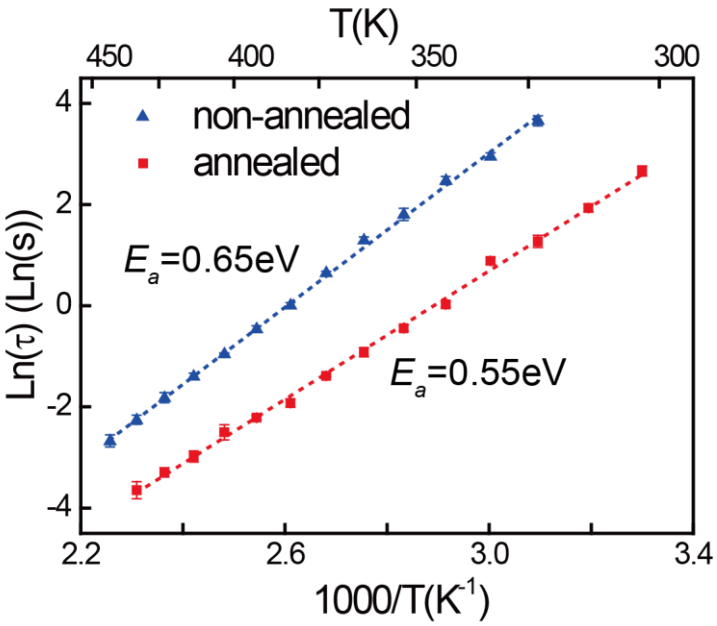

Figure 7-6 – Arrhenius plot of time constant (τ) for both annealed and non-annealed samples.

7.3 Discussions

Recent work by *Han et.al* employing X-ray diffraction from synchrotron sources identified that the 10% Ba-deficient 20Y-BZO exhibited two phases with an addition of slight amount of Y_2O_3.[217] Both the major phase and the minor phase were barium deficient. The major phase contained higher Ba concentration and lower Y concentration, where the Y dopants mostly substituted the B-site Zr ions. On the other hand, the minor phase showed darker contrast in STEM, exhibiting much lower Ba concentration and higher Y concentration, where Y substituted both the B-site (Zr) and A-site (Ba) ions.

In this work, instead of creating Ba deficiency of as much as 10% from the starting material, the Ba loss is from high temperature annealing, due to the volatile property of Ba.

The Ba loss is expected on the whole sample, generating Ba vacancies and oxygen vacancies, shown in Equation 50.

$$Ba_{Ba}^{x} + O_{O}^{x} \rightarrow V_{Ba}'' + V_{O}^{\cdot\cdot} + BaO \uparrow \quad (50)$$

The barium- and oxygen-vacancy defect dipoles can accommodate the lattice distortion and release the stress from yttrium dopant and especially Y-Y clusters, which explains the smaller lattice distortion observed in the major phase of STEM images.

As suggested by both EELS analysis and APT results, in the darker contrast region, the barium deficiency is stronger than the major region. Although perovskite phase is retained, the A-site vacancies may have occupied by Zr or Y, as suggested by previous studies:[223]

$$Zr_{Zr} + V_{Ba}'' \rightarrow Zr_{Ba}^{\cdot\cdot} + V_{Zr}'''' \quad (51)$$

$$Y_{Zr}' + V_{Ba}'' \rightarrow Y_{Ba}^{\cdot} + V_{Zr}'''' \quad (52)$$

The generation of Zr vacancies will consume oxygen vacancies, according to Equation 53.

$$V_{Zr}'''' + V_{Ba}'' + 3V_{O}^{\cdot\cdot} \rightarrow nil \quad (53)$$

In CHAPTER 6, a positive correlation between local structural distortion and proton activation energy was reported. With increasing distortion, the formation of a localized defect-polaron caused stronger trapping effect, impeding proton transport. Hence,

for the annealed sample that exhibits smaller local distortion, a decrease of proton trapping effect and thus a lower activation energy/higher proton mobility can be expected. In addition, according to Equation 50, the generation of oxygen vacancies in the major region of annealed Y-BZO provides increased proton concentration, which is also beneficial to the proton conduction. This is consistent with the tr-KPFM experiment in this study, where lower activation energy and higher mobility for proton is observed in annealed sample. Therefore, a slight barium deficiency is, to some extent, beneficial to the proton conduction property in Y-BZO. Similar effect was also observed in strained Y-BZO samples.[223]

However, creating Ba deficiency cannot always result in a better proton conductivity. The ionic transport property of a solid electrolyte is quantified by conductivity σ, which is defined as $\sigma = nze\mu$, where *n* is the density of charge carrier, *z* is charge number per ion, e is elementary charge, and μ is the mobility of the ion. Ionic mobility, as a thermally activated parameter, can be further written as $\mu = \mu_0 exp(-\frac{E_a}{kT})$, where E_a is the activation energy for ionic hopping, μ_0 is the pre-exponential factor and k is Boltzmann's constant. Therefore, with regard to the total proton conductivity, there is a trade-off effect between proton concentration and the activation energy: on one hand, slight Ba loss in the annealed sample induces a higher *n* due to the generation of oxygen vacancies and a lower E_a due to decreased lattice distortion/proton trapping, which leads to easier proton transport and better conduction properties as observed in this study; on the other hand, with further Ba loss, more B-site atoms substitution in barium site can be expected, consuming oxygen vacancies in the lattice according to Equation 51 and 52, which leads to a decrease of available protons for conduction.

It can further be expected that with even higher Ba deficiency (either by higher annealing temperature or reducing starting material), secondary phase forms in the lattice, which blocks the proton transport and lowers the available protons to conduct in the lattice.[217] Therefore, the optimization of proton conduction property of Y-BZO strongly depend on the quantified value of non-stoichiometry, which requires more investigation.

7.4 Conclusions

In this chapter, the effect of non-stoichiometry on proton transport properties in Y-BZO is studied. Epitaxial thin films of 20Y-BZO was prepared by PLD. After annealing at 1050 °C for 24 h, the major phase of the sample exhibited smaller local distortions compared to the stoichiometric non-annealed sample, which is due to the formation of Ba- and oxygen-vacancy dipoles that alleviate lattice distortion. Darker contrast regions including planar defects and dark spheres also formed after annealing, which showed even lower Ba concentration and higher Zr and Y concentration, indicative of possible A-site substitution by Zr/Y. The annealed Y-BZO showed lower activation energy for proton transport and higher mobility. The results identify a possible approach to improve proton transport properties in complex oxides by creating slight barium deficiency.

CHAPTER 8. CONCLUSIONS AND FUTURE WORK

This Chapter briefly summarizes the major findings in the thesis. Based on these findings, possible directions for future work are also recommended.

8.1 Conclusions

The operation of numerous electrochemical devices, such as lithium-ion batteries, fuel cells, gas sensors, catalysts, etc., relies on the surface/bulk electrochemistry and ionic transport. Understanding the ionic dynamics on the nanoscale is, thus, crucial for improving the performance of these applications and designing the next generation of devices. However, these processes are often complex and easily affected by the environmental conditions and the material's microstructure. In addition, single characterization techniques are usually limited in detecting the mechanisms at the full range of the environmental conditions, and multiple length scales involved.

To overcome these challenges, in this thesis, energy discovery platforms were developed, which are microfabricated lateral devices that enable multiple *in-situ* microscopy, spectroscopy, and functional characterization techniques to be performed on a single set-up. They provide easy control of external conditions including temperature (25 °C – 200 °C), humidity (0% – 90% at 25 °C), ambient gas (air and nitrogen), as well as applied electric field (1 V – 30 V). Through microfabrication, the composition, microstructure, lattice strain (-9.0% – 3.5%) and the presence and absence of TPBs of the material was also controlled, as needed. Multiple *in-situ* techniques, i.e. tr-KPFM and EIS, were performed on the same sample to cover a full range of ionic response. Structural and

compositional analysis were performed via a variety of techniques including AFM, SEM, XRD, STEM-EELS and APT. In addition, theoretical calculations (FEM and DFT) were performed to simulate and model the experimental phenomena, thus providing insight into the ionic dynamics.

Specifically, the electrochemical reactivity and ionic conductivity of two ionic conducting oxides, NC and Y-BZO, were investigated in this thesis. The resulting insight into their ionic dynamics are summarized below.

8.1.1 Ionic Dynamics of NC

The ionic dynamics studies were first performed on NC thin films via tr-KPFM. A surface potential change over time was observed in NC when external bias was repeatedly applied and removed. It was found that the observed surface potential variations were mainly a result of water splitting and transport of protons and hydroxyl groups on the NC surface. During polarization stage, water molecules were decomposed into protons in proximity to the biased electrode. They accumulated and migrated to the grounded electrode under electric field, resulting in a potential increase. During relaxation stage, the accumulated charge carriers on the surface dissipated and moved towards both electrodes, resulting in a decrease of surface potential. Within measured temperature and humidity range (25 °C – 140 °C, 0 – 90 % relative humidity as measured at 25 °C), the surface potential variation during polarization and relaxation stages generally increased with increasing humidity and/or temperature.

Further investigations suggested that such electrochemical reactions were taking place at the TPB, and the ionic transport was mainly taking place within 10 nm of the

sample surface. The atmosphere also played a crucial role in the ionic dynamics of NC: proton transport on NC was stronger in nitrogen atmosphere than in air, especially at higher temperatures, suggesting that oxygen vacancies may facilitate the process of proton generation and migration along NC.

The water splitting reaction at TPB and ionic transport along the surface of NC were then quantified via FEM. Four physical parameters associated with these processes, i.e. proton injection rate at TPB (S), proton dissipation constant (f), proton diffusivity (D) and mobility (μ) were obtained by fitting the experimental data at each environmental condition. It was found that the charge injection rate was a thermally activated process, with the activation energy of approximately 0.24 eV. The activation energy calculated from temperature dependency of proton diffusivity showed two distinct regions that matched well with the experimental results, and therefore, two environmental regimes for proton transport in NC were suggested:

- $T \lessapprox 100$ ℃: proton generation and conduction is enabled through the surface physisorbed water layer; in dry conditions, or wet conditions but at temperatures above a threshold value of ≈30-60 °C, the physisorbed layer is thinner and therefore, the overall conduction is limited by the proton generation and transport rates;
- 100 ℃ $\lessapprox T \lessapprox 135$ ℃ : more protons are generated due to the increased electrochemical reactivity, and protons are conducted through the chemisorbed water layer, with possible catalytic support from oxygen vacancies.

The effect of microstructure on the ionic dynamics of NC was investigated at temperatures below 200 °C, where five NC thin films with different microstructure were prepared by PLD, CSD and SD. Due to the different preparation methods and conditions, these films showed different surface roughness, grain boundary density and crystallographic orientation. It was found that the surface roughness was positively correlated with proton generation and conductivity at 25 °C and 90% RH, most probably due to the fact that proton transport is enabled through the physisorbed water layer on the NC surface. In contrast, at 125 °C and dry conditions - when the surface physisorbed water evaporates - the ionic dynamics were mainly dependent on the grain size and crystallographic orientation. The proton generation rate was negatively correlated with the grain size, while the proton transport though chemisorbed water was mainly affected by the surface plane orientation and presence of cracks and open pores connecting to the surface. Specifically, the proton diffusivity was positively correlated with the Lotgering factor of {111} planes, probably due to the ease of proton transport along {111} oriented NC surfaces.[106]

8.1.2 Proton Transport Mechanisms of Y-BZO

The energy discovery platforms were also used to study the ionic dynamics of Y-BZO. Stoichiometric Y-BZO thin films, both single- and poly-crystalline, with dopant concentration ranging from 0% to 20%, were prepared by PLD. The single- and poly-crystalline films were deposited by controlling the substrate temperature during deposition. Through tr-KPFM, it was found that the activation energy for proton transport was higher in polycrystalline samples than in single-crystalline samples, which was consistent with the blocking effect of the grain boundaries. In addition, the activation energy

monotonically increased with increasing dopant concentration. To understand this phenomenon, distortion analysis was performed on atomic resolution images obtained via STEM. As doping levels increased, Y-Y atom pairs increased statistically. These defect clusters are expected to condense a local lattice distortion and trap defects such as proton interstitials, thereby leading to a monotonic decrease of proton mobility.

The effect of non-stoichiometry on the composition and proton conductivity of Y-BZO was also studied. The non-stoichiometry was created through annealing 20Y-BZO thin films at 1050 °C for 24 h. The structural analysis of the annealed samples indicated the presence of two different regions. The majority of the annealed sample's volume exhibited smaller local distortions compared to the stoichiometric non-annealed sample. This reduction in distortion was suggested to result from the presence of Ba vacancies that accommodate the lattice distortion and release the stress from Y dopant and Y-Y clusters. Small volume within the annealed sample exhibited darker contrast spheres and dark lines, where Zr and Y atoms might occupy the Ba-vacancy sites. From tr-KPFM, the activation energy for proton transport for the annealed 20Y-BZO showed 0.55 eV, much lower than the stoichiometric sample (0.65 eV). It was concluded that slight Ba deficiency can result in better proton conduction in Y-BZO lattice within the measured temperature range (25 – 180 °C), possibly due to the reduced lattice distortion and thus the proton trapping effect in annealed samples.

8.2 Preliminary Results and Future Work

The present work has introduced ionic dynamics studies on the nanoscale through use of energy discovery platforms, and uncovered the effects of extrinsic and intrinsic

factors on the NC and Y-BZO thin films. Further studies are suggested below to extend the application of energy discovery platforms and confirm the theories proposed in this thesis, as recommended in the following sections.

8.2.1 Preliminary Results for the Effect of Lattice Strain on Proton Conduction in Y-BZO

From this thesis, it was concluded that the lattice distortion strongly affects the proton trapping effect, and thus the proton conduction properties in Y-BZO. Lattice strain is expected to significantly affect the distance and force between lattice ions, thus affecting the energy barrier for proton hopping within lattice. To date, a limited number of studies have been carried out to elucidate the role of lattice strain in proton conducting perovskite thin films. Yang *et al.* studied epitaxial Y-BZO thin films deposited on NGO substrates, and reported possible additional proton conduction pathways provided by compressive strain between Y-BZO and NGO interface, due to the formation of dislocation networks.[141] Chen *el al.* studied the effects of hydrostatic pressure applied to bulk yttrium doped barium cerate (Y-BCO), and found that activation energy of bulk conductivity increased from 0.62 eV to 0.73 eV with increasing pressure.[224] However, whether this change was a result of inter-atomic distance change or from intragranular space change was unclear.

To fully understand the effect of lattice strain on the proton conduction properties, epitaxial 20Y-BZO thin films were prepared by PLD, in order to minimize the contribution from other factors such as grain boundaries and dislocations. To create lattice strain, 20Y-BZO thin films were deposited on a variety of substrates with different lattice parameters, as shown in Figure 8-1, creating lattice mismatch ranging from -9.0 % to +3.5 %. [33, 140, 225]

Figure 8-1 – Schematic of different thin films studied in this work.

The structure and lattice parameters of Y-BZO films used are shown in Table 8-1. Lattice parameter for 20Y-BZO cubic is 4.24 Å. NGO has a pseudocubic lattice parameter of 3.86 Å. LSAT has cubic structure with lattice parameter of 3.87 Å. Both NGO and LSAT substrates have relatively large lattice mismatch with 20Y-BZO thin films, with -9.0 % and -8.7 % mismatch, respectively, and the as-grown 20Y-BZO is expected to show compressive strain when grown on these substrates. Figure 8-2a presents the STEM image of LSAT/20Y-BZO interface. As expected, a number of periodic dislocations are observed at the interface. Due to the formation of dislocations, the strain is partially relaxed, and the actual measured strain from lattice parameters are -5.0 % for NGO substrate, and -4.3 % for LSAT substrate.

Table 8-1 – The crystal parameters of Y-BZO and different substrate used in this study.

Materials	Structure	Parameters (Å)	Calculated strain	Measured strain
20Y-BZO	Cubic	4.24[226]	N/A	N/A
NGO	Pseudocubic	3.86[141]	-9.0 %	-5.0 %
LSAT	Cubic	3.87	-8.7 %	-4.3 %
MgO	Cubic	4.21	0.7 %	0.7 %
BCO	Cubic	4.39[227]	3.5 %	3.5 %

In contrast, the lattice parameter of MgO is 4.21 Å, which matches 20Y-BZO very well (0.7 % mismatch for both calculated and measured strain). As a result, no defects were observed at the interface, as shown in Figure 8-2b. Barium cerate (BCO) has similar crystal structure as BZO, and a larger lattice parameter of 4.39 Å. When epitaxially grown on (100) oriented 20Y-BCO, 20Y-BZO thin films show a slight tensile strain of about 3.5 %.[228] The STEM image of 20Y-BCO/20Y-BZO interface is shown in Figure 8-2c, where no obvious dislocations were observed at the interface, indicating a gradual release of lattice distortion. The measured strain from the STEM image is the same as the calculated value, 3.5 %. In this preliminary experiment, 20Y-BCO instead of pure BCO was used because BCO does not provide proton conduction, therefore the inner 20Y-BZO layer in the heterostructure that is not exposed to atmosphere cannot accept protons from the ambient, limiting the proton conduction.

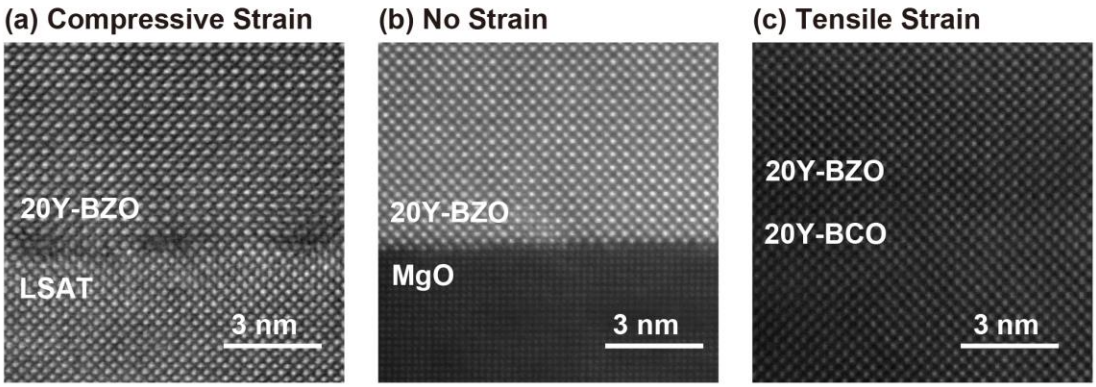

Figure 8-2 – STEM images of Y-BZO with (a) compressive strain, grown on LSAT substrate, (b) no strain, grown on MgO substrate and (c) tensile strain, grown on 20Y-BCO.

As shown in Figure 8-1, for films with compressive strain and no strain, about 30 nanometers of 20Y-BZO were grown on NGO, LSAT and MgO substrates. For tensile

strained films, two methods were used: a) about 3 nm of 20Y-BZO was first grown on MgO substrate as a buffer layer. Then approximately 6 nm of 20Y-BCO was deposited by PLD on 20Y-BZO. Finally, about 27 nm of 20Y-BZO was deposited on 20Y-BCO to create tensile strain of 20Y-BZO. b) about 1.5 nm of 20Y-BCO was deposited separately in between each deposition of 20Y-BZO, creating 20Y-BZO/20Y-BCO heterostructure.

The proton transport property of each sample was characterized by tr-KPFM at 90% RH and 25 – 200 °C, where surface potential mapping as a function of time were obtained.[185, 189] The time constant of surface potential variation was obtained as a function of temperature, as shown in Figure 8-3. It was found that the 20Y-BZO thin film with no strain showed the lowest activation energy for proton transport, 0.65 eV. Both compressive and tensile strained sample showed an increase of activation energy. It is worth noting that the heterostructured 20Y-BCO/20Y-BZO sample had higher activation energy (0.70±0.01 eV) than non-hetero counterpart (0.68±0.01 eV). In the heterostructured sample, the strain relaxes with distance, and the heterostructured sample preserves more strain, therefore have stronger trapping effect on the proton transport, leading to a higher activation energy.

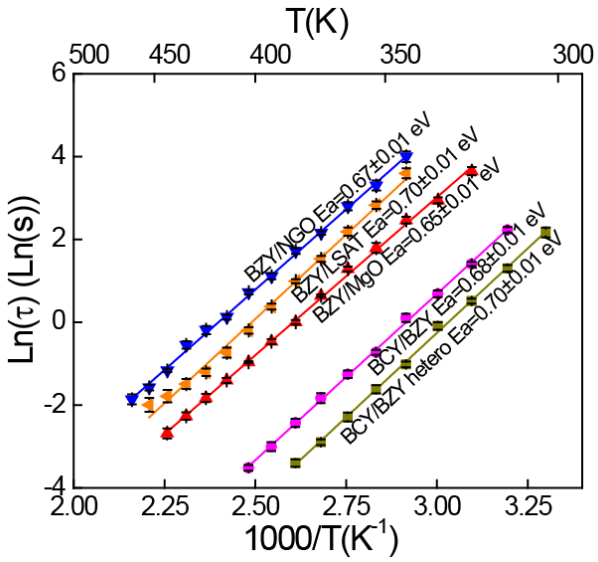

Figure 8-3 – Arrhenius plot of time constant for Y-BZO with different strain.

This preliminary result has suggested that both the compressive strain and tensile strain lead to an increase of activation energy for proton transport, from 0.65 up to 0.70 eV. To explore the origin of this observation, theoretical calculations such as DFT is suggested to study how the slight change of lattice parameters affect the energy barriers for proton transport in these films.

8.2.2 Further Development of Energy Discovery Platforms

In this thesis, the water splitting and transport of protons and/or hydroxyl groups were systematically studied in NC and Y-BZO under controlled environment. The SPM based tr-KPFM characterization offers excellent spatial and temporal resolutions, and is rather sensitive in detecting weak ionic transport corresponding to sub-femto-ampere currents. EIS, in addition to tr-KPFM, provides conduction information when impedance is relatively high. This study highlighted the importance of combining multiple

experimental approaches in electrochemical characterization of materials, which is a major advantage of energy discovery platforms.

The ionic dynamics study of NC and Y-BZO presented in this thesis demonstrate the feasibility of energy discovery platform. The application of such platforms, however, reaches far beyond this thesis. The wide functionality of functional materials is achieved though the understanding of the fundamental physical and chemical phenomena and their interactions (Figure 8-4). In the miniaturized devices, these phenomena are often intertwined, strongly limiting the fundamental understanding of their mechanisms. Energy discovery platforms take advantage of nanofabrication techniques, where device material and chemical gradient can be controlled as needed. Through the use of micro-Raman spectroscopy and SPM including tr-KPFM, piezo-response force microscopy (PFM), scanning impedance microscopy (SIM) and current-AFM, the local physical properties such as strain, and electric field can be excited and measured. The direct probing and correlation of these phenomena in the unprecedented resolution will enable a range of new discoveries and applications.

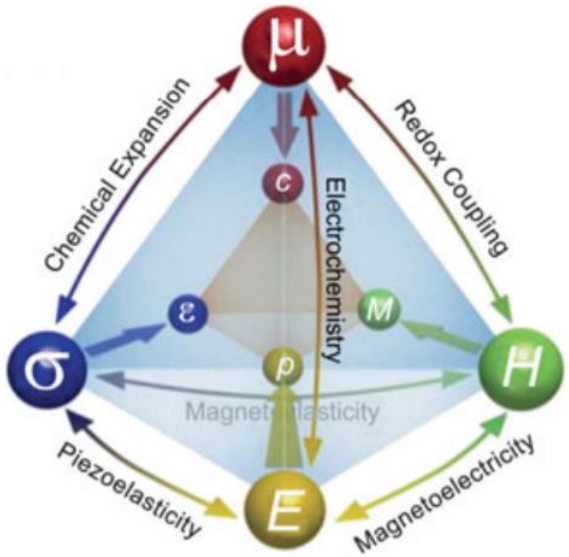

Figure 8-4 – Schematic of the coupling between chemical potential μ, electric field E, magnetic field H and stress σ.[229]

To further the application of energy discovery platforms, it is also suggested to integrate *in-situ* structural and compositional characterization into the platform. In the current study, although atomic resolution characterization including STEM, EELS and APT were performed, they were characterized separately on a different sample. They provided quantitative information regarding the lattice distortion and local composition at the atomic scale, but had potential challenges in correlating the structural and compositional information with the transport information due to sample-to-sample variation.

To enable such application, a special *in-situ* platform design compatible with STEM-EELS characterization is proposed as follows:

1. Thin film deposition of the materials of interest on Si/Si_3N_4 substrate, with electrodes deposited on top for biasing the material. There are several

commercial chips available for basic application of *in-situ* STEM. However, for more complicated applications, specific design and fabrication should be used.

2. Backside etching of silicon wafer using wet etching. Amorphous Si_3N_4 performs as etch stop, and is transparent under STEM.

This new design, when successful, will allow STEM-EELS techniques performed on the same (functional) material in addition to the tools already available such as SPM. It is envisioned to provide fundamental understanding of structure-property relationship on the nanometer to atomic scale. It is expected to be broadly applicable to a wide range of functional materials, including ferroelectric and flexoelectric materials, solid oxide electrolytes and battery components, where atomic scale structure and composition is crucial for their applications.

With the energy discovery platforms, some of the future research is proposed:

8.2.2.1 Transport study via controlled lattice strain

Recent studies have shown that helium implantation offers an entirely new pathway for strain engineering of perovskite thin films. For example, the oxygen octahedral distortions can be tailored continuously by helium dosage.[230] The out-of-plane lattice constant is also controllable by helium dosage without changing in-plane lattice constant in $La_{0.7}Sr_{0.3}MnO_3$.[231] The induced lattice distortion or strain by helium implantation is proven to be reversible through annealing.

Concluded from the present study, the lattice distortion and strain had significant contribution on the proton transport properties. However, the measurements were

performed on multiple samples for the comparison. Although they are prepared under controlled variables, there is potential risk of having other contributing factors such as defects and compositional variability between different samples, hindering the fundamental understanding of materials properties.

To eliminate such uncertainties, it is proposed to use free-standing membrane design for proton conduction properties study, where only one sample is needed, with a number of assigned areas for a variety of helium dosage. According to CHAPTER 6, the formation of B-site lattice distortion causes higher energy barrier for proton transport. Therefore, in the proposed study, we expect a similar but more meaningful trend, which is a gradual decrease in proton conduction with increasing helium dosage. This study is envisioned to not only confirm what we had obtained in the current study, but also to directly correlate the lattice structure with the conduction property on the same region, which is otherwise impossible. In addition, it can be readily applied to many other materials and applications due to the rather simple implementation (one sample instead of multiple deposition, and one for each characterization techniques).

As for detailed plan, firstly, STEM and tr-KPFM are performed on the whole sample, to obtain the lattice distortion and transport properties as a baseline. Then the thin film can be separated into multiple areas to be implanted with a variety of helium ion dosage. Both STEM and tr-KPFM provide nanometer-resolution that are able to identify each implanted area, and record the change of structure and transport properties. With this one-to-one correspondence of structure-property relationship, the effect of ion-induced lattice distortion can be obtained, which is expected to solely due to the helium induced lattice distortion. What is more, a third measurement can be performed after annealing as

a reference, when the distortion is fully relaxed and should be similar to the data before helium implantation.

This study, through strain engineering and in-situ strain observation, well provide much deeper insight into the strain induced transport modification.

8.2.2.2 Bias effect on lattice distortion and properties

With externally applied bias, the lattice structure and electrochemical reactivity are subject to change. For example, a recent study has revealed an increase of membrane strain with increasing applied bias in ceria thin films, and such increase in strain correlates with an increase in activation energy for oxygen conduction.[232] However, the spatially resolved electrochemical reactivity and impedance information on the nanometer scale is not available in most of the previous studies, and the direct correlation between such information with atomic scale structure and composition is not yet established.

With the versatile design and easy fabrication of energy discovery platforms, we expect to have a systematical understanding of the effect of bias on the local electrochemical properties on the nanoscale, and structural and compositional information on the atomic scale. When successful, a specially resolved strain mapping that correspond to the conductivity or electrochemical reactivity mapping of the same location will be obtained, and we expect a positive correlation between the applied electric field and lattice strain. The increase of lattice strain is expected to cause a drop of local conductivity due to the trapping effect, and cause stronger electrochemical or catalytic reactivity, due to stronger charge imbalance.

Specifically, different types of electrodes can be deposited onto the thin film membranes, creating a wide range of electric field applied to the material. Figure 8-5 shows two examples of electrodes design. Electrodes 1 and 3 are facing each other, for applying external bias. Electrodes 2 and 4 can be used for EIS measurement. Figure 8-5a illustrates a design of tip electrodes that can create strong electric field at the tip area. Figure 8-5b has parallel electrodes design that provide uniform electric field all over the sample. When external bias is applied, multiple SPM based techniques such as current-AFM and electrochemical strain microscopy (ESM) can be utilized to identify the electrochemical reactivity locally, and correlates with the electric field or electric field gradience. With implementation of in-situ STEM on the energy discovery platforms, the atomic resolution lattice strain mapping can be monitored while applying a series of external bias on the electrodes.

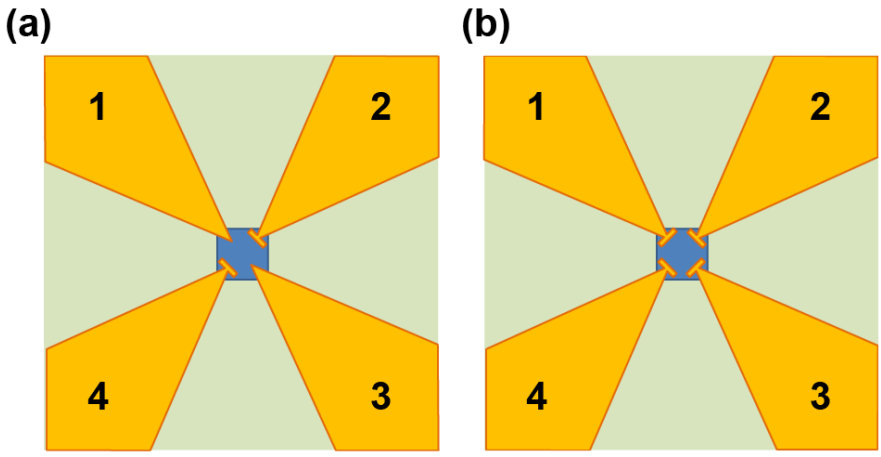

Figure 8-5 – Schematic of two electrode designs on material of interest.

8.2.3 Effects of Grain Size and Lotgering Factor

In this thesis, a variety of NC thin films with different microstructures were prepared, and the structure-property relationship was obtained by correlating the structural parameters and the ionic dynamics parameters, including charge injection rate *S* and proton diffusivity *D*. It was proposed that at low temperature and high humidity, *S* and *D* were mainly dependent on the surface roughness: a rougher surface condensed more water, leading to a stronger electrochemical reaction at TPB and larger diffusivity along the surface. On the contrary, at high temperature and dry conditions, *S* was negatively correlated with the grain size, and *D* was positively correlated with Lotgering factor of {111} direction.

However, other correlations, such as between *S* and {111} Lotgering factor, or *D* with grain size, might have been under-shadowed by outliers. The 700HV sample, for example, might offer the exceptionally high diffusivity due to additional proton diffusion pathways through large and deep cracks present in this sample (Figure 5-1c). To evaluate the significance of large and deep cracks in 700HV sample, it is recommended to use a more complete set of NC samples, with and without surface cracks. PLD processing parameters, such as substrate temperature and deposition pressure, can be modified in order to change microstructure and density of surface cracks. With such information, the governing structural factors on ionic dynamics at high temperature and dry condition can be further elucidated.

8.2.4 Fast Proton Conduction in K-BZO

In this work, we found that the activation energy for proton transport in Y-BZO was positively correlated with lattice distortion, which originated from increased presence

of Y-Y clusters. Therefore, there is a trade-off effect of dopant concentration: on one hand, higher dopant concentration increases oxygen vacancy density and thus the total available proton concentration for transport; on the other hand, higher dopant concentration can result in dopant clusters and trap protons, hindering their transport. In Y-BZO, the dopant atom is surrounded by an octahedron of oxygen ions. Due to the mismatch in size between Y and Zr ions, the octahedron is easily tilted and the lattice distorted. On the other hand, in A-site doped BZO structure such as K doped BZO and Na doped BZO, the dopant is surrounded by 12 oxygen atoms, forming a much larger cage that can accommodate a larger dopant with major lattice distortions. A-site doped BZO is, therefore, expected to be a possible solution for fast proton transport materials.

It is thus suggested to prepare A-site doped BZO. K-BZO is proposed as a starting material, due to a similar atomic size between K^+ (1.64 Å) and Ba^{2+} (1.61 Å) and thus a smaller lattice distortion. The distortion analysis via STEM and tr-KPFM can be used to identify lattice distortion and activation energy for proton transport. If the positive correlation between lattice distortion and activation energy in Y-BZO study holds true for other materials, we would expect to see a lower activation energy for proton transport in K-BZO compared to Y-BZO, due to smaller lattice distortion and thus a decreased trapping effect of dopant cluster.

8.3 Concluding Remarks

In this study, energy discovery platforms, a microfabricated lattice devices that enable multiple in-situ microscopy, spectroscopy and functional characterization techniques are developed, which dig into intertwined physical and electrochemical

properties and correlations on the nanoscale and atomic scale. The obtained comprehensive structure-properties relationship of NC and Y-BZO not only showcases the feasibility of energy discovery platforms in complex ionic dynamics study, but also facilitate material and device design with better performance and reliability. It is no doubt that with further development of energy discovery platforms, they can exhibit far more potential in the fundamental study of functional materials.

REFERENCES

1. Kraytsberg, A.; Ein-Eli, Y. *J Power Sources* **2011,** 196, (3), 886-893.

2. Adler, S. B. *Chem Rev* **2004,** 104, (10), 4791-4843.

3. Bagotsky, V. S., *Fuel Cells: Problems and Solutions*. Wiley: Hoboken, 2009.

4. Fabbri, E.; Magraso, A.; Pergolesi, D. *Mrs Bull* **2014,** 39, (9), 792-797.

5. Fabbri, E.; Pergolesi, D.; Traversa, E. *Chem Soc Rev* **2010,** 39, (11), 4355-4369.

6. Kreuer, K. D.; Paddison, S. J.; Spohr, E.; Schuster, M. *Chem Rev* **2004,** 104, (10), 4637-4678.

7. Kreuer, K. D. *Annu Rev Mater Res* **2003,** 33, 333-359.

8. Oesten, R.; Huggins, R. A. *Ionics* **1995,** 1, (5-6), 427-437.

9. Miura, N.; Kanamaru, K.; Shimizu, Y.; Yamazoe, N. *Solid State Ionics* **1990,** 40-1, 452-455.

10. Cheng, S. G.; Gupta, V. K.; Lin, J. Y. S. *Solid State Ionics* **2005,** 176, (35-36), 2653-2662.

11. Kharton, V. V.; Marques, F. M. B.; Atkinson, A. *Solid State Ionics* **2004,** 174, (1-4), 135-149.

12. Ryan P. O'Hayre, S.-W. C., Whitney Colella, Fritz B. Prinz, *Fuel Cell Fundamentals*. Wiley: Hoboken, NJ, 2006.

13. Haile, S. M. *Acta Mater* **2003,** 51, (19), 5981-6000.

14. Fergus, J. W. *J Power Sources* **2006,** 162, (1), 30-40.

15. Brett, D. J. L.; Atkinson, A.; Brandon, N. P.; Skinner, S. J. *Chem Soc Rev* **2008,** 37, (8), 1568-1578.

16. Ishihara, T., *Perovskite Oxide for Solid Oxide Fuel Cells*. Springer: 2009.

17. Yang, S. M.; Lee, S.; Jian, J.; Zhang, W. R.; Lu, P.; Jia, Q. X.; Wang, H. Y.; Noh, T. W.; Kalinin, S. V.; MacManus-Driscoll, J. L. *Nat Commun* **2015,** 6, (8588), 1-6.

18. Rose, L.; Menon, M.; Kammer, K.; Kesler, O.; Larsen, P. H. *Adv Mater Res-Switz* **2007,** 15-17, 293-298.

19. Iwahara, H.; Esaka, T.; Uchida, H.; Maeda, N. *Solid State Ionics* **1981,** 3-4, (Aug), 359-363.

20. Kreuer, K. D. *Solid State Ionics* **1997,** 97, (1-4), 1-15.

21. Norby, T.; Larring, Y. *Curr Opin Solid St M* **1997,** 2, (5), 593-599.

22. Kroger, F. A.; Vink, H. J. *Solid State Phys* **1956,** 3, 307-435.

23. Yamazaki, Y.; Blanc, F.; Okuyama, Y.; Buannic, L.; Lucio-Vega, J. C.; Grey, C. P.; Haile, S. M. *Nat Mater* **2013,** 12, (7), 647-651.

24. Kreuer, K. D.; Adams, S.; Munch, W.; Fuchs, A.; Klock, U.; Maier, J. *Solid State Ionics* **2001,** 145, (1-4), 295-306.

25. Norby, T. *Solid State Ionics* **1999,** 125, (1-4), 1-11.

26. Kakinuma, K.; Tomita, A.; Yamamura, H.; Atake, T. *J Mater Sci* **2006,** 41, (19), 6435-6440.

27. Miyoshi, S.; Akao, Y.; Kuwata, N.; Kawamura, J.; Oyama, Y.; Yagi, T.; Yamaguchi, S. *Chem Mater* **2014,** 26, (18), 5194-5200.

28. Tande, C.; Perez-Coll, D.; Mather, G. C. *J Mater Chem* **2012,** 22, (22), 11208-11213.

29. Scherrer, B.; Schlupp, M. V. F.; Stender, D.; Martynczuk, J.; Grolig, J. G.; Ma, H.; Kocher, P.; Lippert, T.; Prestat, M.; Gauckler, L. J. *Advanced Functional Materials* **2013,** 23, (15), 1957-1964.

30. Raz, S.; Sasaki, K.; Maier, J.; Riess, I. *Solid State Ionics* **2001,** 143, (2), 181-204.

31. Kim, S.; Avila-Paredes, H. J.; Wang, S. Z.; Chen, C. T.; De Souza, R. A.; Martin, M.; Munir, Z. A. *Phys Chem Chem Phys* **2009,** 11, (17), 3035-3038.

32. Avila-Paredes, H. J.; Barrera-Calva, E.; Anderson, H. U.; De Souza, R. A.; Martin, M.; Munir, Z. A.; Kim, S. *J Mater Chem* **2010,** 20, (30), 6235-6238.

33. Pergolesi, D.; Fabbri, E.; D'Epifanio, A.; Di Bartolomeo, E.; Tebano, A.; Sanna, S.; Licoccia, S.; Balestrino, G.; Traversa, E. *Nat Mater* **2010,** 9, (10), 846-852.

34. Tredici, I. G.; Maglia, F.; Ferrara, C.; Mustarelli, P.; Anselmi-Tamburini, U. *Advanced Functional Materials* **2014,** 24, (32), 5137-5146.

35. Shirpour, M.; Gregori, G.; Merkle, R.; Maier, J. *Phys Chem Chem Phys* **2011,** 13, (3), 937-940.

36. Avila-Paredes, H. J.; Chen, C. T.; Wang, S. Z.; De Souza, R. A.; Martin, M.; Munir, Z.; Kim, S. *J Mater Chem* **2010,** 20, (45), 10110-10112.

37. Gregori, G.; Shirpour, M.; Maier, J. *Advanced Functional Materials* **2013,** 23, (47), 5861-5867.

38. Oh, T. S.; Boyd, D. A.; Goodwin, D. G.; Haile, S. M. *Phys Chem Chem Phys* **2013,** 15, (7), 2466-2472.

39. Ruiz-Trejo, E.; Kilner, J. A. *J Appl Electrochem* **2009,** 39, (4), 523-528.

40. Takamura, H.; Takahashi, N. *Solid State Ionics* **2010,** 181, (3-4), 100-103.

41. Yinon, J. *Trac-Trend Anal Chem* **2002,** 21, (4), 292-301.

42. Haugen, J. E.; Rudi, K.; Langsrud, S.; Bredholt, S. *Anal Chim Acta* **2006,** 565, (1), 10-16.

43. Kruis, F. E.; Fissan, H.; Peled, A. *J Aerosol Sci* **1998,** 29, (5-6), 511-535.

44. Timmer, B.; Olthuis, W.; van den Berg, A. *Sensor Actuat B-Chem* **2005,** 107, (2), 666-677.

45. Liu, Y. X.; Parisi, J.; Sun, X. C.; Lei, Y. *J Mater Chem A* **2014,** 2, (26), 9919-9943.

46. Azad, A. M.; Akbar, S. A.; Mhaisalkar, S. G.; Birkefeld, L. D.; Goto, K. S. *J Electrochem Soc* **1992,** 139, (12), 3690-3704.

47. Moseley, P. T. *Meas Sci Technol* **1997,** 8, (3), 223-237.

48. Werle, P.; Slemr, F.; Maurer, K.; Kormann, R.; Mucke, R.; Janker, B. *Opt Laser Eng* **2002,** 37, (2-3), 101-114.

49. Pohle, R.; Fleischer, M.; Meixner, H. *Sensor Actuat B-Chem* **2000,** 68, (1-3), 151-156.

50. Gibson, D.; MacGregor, C. *Sensors-Basel* **2013,** 13, (6), 7079-7103.

51. Mizaikoff, B. *Chem Soc Rev* **2013,** 42, (22), 8683-8699.

52. Suresh, M.; Vasa, N. J.; Agarwal, V.; Chandapillai, J. *Sensor Actuat B-Chem* **2014,** 195, 44-51.

53. Zhu, H. B.; Nidetz, R.; Zhou, M. L.; Lee, J.; Buggaveeti, S.; Kurabayashi, K.; Fan, X. D. *Lab Chip* **2015,** 15, (14), 3021-3029.

54. Lewis, A. C.; Hamilton, J. F.; Rhodes, C. N.; Halliday, J.; Bartle, K. D.; Homewood, P.; Grenfell, R. J. P.; Goody, B.; Harling, A. M.; Brewer, P.; Vargha, G.; Milton, M. J. T. *J Chromatogr A* **2010,** 1217, (5), 768-774.

55. Vyas, J. C.; Katti, V. R.; Gupta, S. K.; Yakhmi, J. V. *Sensor Actuat B-Chem* **2006,** 115, (1), 28-32.

56. Magori, V. In *Ultrasonic Sensors in Air*, Proc. IEEE Ultrason. Symp., 1994; pp 471-481.

57. Kumar, S.; Furuhashi, H. *Ultrasonics* **2017,** 74, 186-195.

58. Wykes, C.; Carr, H.; Munro, W. S. H.; Nagi, F.; Pomeroy, S.; Rafiq, M.; Webb, P.; Gibson, I. *Ultrasonics International 93 - Conference Proceedings* **1993**, 667-670.

59. Tomchenko, A. A.; Harmer, G. P.; Marquis, B. T.; Allen, J. W. *Sensor Actuat B-Chem* **2003,** 93, (1-3), 126-134.

60. Barsan, N.; Koziej, D.; Weimar, U. *Sensor Actuat B-Chem* **2007,** 121, (1), 18-35.

61. Sakai, G.; Matsunaga, N.; Shimanoe, K.; Yamazoe, N. *Sensor Actuat B-Chem* **2001,** 80, (2), 125-131.

62. Matsunaga, N.; Sakai, G.; Shimanoe, K.; Yamazoe, N. *Sensor Actuat B-Chem* **2002,** 83, (1-3), 216-221.

63. Jasinski, P. *Mater Sci-Poland* **2006,** 24, (1), 269-278.

64. Bhoga, S. S.; Singh, K. *Ionics* **2007,** 13, (6), 417-427.

65. Park, C. O.; Fergus, J. W.; Miura, N.; Park, J.; Choi, A. *Ionics* **2009,** 15, (3), 261-284.

66. Currie, J. F.; Essalik, A.; Marusic, J. C. *Sensor Actuat B-Chem* **1999,** 59, (2-3), 235-241.

67. Barreca, D.; Gasparotto, A.; Maccato, C.; Maragno, C.; Tondello, E.; Comini, E.; Sberveglieri, G. *Nanotechnology* **2007,** 18, (12), 125502.

68. Beie, H. J.; Gnorich, A. *Sensor Actuat B-Chem* **1991,** 4, (3-4), 393-399.

69. Miremadi, B. K.; Singh, R. C.; Chen, Z.; Morrison, S. R.; Colbow, K. *Sensor Actuat B-Chem* **1994,** 21, (1), 1-4.

70. Liu, H.; Du, X. W.; Xing, X. R.; Wang, G. X.; Qiao, S. Z. *Chem Commun* **2012,** 48, (6), 865-867.

71. Li, Y. M.; Liang, J.; Tao, Z. H.; Chen, J. *Mater Res Bull* **2008,** 43, (8-9), 2380-2385.

72. Sun, B.; Horvat, J.; Kim, H. S.; Kim, W. S.; Ahn, J.; Wang, G. X. *J Phys Chem C* **2010,** 114, (44), 18753-18761.

73. Li, B. X.; Xie, Y.; Jing, M.; Rong, G. X.; Tang, Y. C.; Zhang, G. Z. *Langmuir* **2006,** 22, (22), 9380-9385.

74. Maekawa, T.; Tamaki, J.; Miura, N.; Yamazoe, N.; Matsushima, S. *Sensor Actuat B-Chem* **1992,** 9, (1), 63-69.

75. Rani, R. A.; Zoolfakar, A. S.; Ou, J. Z.; Field, M. R.; Austin, M.; Kalantar-zadeh, K. *Sensor Actuat B-Chem* **2013,** 176, 149-156.

76. Dirksen, J. A.; Duval, K.; Ring, T. A. *Sensor Actuat B-Chem* **2001,** 80, (2), 106-115.

77. Du, Y.; Wang, W. N.; Li, X. W.; Zhao, J.; Ma, J. M.; Liu, Y. P.; Lu, G. Y. *Mater Lett* **2012,** 68, 168-170.

78. Williams, G.; Coles, G. S. V. *Sensor Actuat B-Chem* **1993,** 16, (1-3), 349-353.

79. Michel, C. R.; Martinez-Preciado, A. H.; Contreras, N. L. L. *Sensor Actuat B-Chem* **2013,** 184, 8-14.

80. Karunagaran, B.; Uthirakumar, P.; Chung, S. J.; Velumani, S.; Suh, E. K. *Mater Charact* **2007,** 58, (8-9), 680-684.

81. Tang, H.; Prasad, K.; Sanjines, R.; Levy, F. *Sensor Actuat B-Chem* **1995,** 26, (1-3), 71-75.

82. Lin, H. M.; Keng, C. H.; Tung, C. Y. *Nanostruct Mater* **1997,** 9, (1-8), 747-750.

83. Li, X. L.; Lou, T. J.; Sun, X. M.; Li, Y. D. *Inorg Chem* **2004,** 43, (17), 5442-5449.

84. Sberveglieri, G.; Depero, L.; Groppelli, S.; Nelli, P. *Sensor Actuat B-Chem* **1995,** 26, (1-3), 89-92.

85. Carotta, M. C.; Martinelli, G.; Sadaoka, Y.; Nunziante, P.; Traversa, E. *Sensor Actuat B-Chem* **1998,** 48, (1-3), 270-276.

86. Gunasekaran, N.; Meenakshisundaram, A.; Srinivasan, V. *Surf Technol* **1984,** 22, (1), 89-98.

87. Zhou, Z. G.; Tang, Z. L.; Zhang, Z. T.; Wlodarski, W. *Sensor Actuat B-Chem* **2001,** 77, (1-2), 22-26.

88. Wang, W. S.; Virkar, A. V. *J Power Sources* **2005,** 142, (1-2), 1-9.

89. Agadzhanyan, S. A.; Pogosyan, A. A.; Karabashyan, L. V. *Mol Biol+* **1982,** 16, (2), 279-284.

90. Cerda, J.; Arbiol, J.; Dezanneau, G.; Diaz, R.; Morante, J. R. *Sensor Actuat B-Chem* **2002,** 84, (1), 21-25.

91. Usui, T.; Asada, A.; Ishibashi, K.; Nakazawa, M. *J Electrochem Soc* **1991,** 138, (2), 585-588.

92. Obayashi, H.; Sakurai, Y.; Gejo, T. *J Solid State Chem* **1976,** 17, (3), 299-303.

93. Decollongue, B.; Garbowski, E.; Primet, M. *J Chem Soc Faraday T* **1991,** 87, (15), 2493-2499.

94. Sayle, T. X. T.; Parker, S. C.; Catlow, C. R. A. *J Chem Soc Chem Comm* **1992**, (14), 977-978.

95. Zhu, B.; Fan, L. D.; Lund, P. *Appl Energ* **2013,** 106, 163-175.

96. Inaba, H.; Tagawa, H. *Solid State Ionics* **1996,** 83, (1-2), 1-16.

97. Ciucci, F.; Chueh, W. C.; Goodwin, D. G.; Haile, S. M. *Phys Chem Chem Phys* **2011,** 13, (6), 2121-2135.

98. Kungas, R.; Bidrawn, F.; Vohs, J. M.; Gorte, R. J. *Electrochem Solid St* **2010,** 13, (8), B87-B90.

99. Moseley, P. T. *Sensor Actuat B-Chem* **1992,** 6, (1-3), 149-156.

100. Chueh, W. C.; Falter, C.; Abbott, M.; Scipio, D.; Furler, P.; Haile, S. M.; Steinfeld, A. *Science* **2010,** 330, (6012), 1797-1801.

101. Kokan, J. R.; Gerhardt, R. A. *Electrically Based Microstructural Characterization* **1996,** 411, 419-424.

102. Gerhardt, R. A.; Cao, W. Q. *Ieee 1996 Annual Report - Conference on Electrical Insulation and Dielectric Phenomena, Vols I & Ii* **1996**, 102-105.

103. Cao, W. Q.; Gerhardt, R.; Wachtman, J. B. *Ceram Trans* **1990,** 8, 175-184.

104. Ramachandran, K.; Pruyn, T. L.; Huang, T.; Wang, Y. S.; Singh, P. M.; Ready, W. J.; Gerhardt, R. A.; Sundaram, V.; Tummala, R. *J Mater Sci-Mater El* **2015,** 26, (4), 2563-2570.

105. Yang, Z. X.; Wang, Q. G.; Wei, S. Y.; Ma, D. W.; Sun, Q. A. *J Phys Chem C* **2010,** 114, (35), 14891-14899.

106. Molinari, M.; Parker, S. C.; Sayle, D. C.; Islam, M. S. *J Phys Chem C* **2012,** 116, (12), 7073-7082.

107. Fronzi, M.; Piccinin, S.; Delley, B.; Traversa, E.; Stampfl, C. *Phys Chem Chem Phys* **2009,** 11, (40), 9188-9199.

108. Verdaguer, A.; Weis, C.; Oncins, G.; Ketteler, G.; Bluhm, H.; Salmeron, M. *Langmuir* **2007,** 23, (19), 9699-9703.

109. Gritschneder, S.; Reichling, M. *Nanotechnology* **2007,** 18, (4), 044024.

110. Choi, Y. M.; Abernathy, H.; Chen, H. T.; Lin, M. C.; Liu, M. L. *Chemphyschem* **2006,** 7, (9), 1957-1963.

111. Huang, M.; Fabris, S. *Phys Rev B* **2007,** 75, (8), 081404.

112. Zhang, J.; Kumagai, H.; Yamamura, K.; Ohara, S.; Takami, S.; Morikawa, A.; Shinjoh, H.; Kaneko, K.; Adschiri, T.; Suda, A. *Nano Lett* **2011,** 11, (2), 361-364.

113. Giuliano Gregori, M. S., Joachim Maier. *Advanced Functional Materials* **2013,** 23, (47), 5861-5867.

114. Rodriguez, J. A.; Ma, S.; Liu, P.; Hrbek, J.; Evans, J.; Perez, M. *Science* **2007,** 318, (5857), 1757-1760.

115. Mudiyanselage, K.; Stacchiola, D. *Abstr Pap Am Chem S* **2013,** 246, (19), 5101-5.

116. Vecchietti, J.; Bonivardi, A.; Xu, W. Q.; Stacchiola, D.; Delgado, J. J.; Calatayud, M.; Collins, S. E. *Acs Catal* **2014,** 4, (6), 2088-2096.

117. Fu, Q.; Saltsburg, H.; Flytzani-Stephanopoulos, M. *Science* **2003,** 301, (5635), 935-938.

118. Taniguchi, N.; Hatoh, K.; Niikura, J.; Gamo, T.; Iwahara, H. *Solid State Ionics* **1992,** 53, 998-1003.

119. Babilo, P.; Uda, T.; Haile, S. M. *J Mater Res* **2007,** 22, (5), 1322-1330.

120. Chen, C. T.; Danel, C. E.; Kim, S. *J Mater Chem* **2011,** 21, (14), 5435-5442.

121. Maier, J. *Prog Solid State Ch* **1995,** 23, (3), 171-263.

122. Kim, S.; Fleig, J.; Maier, J. *Phys Chem Chem Phys* **2003,** 5, (11), 2268-2273.

123. Guo, X.; Waser, R. *Prog Mater Sci* **2006,** 51, (2), 151-210.

124. Yazdi, M. A. P.; Briois, P.; Georges, S.; Shaula, A. L.; Cavaleiro, A.; Billard, A. *J Electrochem Soc* **2010,** 157, (11), B1582-B1587.

125. Peng, C.; Melnik, J.; Luo, J. L.; Sanger, A. R.; Chuang, K. T. *Solid State Ionics* **2010,** 181, (29-30), 1372-1377.

126. Tao, S. W.; Irvine, J. T. S. *Adv Mater* **2006,** 18, (12), 1581-1584.

127. Gao, D. Y.; Guo, R. S. *J Alloy Compd* **2010,** 493, (1-2), 288-293.

128. Park, K. Y.; Seo, Y.; Kim, K. B.; Song, S. J.; Park, B.; Park, J. Y. *J Alloy Compd* **2015,** 639, 435-444.

129. Ricote, S.; Bonanos, N. *Solid State Ionics* **2010,** 181, (15-16), 694-700.

130. Sun, W. P.; Shi, Z.; Liu, M. F.; Bi, L.; Liu, W. *Advanced Functional Materials* **2014,** 24, (36), 5695-5702.

131. Sun, Z. Q.; Fabbri, E.; Bi, L.; Traversa, E. *J Am Ceram Soc* **2012,** 95, (2), 627-635.

132. Savaniu, C. D.; Canales-Vazquez, J.; Irvine, J. T. S. *J Mater Chem* **2005,** 15, (5), 598-604.

133. Fabbri, E.; D'Epifanio, A.; Di Bartolomeo, E.; Licoccia, S.; Traversa, E. *Solid State Ionics* **2008,** 179, (15-16), 558-564.

134. Tauer, T.; O'Hayre, R.; Medlin, J. W. *Chem Mater* **2014,** 26, (17), 4915-4924.

135. Raiteri, P.; Gale, J. D.; Bussi, G. *J Phys-Condens Mat* **2011,** 23, (33), 334213.

136. Kitamura, N.; Akola, J.; Kohara, S.; Fujimoto, K.; Idemoto, Y. *J Phys Chem C* **2014,** 118, (33), 18846-18852.

137. Dawson, J. A.; Miller, J. A.; Tanaka, I. *Chem Mater* **2015,** 27, (3), 901-908.

138. An, J. W.; Kim, Y. B.; Jung, H. J.; Park, J. S.; Cha, S. W.; Gur, T. M.; Prinz, F. B. *Int J Precis Eng Man* **2012,** 13, (7), 1273-1279.

139. Shirpour, M.; Gregori, G.; Houben, L.; Merkle, R.; Maier, J. *Solid State Ionics* **2014,** 262, 860-864.

140. Kim, Y. B.; Gur, T. M.; Jung, H. J.; Kang, S.; Sinclair, R.; Prinz, F. B. *Solid State Ionics* **2011,** 198, (1), 39-46.

141. Yang, N.; Cantoni, C.; Foglietti, V.; Tebano, A.; Belianinov, A.; Strelcov, E.; Jesse, S.; Di Castro, D.; Di Bartolomeo, E.; Licoccia, S.; Kalinin, S. V.; Balestrino, G.; Aruta, C. *Nano Lett* **2015,** 15, (4), 2343-2349.

142. Suzuki, T.; Kosacki, I.; Anderson, H. U. *Solid State Ionics* **2002,** 151, (1-4), 111-121.

143. Suzuki, T.; Kosacki, I.; Anderson, H. U. *J Am Ceram Soc* **2002,** 85, (6), 1492-1498.

144. Plonczak, P.; Joost, M.; Hjelm, J.; Sogaard, M.; Lundberg, M.; Hendriksen, P. V. *J Power Sources* **2011,** 196, (3), 1156-1162.

145. Suzuki, T.; Kosacki, I.; Petrovsky, V.; Anderson, H. U. *J Appl Phys* **2002,** 91, (4), 2308-2314.

146. Wang, Y. Z.; Chu, B. L.; He, Q. Y.; Xu, J. *Appl Surf Sci* **2008,** 254, (21), 6799-6801.

147. Lotgering, F. K. *J Inorg Nucl Chem* **1960,** 16, (1-2), 100-108.

148. Lotgering, F. K. *J Inorg Nucl Chem* **1959,** 9, (2), 113-123.

149. https://www.purdue.edu/ehps/rem/rs/sem.htm

150. Muller, D. A. *Nat Mater* **2009,** 8, (4), 263-270.

151. Bogner, A.; Jouneau, P. H.; Thollet, G.; Basset, D.; Gauthier, C. *Micron* **2007,** 38, (4), 390-401.

152. Miller, M. K.; Kenik, E. A. *Microsc Microanal* **2004,** 10, (3), 336-341.

153. Miller, M. K.; Forbes, R. G. *Mater Charact* **2009,** 60, (6), 461-469.

154. Kelly, T. F.; Miller, M. K. *Rev Sci Instrum* **2007,** 78, (3), 031101.

155. Renaud, L.; Martin, I.; Salle, B.; Benbalagh, R.; Davis, A.; Schuhmacher, M. *Microsc Microanal* **2009,** 15, 262-262.

156. Ding, J.; Strelcov, E.; Kalinin, S. V.; Bassiri-Gharb, N. *Nano Lett* **2015,** 15, (6), 3669-3676.

157. Strelcov, E.; Jesse, S.; Huang, Y. L.; Teng, Y. C.; Kravchenko, II; Chu, Y. H.; Kalinin, S. V. *Acs Nano* **2013,** 7, (8), 6806-6815.

158. Strelcov, E.; Ievlev, A. V.; Jesse, S.; Kravchenko, I. I.; Shur, V. Y.; Kalinin, S. V. *Adv Mater* **2014,** 26, (6), 958-963.

159. Cha, D. K.; Park, S. M. *J Electrochem Soc* **1997,** 144, (8), 2573-2580.

160. Bommersbach, P.; Alemany-Dumont, C.; Millet, J. P.; Normand, B. *Electrochim Acta* **2006,** 51, (19), 4011-4018.

161. Trabelsi, W.; Dhouibi, L.; Triki, E.; Ferreira, M. G. S.; Montemor, M. F. *Surf Coat Tech* **2005,** 192, (2-3), 284-290.

162. Gerhardt, R. *J Phys Chem Solids* **1994,** 55, (12), 1491-1506.

163. Hohenberg, P.; Kohn, W. *Phys Rev B* **1964,** 136, (3B), B864-B871.

164. Kohn, W.; Sham, L. J. *Phys Rev* **1965,** 140, (4A), 1133-&.

165. Kohn, W. *Rev Mod Phys* **1999,** 71, (5), 1253-1266.

166. Jones, R. O.; Gunnarsson, O. *Rev Mod Phys* **1989,** 61, (3), 689-746.

167. Kresse, G.; Joubert, D. *Phys Rev B* **1999,** 59, (3), 1758-1775.

168. Kresse, G.; Furthmuller, J. *Phys Rev B* **1996,** 54, (16), 11169-11186.

169. Kalinin, S. V.; Rodriguez, B. J.; Jesse, S.; Morozovska, A. N.; Bokov, A. A.; Ye, Z. G. *Appl Phys Lett* **2009,** 95, (14), 142902.

170. Kumar, A.; Ehara, Y.; Wada, A.; Funakubo, H.; Griggio, F.; Trolier-McKinstry, S.; Jesse, S.; Kalinin, S. V. *J Appl Phys* **2012,** 112, (5), 052021.

171. Kim, S.; Merkle, R.; Maier, J. *Solid State Ionics* **2003,** 161, (1-2), 113-119.

172. Hibino, T.; Hashimoto, A.; Inoue, T.; Tokuno, J.; Yoshida, S.; Sano, M. *Science* **2000,** 288, (5473), 2031-2033.

173. Chueh, W. C.; McDaniel, A. H.; Grass, M. E.; Hao, Y.; Jabeen, N.; Liu, Z.; Haile, S. M.; McCarty, K. F.; Bluhm, H.; El Gabaly, F. *Chem Mater* **2012,** 24, (10), 1876-1882.

174. Feng, Z. L. A.; El Gabaly, F.; Ye, X. F.; Shen, Z. X.; Chueh, W. C. *Nat Commun* **2014,** 5, 4374.

175. Sayle, T. X. T.; Parker, S. C.; Catlow, C. R. A. *Surf Sci* **1994,** 316, (3), 329-336.

176. Harned, H. S.; Robinson, R. A. *T Faraday Soc* **1940,** 36, 0973-0977.

177. Chen, H. N.; Voth, G. A.; Agmon, N. *J Phys Chem B* **2010,** 114, (1), 333-339.

178. Pines, E.; Huppert, D.; Agmon, N. *J Chem Phys* **1988,** 88, (9), 5620-5630.

179. Kreuer, K. D.; Rabenau, A.; Weppner, W. *Angew Chem Int Edit* **1982,** 21, (3), 208-209.

180. Wraight, C. A. *Bba-Bioenergetics* **2006,** 1757, (8), 886-912.

181. Mogensen, M.; Sammes, N. M.; Tompsett, G. A. *Solid State Ionics* **2000,** 129, (1-4), 63-94.

182. Kim, S.; Jain, P.; Avila-Paredes, H. J.; Thron, A.; van Benthem, K.; Sen, S. *J Mater Chem* **2010,** 20, (19), 3855-3858.

183. Nolan, M.; Fearon, J. E.; Watson, G. W. *Solid State Ionics* **2006,** 177, (35-36), 3069-3074.

184. Lee, S. H.; Rasaiah, J. C. *J Chem Phys* **2011,** 135, (12), 124505.

185. Ding, J.; Strelcov, E.; Kalinin, S. V.; Bassiri-Gharb, N. *Nanotechnology* **2016,** 27, (34), 345401.

186. Zhou, Y. H.; Perket, J. M.; Zhou, J. *J Phys Chem C* **2010,** 114, (27), 11853-11860.

187. Sun, C. W.; Li, H.; Chen, L. Q. *Energ Environ Sci* **2012,** 5, (9), 8475-8505.

188. Jung, W.; Dereux, J. O.; Chueh, W. C.; Hao, Y.; Haile, S. M. *Energ Environ Sci* **2012,** 5, (9), 8682-8689.

189. Strelcov, E.; Jesse, S.; Huang, Y. L.; Teng, Y. C.; Kravchenko, I. I.; Chu, Y. H.; Kalinin, S. V. *Acs Nano* **2013,** 7, (8), 6806-6815.

190. Thiwawong, T.; Onlaor, K.; Tunhoo, B. *Adv Mater Sci Eng* **2013,** 2013, 1-7.

191. Varghese, O. K.; Malhotra, L. K. *J Appl Phys* **2000,** 87, (10), 7457-7465.

192. Camellone, M. F.; Ribeiro, F. N.; Szabova, L.; Tateyama, Y.; Fabris, S. *J Am Chem Soc* **2016,** 138, (36), 11560-11567.

193. Gritschneder, S.; Iwasawa, Y.; Reichling, M. *Nanotechnology* **2006,** 18, (4), 044025.

194. Mullins, D. R. *Surf Sci Rep* **2015,** 70, (1), 42-85.

195. Fabbri, E.; Pergolesi, D.; Traversa, E. *Chemical Society reviews* **2010,** 39, (11), 4355-69.

196. Kreuer, K. D. *Annual Review of Materials Research* **2003,** 33, (1), 333-359.

197. Kochetova, N.; Animitsa, I.; Medvedev, D.; Demin, A.; Tsiakaras, P. *RSC Adv.* **2016,** 6, (77), 73222-73268.

198. Han, D.; Kishida, K.; Shinoda, K.; Inui, H.; Uda, T. *Journal of Materials Chemistry A* **2013,** 1, 3027.

199. Fabbri, E.; Pergolesi, D.; Licoccia, S.; Traversa, E. *Solid State Ionics* **2010,** 181, (21-22), 1043-1051.

200. Bohn, H. G.; Schober, T. *J Am Ceram Soc* **2000,** 83, (4), 768-772.

201. Iguchi, F.; Sata, N.; Tsurui, T.; Yugami, H. *Solid State Ionics* **2007,** 178, (7-10), 691-695.

202. Yamazaki, Y.; Blanc, F.; Okuyama, Y.; Buannic, L.; Lucio-Vega, J. C.; Grey, C. P.; Haile, S. M. *Nat Mater* **2013,** 12, (7), 647-51.

203. Björketun, M.; Sundell, P.; Wahnström, G. *Physical Review B* **2007,** 76, (5).

204. Tomoyose, T.; Shimoji, N.; Wakamura, K. *J Phys Soc Jpn* **2005,** 74, (11), 3011-3015.

205. Ishii, T.; Ichigozaki, A. *J Phys Soc Jpn* **2004,** 73, (1), 130-135.

206. Samgin, A. L. *Russ J Electrochem+* **1999,** 35, (3), 287-293.

207. Sundell, P.; Björketun, M.; Wahnström, G. *Physical Review B* **2007,** 76, (9).

208. Goncalves, M. D.; Maram, P. S.; Muccillo, R.; Navrotsky, A. *Journal of Materials Chemistry A* **2014,** 2, (42), 17840-17847.

209. Diercks, D. R.; Gorman, B. P.; Manerbino, A.; Coors, G.; Salvador, P. *Journal of the American Ceramic Society* **2014,** 97, (10), 3301-3306.

210. Devaraj, A.; Gu, M.; Colby, R.; Yan, P.; Wang, C. M.; Zheng, J. M.; Xiao, J.; Genc, A.; Zhang, J. G.; Belharouak, I.; Wang, D.; Amine, K.; Thevuthasan, S. *Nature communications* **2015,** 6, 8014.

211. Hyde, J. M.; Marquis, E. A.; Wilford, K. B.; Williams, T. J. *Ultramicroscopy* **2011,** 111, (6), 440-7.

212. Cancellieri, C.; Fontaine, D.; Gariglio, S.; Reyren, N.; Caviglia, A. D.; Fete, A.; Leake, S. J.; Pauli, S. A.; Willmott, P. R.; Stengel, M.; Ghosez, P.; Triscone, J. M. *Phys Rev Lett* **2011,** 107, (5).

213. Swift, M.; Janotti, A.; Van de Walle, C. G. *Phys Rev B* **2015,** 92, (21).

214. Janotti, A.; Varley, J. B.; Choi, M.; van de Walle, C. G. *Phys Rev B* **2014,** 90, (8), 085202.

215. Sang, X. H.; Grimley, E. D.; Niu, C. N.; Irving, D. L.; LeBeau, J. M. *Appl Phys Lett* **2015,** 106, (6), 162905.

216. Sun, Z. Q.; Fabbri, E.; Bi, L.; Traversa, E. *Phys Chem Chem Phys* **2011,** 13, (17), 7692-7700.

217. Han, D. L.; Kishida, K.; Inui, H.; Uda, T. *Rsc Adv* **2014,** 4, (60), 31589-31593.

218. Yamazaki, Y.; Babilo, P.; Haile, S. M. *Chem Mater* **2008,** 20, (20), 6352-6357.

219. Fabbri, E.; Bi, L.; Tanaka, H.; Pergolesi, D.; Traversa, E. *Advanced Functional Materials* **2011,** 21, (1), 158-166.

220. Yamazaki, Y.; Hernandez-Sanchez, R.; Haile, S. M. *Chem Mater* **2009,** 21, (13), 2755-2762.

221. Yamazaki, Y.; Hernandez-Sanchez, R.; Haile, S. M. *J Mater Chem* **2010,** 20, (37), 8158-8166.

222. Han, D. L.; Kishida, K.; Shinoda, K.; Inui, H.; Uda, T. *J Mater Chem A* **2013,** 1, (9), 3027-3033.

223. Aruta, C.; Han, C.; Zhou, S.; Cantoni, C.; Yang, N.; Tebano, A.; Lee, T. L.; Schlueter, C.; Bongiorno, A. *J Phys Chem C* **2016,** 120, (15), 8387-8391.

224. Chen, Q. L.; Braun, A.; Yoon, S.; Bagdassarov, N.; Graule, T. *J Eur Ceram Soc* **2011,** 31, (14), 2657-2661.

225. Foglietti, V.; Yang, N.; Tebano, A.; Aruta, C.; Di Bartolomeo, E.; Licoccia, S.; Cantoni, C.; Balestrino, G. *Appl Phys Lett* **2014,** 104, (8), 081612.

226. Han, D. L.; Hatada, N.; Uda, T. *J Am Ceram Soc* **2016,** 99, (11), 3745-3753.

227. Medvedev, D.; Murashkina, A.; Pikalova, E.; Demin, A.; Podias, A.; Tsiakaras, P. *Prog Mater Sci* **2014,** 60, 72-129.

228. Di Bartolomeo, E.; D'Epifanio, A.; Yang, N.; Tebano, A.; Balestrino, G.; Licoccia, S. *Solid Oxide Fuel Cells 13 (Sofc-Xiii)* **2013,** 57, (1), 1059-1068.

229. Jesse, S.; Kumar, A.; Arruda, T. M.; Kim, Y.; Kalinin, S. V.; Ciucci, F. *Mrs Bull* **2012,** 37, (7), 651-658.

230. Herklotz, A.; Wong, A. T.; Meyer, T.; Biegalski, M. D.; Lee, H. N.; Ward, T. Z. *Sci Rep-Uk* **2016,** 6, 26491.

231. Guo, H. W.; Dong, S.; Rack, P. D.; Budai, J. D.; Beekman, C.; Gai, Z.; Siemons, W.; Gonzalez, C. M.; Timilsina, R.; Wong, A. T.; Herklotz, A.; Snijders, P. C.; Dagotto, E.; Ward, T. Z. *Phys Rev Lett* **2015,** 114, (25), 256801.

232. Shi, Y. U.; Bork, A. H.; Schweiger, S.; Rupp, J. L. M. *Nat Mater* **2015,** 14, (7), 721-727.